INVESTIGATION OF CRITICAL HEAT FLUX IN REDUCED GRAVITY USING PHOTOMICROGRAPHIC TECHNIQUES

by

Issam Mudawar
Hui Zhang

Boiling and Two-Phase Flow Laboratory
School of Mechanical Engineering
Purdue University
West Lafayette, Indiana 47907

August 2003

Final Report

Prepared for

Boiling and Two-Phase Flow Laboratory

Boiling and Two-Phase Flow Laboratory

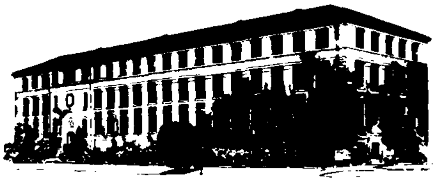

School of Mechanical Engineering

Purdue University
West Lafayette, Indiana 47907

INVESTIGATION OF CRITICAL HEAT FLUX IN REDUCED GRAVITY USING PHOTOMICROGRAPHIC TECHNIQUES

by

Prof. Issam Mudawar
Hui Zhang

Boiling and Two-Phase Flow Laboratory
School of Mechanical Engineering
Purdue University
West Lafayette, Indiana 47907
Tel. (765) 494-5705

August 2003

Final Report

Prepared for

Dr. Mohammad M. Hasan
NASA Glenn Research Center
Mail Stop 500-102
21000 Brookpark Road
Cleveland, OH 44135

TABLE OF CONTENTS

Page

LIST OF TABLES

LIST OF FIGURES

Figure Page

NOMENCLATURE

A	Channel cross-sectional area
A_k	Cross-sectional area occupied by phase k
A_w	Area of wetting front
b	Ratio of wetting front length to wavelength, w/λ
c	Wave speed
$C_{f,i}$	Interfacial friction factor
c_i	Imaginary component of wave speed
$c_{p,f}$	Specific heat of liquid
D_f	Hydraulic diameter of liquid layer, $2W\,(H - \delta)\,/(W + H - \delta)$
D_g	Hydraulic diameter of vapor layer, $2W\,\delta\,/\,(W + \delta)$
f_k	Wall friction factor for phase k
g	Earth's gravitational acceleration
g_n	Component of gravitational acceleration normal to wall, $g \cos \theta$
G	Mass flux, $\rho_f\,U$
H	Channel height (5.0 mm)
h_{fg}	Latent heat of vaporization
H_k	Height (thickness) of phase k layer

h_{meas}	Measured vapor patch height
k	Wave number, $2\pi/\lambda$
k_c	Critical wave number, $2\pi/\lambda_c$
L	Heater length in flow direction (101.6 mm)
P	Pressure
p_i	Interfacial perimeter between phases
p_k	Perimeter of wall contact with phase k
P_o	Outlet pressure
q''	Wall heat flux
q_m''	Critical heat flux
q_w''	Wetting front lift-off heat flux
t	Time
T	Temperature
$\Delta T_{sub,i}$	Inlet subcooling, $T_{sat,i} - T_{b,i}$
$\Delta T_{sub,o}$	Calculated outlet subcooling, $T_{sat,o} - T_{b,o}$
U	Mean liquid inlet velocity
U_f	Liquid phase velocity
U_g	Vapor phase velocity
$U_{g,n}$	Vapor velocity in wetting front normal to wall
u_i	Streamwise velocity of vapor produced at interface
w	Wetting front length used in CHF model

W	Heater and channel width (2.5 mm)
W'_{fg}	Rate of interfacial evaporation per unit streamwise distance
w_j	Length of j^{th} wetting front
w_{meas}	Measured wetting front length
x	Flow quality
z	Streamwise coordinate
$z*$	Extent of continuous upstream wetting region
z_0	Streamwise distance where $U_f = U_g$

Greek symbol

α	Void fraction, δ/H
δ	Mean vapor layer thickness; vapor layer amplitude used in CHF model
η	Interfacial perturbation
η_0	Amplitude of interfacial perturbation, $\eta_0 = \delta$
θ	Flow orientation angle
λ	Vapor wavelength
λ_c	Critical wavelength
λ_j	Wavelength of j^{th} wave
λ_{meas}	Measured vapor patch length
ρ_f	Density of saturated liquid
ρ''_f	Modified liquid density
ρ_g	Density of saturated vapor

ρ_g''	Modified vapor density
σ	Surface tension
τ_i	Interfacial shear stress
$\tau_{w,f}$	Shear stress between wall and liquid
$\tau_{w,g}$	Shear stress between wall and vapor

Subscripts

b	Bulk liquid
f	Saturated liquid
g	Saturated vapor
i	Inlet; imaginary component
k	Phase k ($k = f$ for liquid or g for vapor)
m	Maximum, critical heat flux
o	Outlet
sat	Saturation
w	Wall.

ABSTRACT

Experiments were performed to examine the effects of body force on flow boiling critical heat flux (CHF). FC-72 was boiled along one wall of a transparent rectangular flow channel that permitted photographic study of the vapor-liquid interface just prior to CHF. High-speed video imaging techniques were used to identify dominant CHF mechanisms corresponding to different flow orientations and liquid velocities. Six different CHF regimes were identified: Wavy Vapor Layer, Pool Boiling, Stratification, Vapor Counterflow, Vapor Stagnation, and Separated Concurrent Vapor Flow. CHF showed significant sensitivity to orientation for flow velocities below 0.2 m/s, where extremely low CHF values where measured, especially with downward-facing heated wall and downflow orientations. High flow velocities dampened the effects of orientation considerably. The CHF data were used to assess the suitability of previous CHF models and correlations. It is shown the Interfacial Lift-off Model is very effective at predicting CHF for high velocities at all orientations. The flooding limit, on the other hand, is useful at estimating CHF at low velocities and for downflow orientations. A new method consisting of three dimensionless criteria is developed for determining the minimum flow velocity required to overcome body force effects on near-saturated flow boiling CHF.

Vertical upflow boiling experiments were performed in pursuit of identifying the trigger mechanism for subcooled flow boiling CHF. While virtually all prior studies on flow boiling CHF concern the prediction or measurement of conditions that lead to CHF, this study was focused on events that take place during the CHF transient. High-speed video imaging and photomicrographic techniques were used to record the transient behavior of interfacial features from the last steady-state power level before CHF until the moment of power cut-off following CHF. The video records show the development of a wavy vapor layer which propagates along the heated wall, permitting cooling prior to CHF only in wetting fronts corresponding to the wave troughs. Image analysis software was developed to estimate void fraction from the individual video images. The void fraction records for subcooled flow boiling show the CHF transient is accompanied by gradual lift-off of wetting fronts culminating in some maximum vapor layer mean thickness, following which the vapor layer begins to thin down as the transition to film boiling ensues. This study proves the Interfacial Lift-off Model, which has been validated for near-saturated flow boiling CHF, is equally valid for subcooled conditions.

CHAPTER 1

INTRODUCTION

1.1 Flow Boiling CHF Mechanisms and Models

The trigger mechanism for critical heat flux (CHF) in flow boiling has been the subject of intense debate for over five decades. There is nothing approaching a unified comprehensive understanding despite the thousands of experiments conducted to date [1]. Direct observation of vapor formations near the heated wall is the most popular and effective means for gaining insight into the physical CHF trigger mechanism. Yet such techniques are often costly, time consuming, and prone to failure due to the extreme temperatures encountered at CHF. This explains why flow visualization studies of the CHF mechanism tend to be qualitative, and intended mostly to develop a correlation applicable to a particular system or flow pattern. This type of experiment does little to aid the theoretical understanding of the problem.

Dryout is one type of CHF, which occurs in low mass velocities, low subcooling and/or large length-to-diameter ratio channels. It constitutes a relatively mild form of CHF and is associated with relatively small excursions in the wall temperature. *Departure from nucleate boiling* is a far more severe form of CHF because it precipitates abrupt rise in the wall temperature even in the presence of abundant liquid flow in the channel core. The present study concern this more severe type of CHF, which is of vital important to the design and safety assessment of nuclear, aerospace, defense, medical and electronic systems involving intense heat removal from heat-flux-controlled surfaces.

Other than dryout, four major physical mechanisms have been postulated as the trigger for CHF in subcooled and near-saturated flow boiling. All these mechanisms are based upon some physical process that restricts bulk liquid flow from reaching the heated wall.

1.1.1 Boundary Layer Separation Model

The earliest subcooled CHF model is based on the hypothesis of boundary layer separation. As illustrated in Fig. 1.1(a), the forward movement of near-wall liquid in the boundary layer is obstructed by vapor production at the wall. At CHF, this obstruction decreases the near-wall liquid velocity gradient to the point of liquid stagnation just outside the bubble layer. This greatly decreases the liquid's ability to compensate for the intense vapor production at the wall. Eventually, the bulk liquid flow detaches from the heated wall, inducing dryout downstream.

Kutateladze and Leont'ev [2] postulated vapor production in flow boiling is very similar to gas injection into a turbulent boundary layer flowing over a permeable flat plate. To predict subcooled CHF, they utilized a pool boiling CHF correlation and a subcooling parameter which accounted for the heat flux necessary to induce boundary layer separation. However, boundary layer separation and pool boiling are two distinctly different processes, and there is no physical reason to expect that their heat fluxes are in

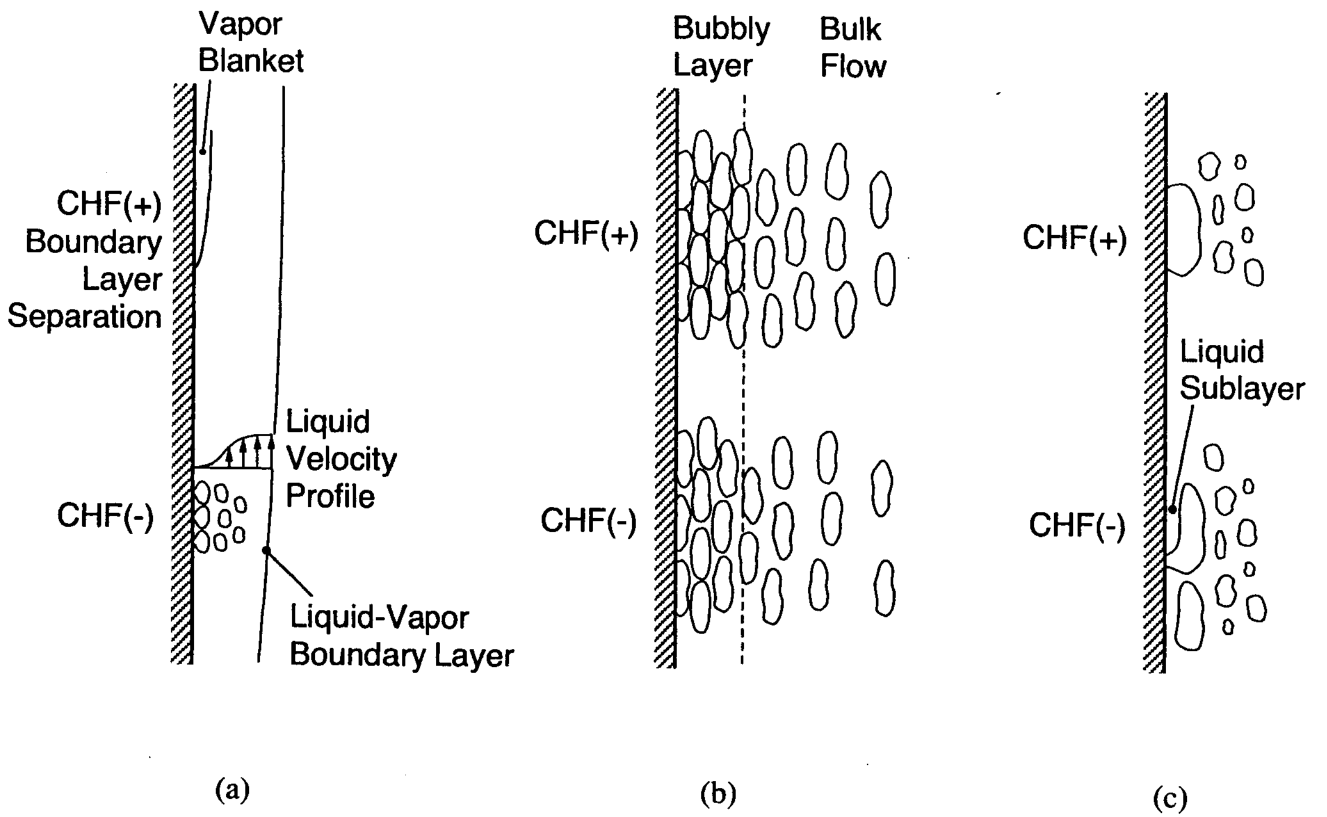

Fig. 1.1 Flow boiling CHF mechanisms according to (a) Boundary Layer Separation Model, (b) Bubble Crowding Model, and (c) Sublayer Dryout Model.

any way additive. Tong [3,4] and Purcupile and Gouse [5] developed empirical CHF correlations loosely built upon the Boundary Layer Separation Model.

1.1.2 Bubble Crowding Model

A second mechanism that has been postulated to trigger CHF is bubble crowding. This mechanism is governed by turbulent fluctuations in the liquid flow at the outer edge of the near-wall bubbly layer. As illustrated in Fig. 1.1(b), these turbulent fluctuations become too weak at high heat fluxes to transport bulk liquid through the dense bubbly layer in order to cool the wall. Eventually, the bubbly layer coalesces into a vapor layer and CHF ensues.

To model this process, a critical void fraction that precedes CHF must be defined. It is the maximum volume fraction at which the bubbles can maintain separation in the bubbly layer with no significant contact. The bubbly layer was idealized by Weisman and Pei [6] as consisting of ellipsoidal bubbles having an axis ratio of 3 to 1. When these idealized bubbles are stacked into a bubbly layer they produce a near-wall void fraction of 82%. Weisman and Pei utilized three empirical parameters to achieve good agreement with CHF data for water. Their model also showed good predictions for R-11, R-113, liquid nitrogen, and anhydrous ammonia, and was later extended by Weisman and Ileslamlou [7] to highly subcooled conditions.

Overall, the use of several empirical constants and, more importantly, the critical void fraction assumption raise serious questions about the validity of this model. Depending on flow conditions such as mass velocity, pressure, and subcooling, Styrikovich *et al.* [8] measured near-wall void fractions from 30 to 95%, which contradicts the fixed value of 82% utilized in the Bubble Crowding Model.

1.1.3 Sublayer Dryout Model

The third type of CHF trigger mechanism is based upon sublayer dryout. The Sublayer Dryout Model treats the liquid-vapor exchange as a more localized phenomenon than the Boundary Layer Separation Model and Bubble Crowding Model do. The Sublayer Dryout Model is based on observations from a number of earlier studies. Several researchers reported observing significant coalescence of small vapor bubbles at high heat fluxes into vapor patches that moved along the heated wall. Furthermore, the vapor patches were observed to trap a thin liquid sublayer which seemed to provide the necessary cooling for the wall prior to CHF [9-12].

The Sublayer Dryout Model is based on the assumption that CHF will commence upon evaporation of the thin liquid sublayer. Lee and Mudawar [13] provided the basic framework for this model. As depicted in Fig. 1.1(c), they postulated CHF to occur when the wall heat flux surpasses the enthalpy of liquid replenishing the sublayer from the bubbly layer and bulk liquid. The Helmholtz wavelength, calculated from bubble rise velocity and liquid velocity, was used to determine the length of the sublayer since bubbles that are longer than the Helmholtz wavelength are unstable and should break up into smaller bubbles. A momentum balance on the vapor blanket normal to the heated surface yields the liquid sublayer thickness.

Several researchers borrowed much of the original formulation of the Lee and Mudawar model. Lin *et al.* [14] modified this model slightly to aid the prediction of CHF in both subcooled and low positive quality flows. The Katto [15-17] and Celata *et al.* [18,19] CHF models are all fairly similar to the Lee and Mudawar model. The significant differences in these models are found in the methods used to calculate vapor velocity and liquid sublayer thickness.

1.1.4 Interfacial Lift-off Model

The fourth CHF mechanism is based upon the Interfacial Lift-off Model. This model was developed by Galloway and Mudawar [20,21] based upon extensive flow visualization experiments they carried out at near saturated conditions, relatively low flow velocities and a heated length 4.96 times the hydraulic diameter. Using back lighting of the boiling flow in a rectangular channel with transparent sidewalls, they were able to clearly capture the liquid-vapor interface as a silhouette. As CHF was approached, a series of vapor patches were observed to propagate along the heated wall resembling a fairly continuous wavy vapor layer. As illustrated in Fig. 1.2, the vapor patches appeared to insulate the heated wall beneath, and virtually all the wall cooling occurred by vigorous boiling in *wetting fronts* located in troughs between the vapor patches. They identified the CHF trigger mechanism by separation of the most upstream wetting front off the wall. Once this cooling path was eliminated, the heat flux increased in the other wetting fronts, forcing them to separate in succession, and leading to the formation of a continuous vapor blanket which insulated the entire heated wall.

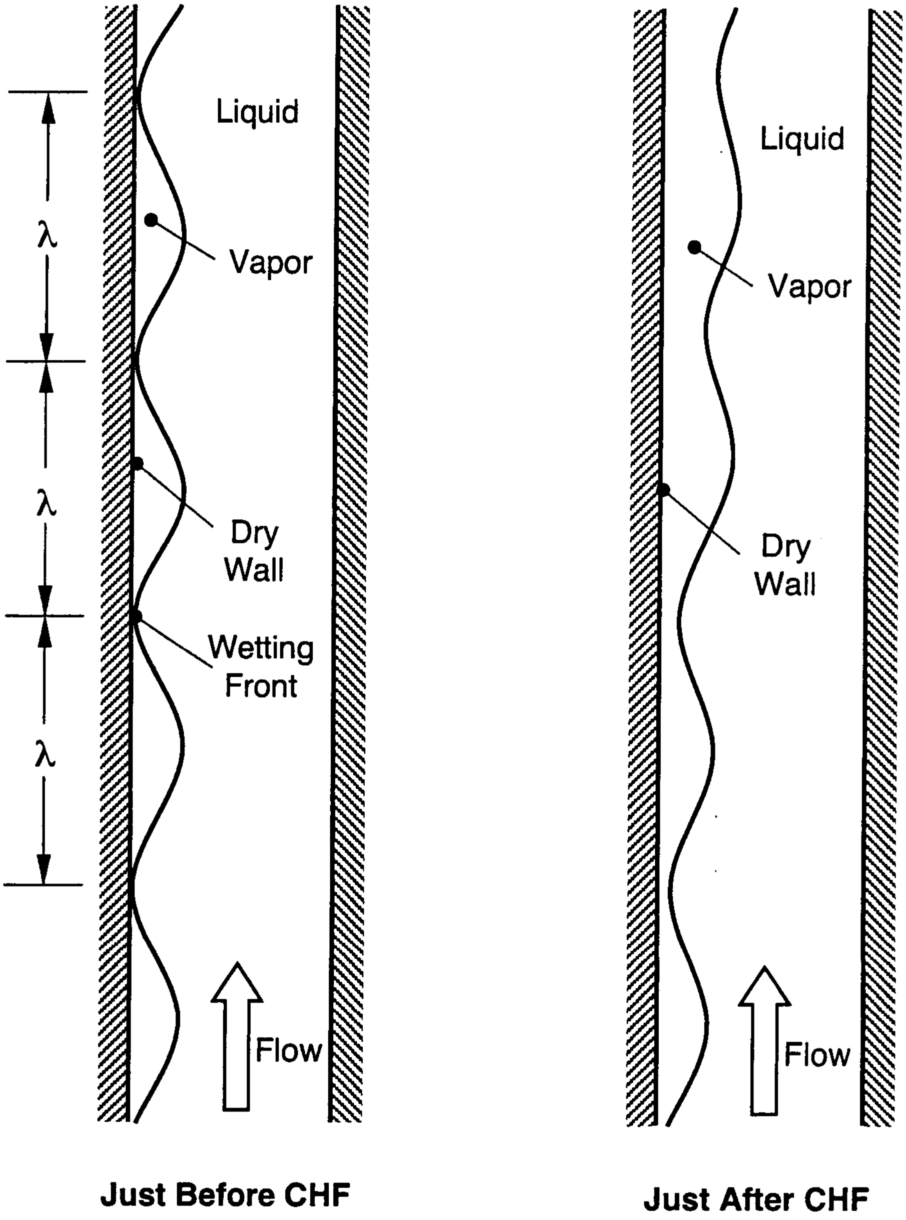

Fig. 1.2 Flow boiling CHF mechanism according to Interfacial Lift-off Model.

Galloway and Mudawar postulated wetting fronts detach when the pressure force associated with interfacial curvature, which is responsible for maintaining liquid contact with the wall, is overcome by vapor momentum in the wetting front normal to the heated wall.

The interfacial lift-off model was extended by Gersey and Mudawar [22,23] to a wider channel and a heated lengths up to 16.5 the hydraulic diameter. They showed that the interfacial wavelength increases in the streamwise direction, eventually reaching an asymptotic value. This increase was attributed to wave stretching and drag-induced merging between consecutive vapor patches. Sturgis and Mudawar [24,25] performed flow visualization on long heaters for both saturated and subcooled conditions. The wavy vapor patches observed at saturated conditions by Galloway and Mudawar and Gersey and Mudawar were the dominant vapor formations in subcooled flow as well. Compared with saturated conditions, both wavelength and amplitude of the vapor patches decreased with increased subcooling. Sturgis and Mudawar also performed a statistical investigation of vapor formations, and categorized them into ones that involved trapping of a liquid sublayer (as described by the Sublayer Dryout Model) versus those that followed the wavy vapor layer depiction. The vapor formations necessary for sublayer dryout were observed less than 10% of the time for near-saturated flow and about 25% for subcooled flow, proving the wavy vapor layer behavior occurs with far greater frequency.

Zhang *et al.* [26,27] investigated the effects of gravitational force on flow boiling CHF using different flow orientations. They identified six different CHF regimes associated with the different orientations, flow velocities and subcoolings. Vertical upflow at all velocities, as well as high velocity flow (> 0.5 m/s) at all orientations was dominated by the wavy vapor layer behavior. They observed that the vapor waves generated upstream tend to preserve a wave curvature value as they propagate along the heated wall, and confirmed that CHF is triggered by lift-off of vapor waves with a certain wave curvature value. They modified the Interfacial Lift-off Model to incorporate the effects of gravitational force on near-saturated flow boiling CHF.

1.2 Effects of Orientation on Flow Boiling CHF

Howard and Mudawar [28] investigated the effects of wall orientation on pool boiling CHF. They showed orientation effects fall into three regions; each is associated with a unique CHF trigger mechanism. In the upward-facing region, the buoyancy forces remove the vapor vertically off the wall in accordance with the classical interpretation by Zuber et al. [29]. In the downward-facing region, the vapor stratifies beneath the heated wall, resulting in very small CHF values. The near-vertical region is characterized by a wavy liquid-vapor interface very similar to that proposed earlier for flow boiling by Galloway and Mudawar [20,21] and Sturgis and Mudawar [24,25]. Howard and Mudawar adapted the Interfacial Lift-off model to accurately predict near-vertical region CHF data.

Orientation effects in flow boiling are complicated by the influence of liquid inertia. Buoyancy plays a dominant role at low velocities due to weak inertia, which results in lower CHF values for downflow, for example, compared to upflow at the same velocity. Increasing the liquid velocity imparts dominance to liquid inertia. In fact, high velocities can completely negate the effects of orientation, producing virtually equal CHF for downflow as for upflow. These trends were confirmed by Simoneau and Simon [30] and Mishima and Nishihara [31]. Both studies showed vapor motion in a vertical downflow switches from concurrent at high liquid velocities to countercurrent at low velocities. Mishima and Nishihara suggested flooding is the cause of CHF for downflow at very low velocities. They also identified a very low CHF downflow condition where bubbles stagnate upon the heated wall because of a balance between liquid inertia and buoyancy force.

In a previous paper by the authors of the present study [26], the effects of orientation on flow boiling CHF were investigated experimentally at eight orientations spaced 45° apart using FC-72 as working fluid. Figure 1.3 provides a definition of flow orientation as well as the location of the heated wall for each orientation. Orientation angle is referenced to the $\theta = 0°$ horizontal orientation with the heated wall facing upwards. Based on photographic results, six CHF regimes were identified for saturated flow, which are represented in Fig. 1.4:

Wavy vapor layer,

Pool boiling,

Stratification of vapor above liquid,

Vapor stagnation,

Vapor counterflow, and

Separated concurrent vapor flow.

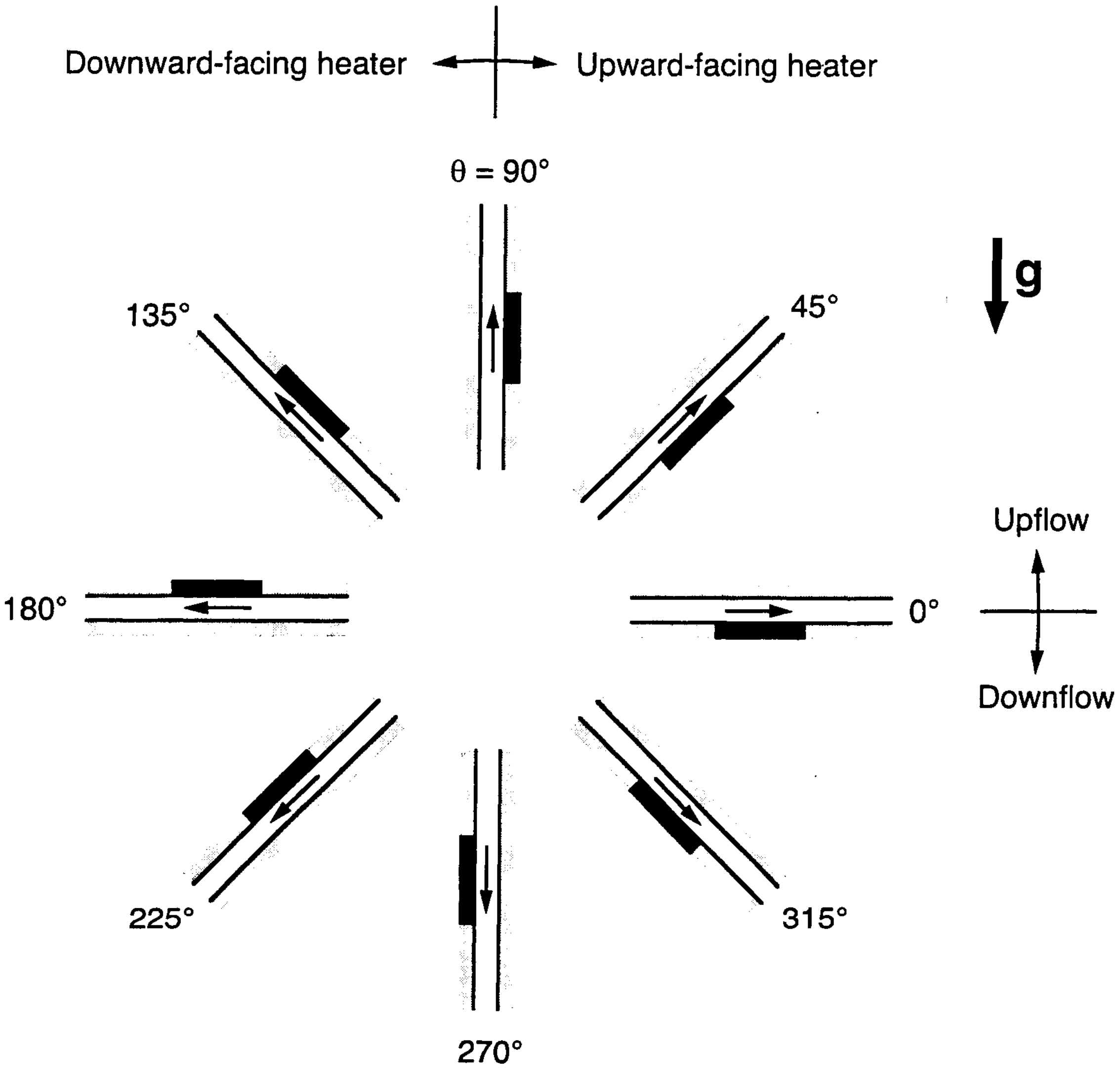

Fig. 1.3 Flow orientation nomenclature. Heater location for each orientation is indicated by black rectangle.

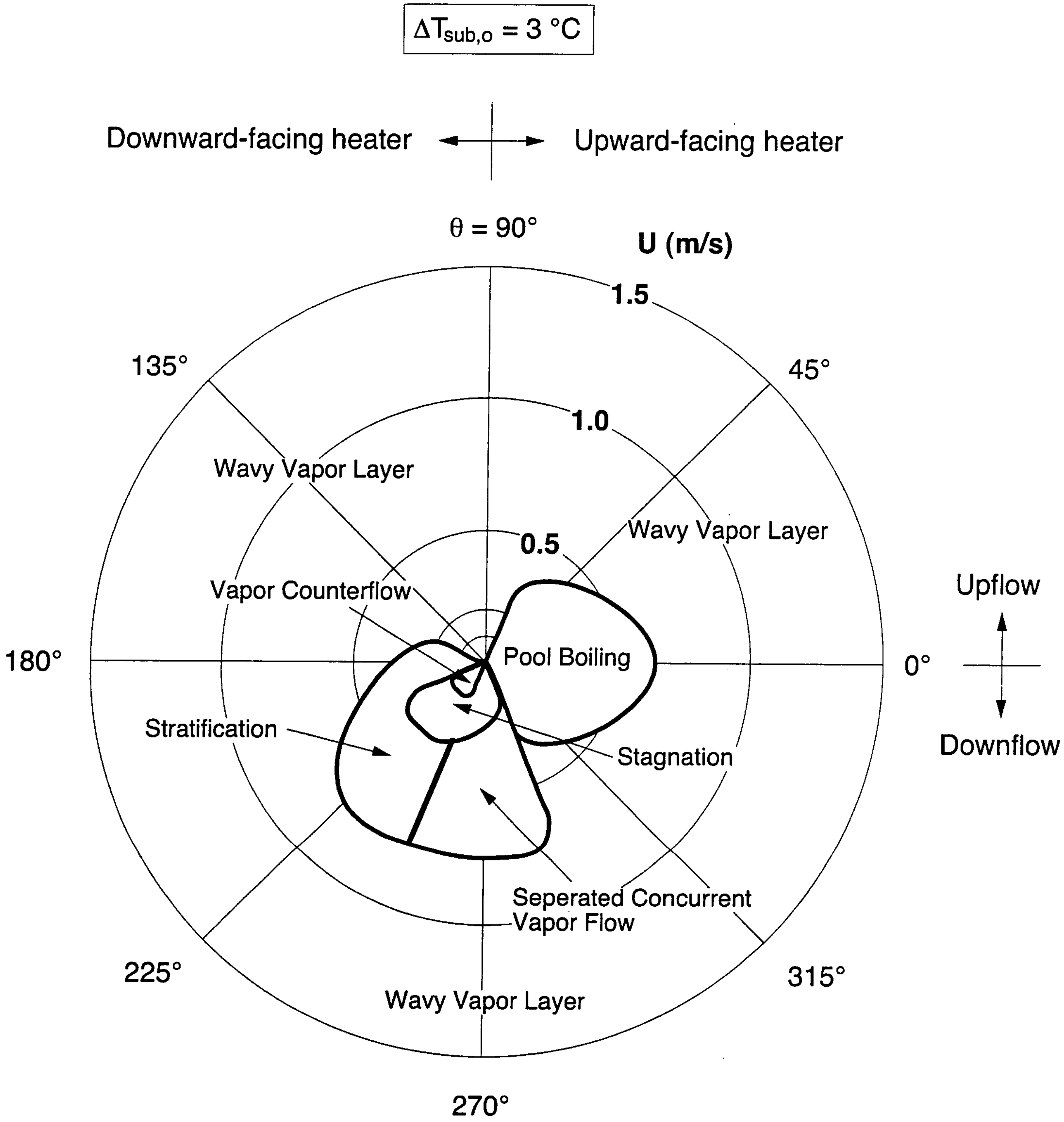

Fig. 1.4 CHF regimes for saturated flow.

The low velocity, upward-facing heated wall data were underpredicted by the Zuber et al. model [29] for pool boiling. The vapor stagnation, vapor counterflow, and vapor concurrent flow data seemed closely related to flooding. The wavy vapor layer regime encompassed high-velocity conditions at all orientations, as well as low-velocity upflow orientations. CHF data belonging to the wavy vapor layer regime were within the range of Sturgis and Mudawar's [24,25] Interfacial Lift-off model predictions. Since this model was developed for horizontal flow, the predictions did not distinguish between different flow orientations, and resulted in equal CHF for all orientations corresponding to the same velocity.

CHAPTER 2

EXPERIMENTAL METHODS

2.1 Flow Boiling Module

A flow boiling test module was fabricated which enabled side-viewing of vapor formations along a heated surface. The module was formed by bolting together two transparent polycarbonate plastic (Lexan) plates, as shown in Figure 2.1. A 5.0 mm × 2.5 mm slot was milled into the bottom plate of the test module, forming a flow channel. A side portion of the same bottom plate was milled out to facilitate the insertion of a copper heater flush with one side of the flow channel. A hydrodynamically fully-developed flow was achieved by placing the heater 106 hydraulic diamaters from the inlet. A honeycomb insert at the channel inlet straightened the flow and broke up any large eddies. The two test module plates were bolted together, trapping a flexible Teflon cord in a shallow slot on the underside of the top plate, providing a leak-proof assembly. Leaks around the heater surfaces were prevented by careful application of a thin film of high-temperature RTV silicone rubber. Fluid temperature and pressure were measured both upstream and downstream of the heater. The pressure was measured with 0.01% accuracy transducers.

FC-72, a 3M Company dielectric fluid recommended for cooling of electronic and power devices in space systems, was used in all the tests. Its relatively low boiling point

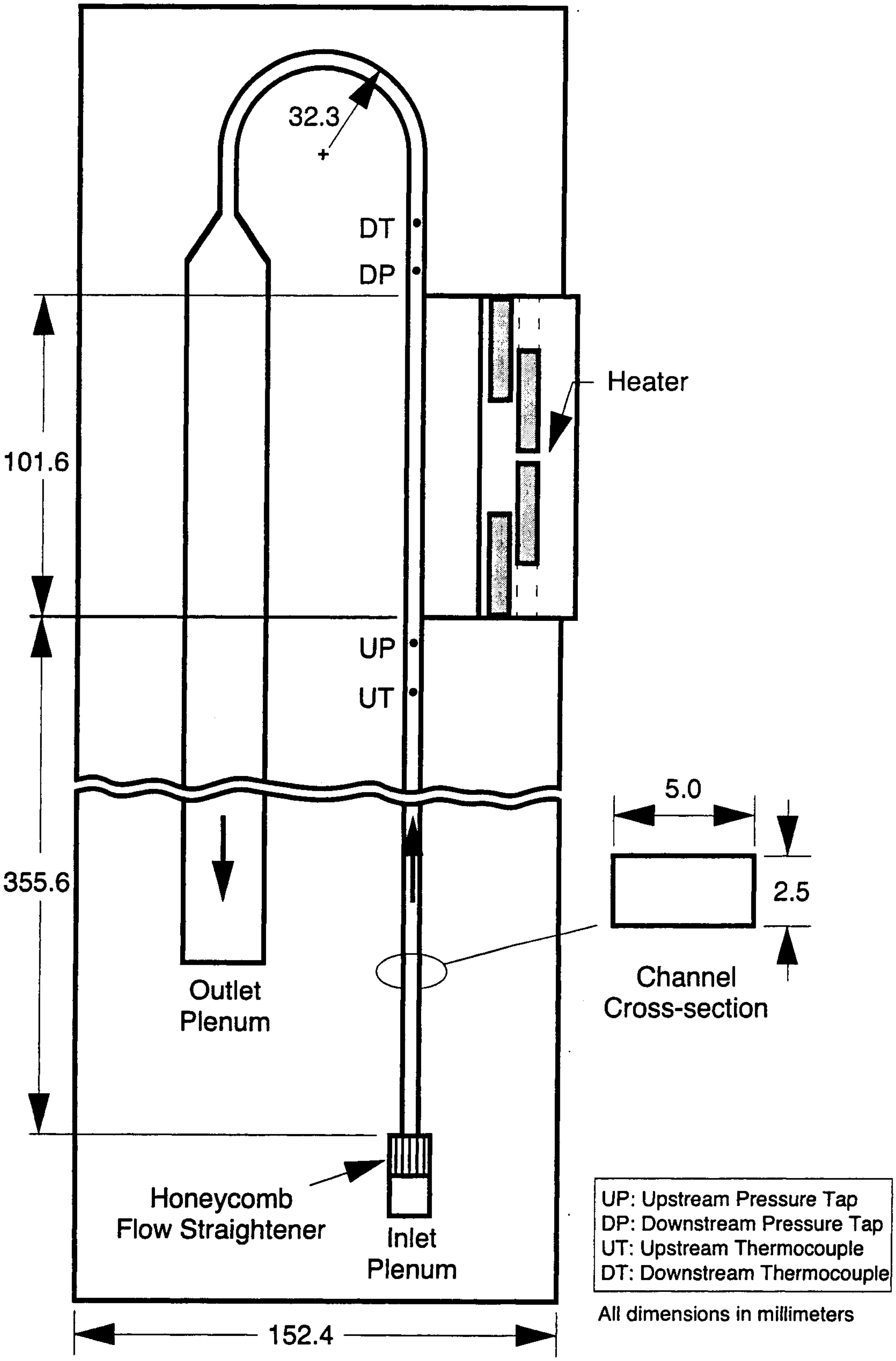

Fig. 2.1 Bottom plate of test module.

(56°C at atmospheric pressure) and low CHF values are both especially attractive for photographic study of the CHF mechanism because the unsteady CHF temperature excursion with this fluid is much slower than with water, which greatly reduces the danger of test module burnout.

The heater block was fabricated from a single block of 99.99% pure (oxygen-free) copper. A thin portion of the block was inserted into the lower plate of the test module as shown in Figure 2.2. The heated surface, Figure 2.3, was 2.5 mm wide and 101.6 mm along the flow direction. Heat was supplied by four 150-W cartridge heaters that were embedded in the thick protruding portion of the copper block. These cartridge heaters were powered by a single 115-volt variable transformer, allowing the heat dissipation to be incremented manually during testing. The cartridge heaters were distributed symmetrically in the thick portion of the copper block to ensure even heat dissipation along the heater surface in contact with the fluid.

Local heat flux and local wall temperature were determined with five sets of Type-K thermocouples inserted strategically along the heater. Each set consisted of three thermocouples situated 1.02, 6.10, and 11.18 mm from the surface.

Assuming locally one-dimensional heat conduction through the thin portion of the copper heater inserted into the lower plate of the test module, a temperature profile was calculated using a linear squares best-fit to the three thermocouple readings at each of the five thermocouple locations. This profile was then used to calculate both the local heat flux, q'', and local wall temperature, T_w. The heat flux and wall temperature were determined with 7.9% and 0.3 °C uncertainty, respectively.

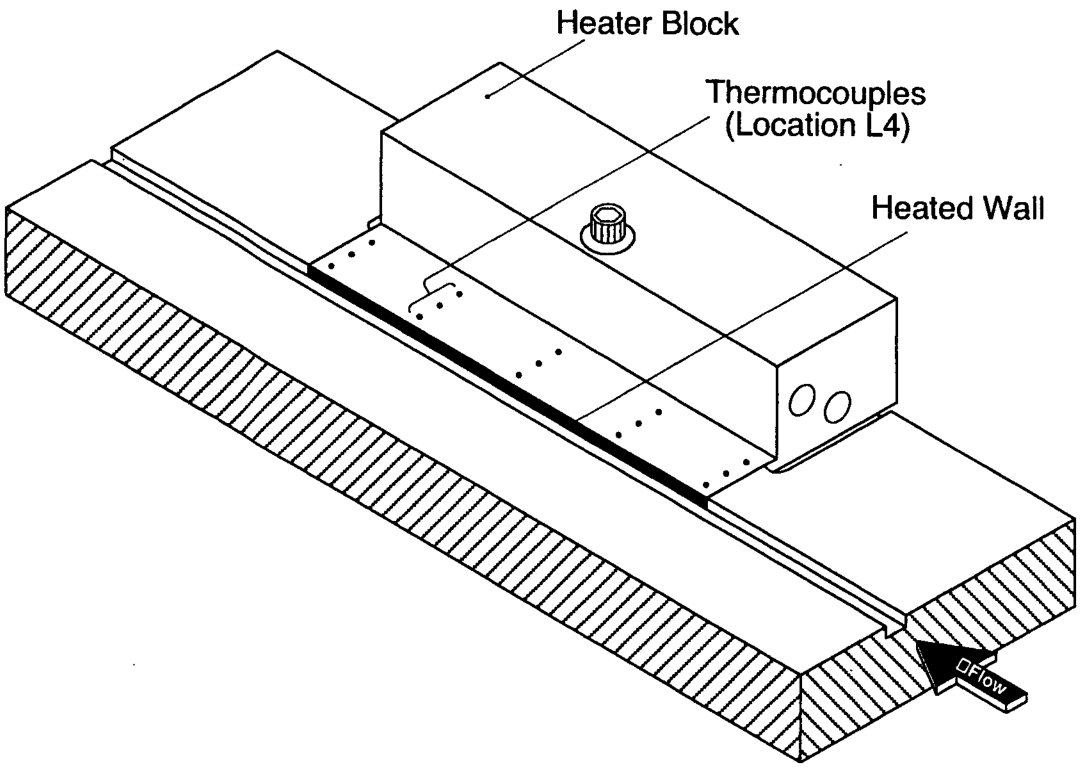

Fig. 2.2 Heater inserted into bottom plate of test module.

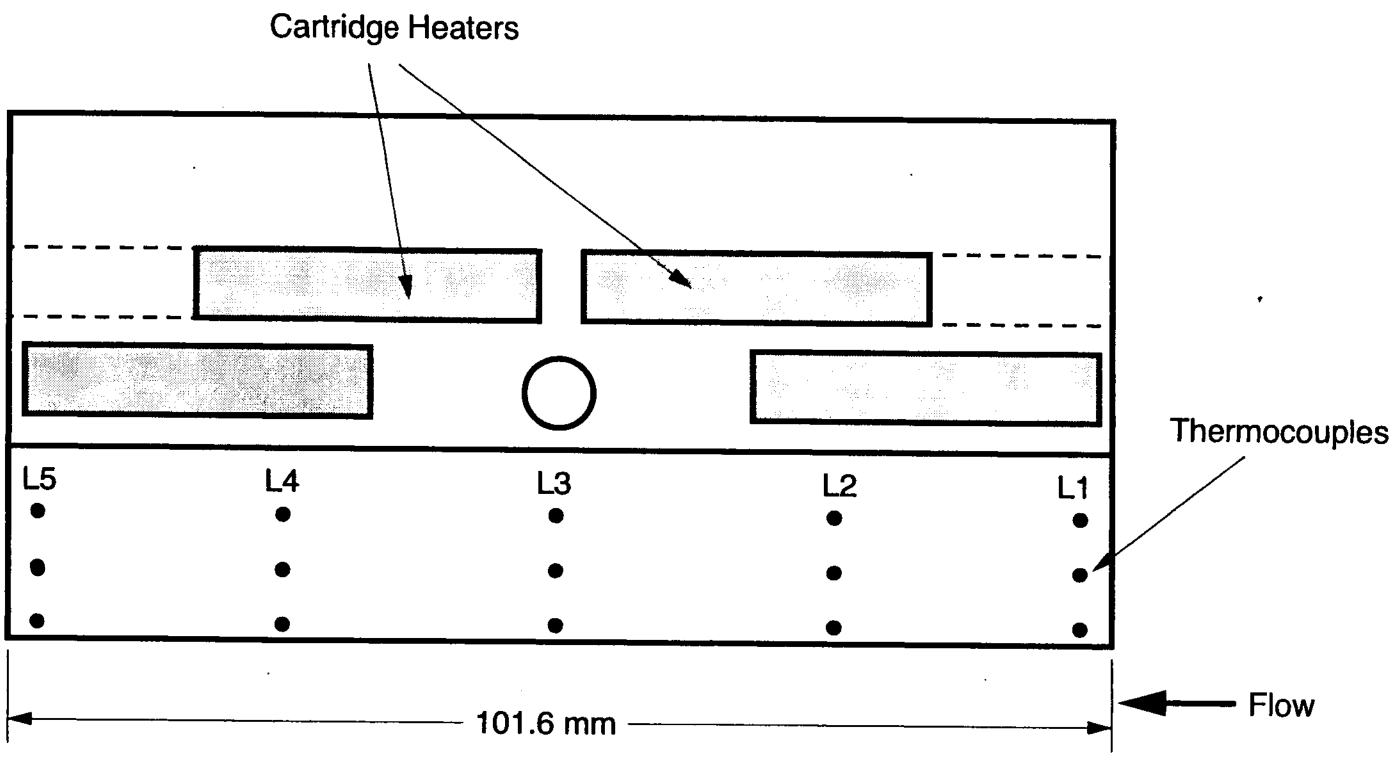

Fig. 2.3 Top view of heater.

The calculation of fluid bulk temperature, $T_{b,o}$, at a particular thermocouple location along the flow direction was based on heat input up to that location and the assumption of a well-mixed flow. The inlet fluid temperature was measured by the upstream thermocouple. However, the downstream thermocouple did not provide an accurate reading of the exit temperature since void fraction at the outlet was quite large in many cases. For this reason, the mixture outlet temperature was calculated in the same manner as the bulk temperature.

2.2 Flow Loop

Figure 2.4 shows a schematic of the two-phase flow loop that was used to supply liquid FC-72 to the test module at the desired operating conditions. To ensure flow stability, only a fraction of the total flow entered the flow channel; the balance was by-passed to the loop's reservoir. Fluid flow into the channel was controlled by two valves, one located in the by-pass line and the other upstream of the test module. Flow rate was measured by two variable area rotameters (used mostly for visual monitoring) and a turbine flowmeter. The turbine flowmeter had a 2.3% accuracy.

The fluid temperature was modulated by a flat-plate heat exchanger and an in-line heater. The primary purpose of the heat exchanger was to cool the bulk flow from energy supplied by the test heater and the pump, using water as secondary coolant. Connected to a variable transformer, the in-line heater fine-tuned the fluid temperature prior to entering the flow channel.

The entire facility, which included the two-phase flow loop and instrumentation cabinets, was mounted onto a steel cart equipped with heavy-duty casters. This was

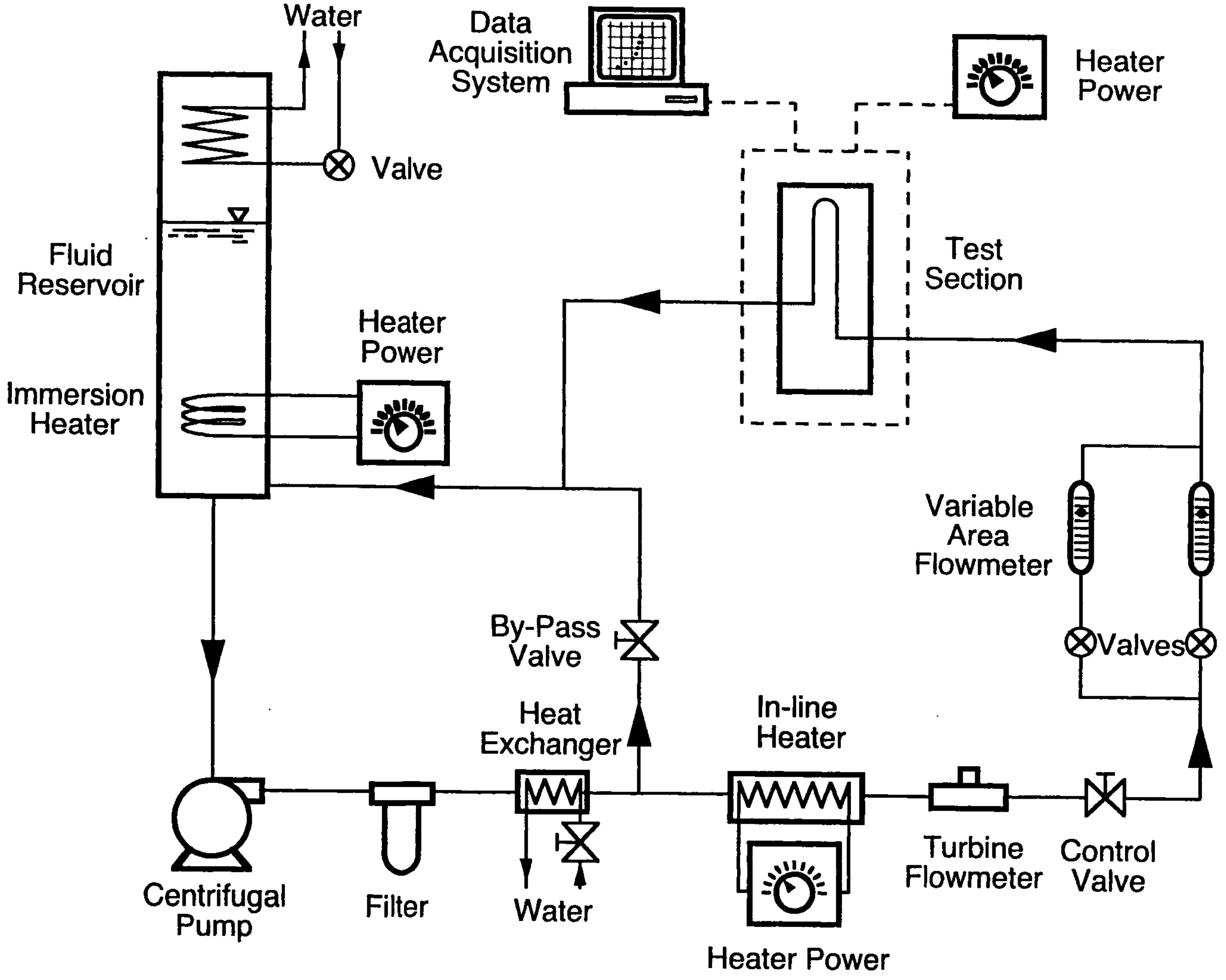

Fig. 2.4 Two-phase flow loop.

intended to facilitate convenient transport of the facility for future parabolic flight microgravity experiments. The test module was connected to a bracket that included a 0-360 degree angular rotation stage, and the bracket was mounted atop the cart. The rotation stage enabled testing at all orientations relative to Earth's gravity.

2.3 Test Conditions

For each test, the inlet temperature, outlet pressure, and flow rate were first adjusted to the desired test conditions with the heater electrical power set very low. Once thermal conditions became steady, a data point was recorded and electrical power incremented. Continuing in this manner, the test proceeded through the single-phase and two-phase regions generating a boiling curve which was terminated at CHF. Steady-state conditions were evaluated based on the standard deviation of the surface temperature at thermocouple Location 5. CHF is defined here as the last stable condition prior to a sudden drop in heat flux, accompanied by a sudden increase in surface temperature.

As shown in Figure 1.3, tests were conducted at 8 different orientations. The horizontal orientation with the heated surface facing upwards is defined as $\theta = 0°$. Moving counterclockwise, the orientation angle was increased in 45° increments to cover representative conditions for all orientations.

For each orientation, tests were carried out at two outlet subcooling levels, referred to in this paper as saturated ($\Delta T_{sub,o}$ = 3 °C) and subcooled ($\Delta T_{sub,o}$ = 30 °C). For the saturated conditions, five flow velocities (U = 0.1, 0.2, 0.5, 1.0 and 1.5 m/s) were studied. Only three velocities (U = 0.5, 1.0 and 1.5 m/s) were examined. The small flow rates associated with velocities below 0.5 m/s meant the liquid had to be supplied at very low inlet temperatures to provide the desired exit subcooling. Instead of a water-cooled heat exchanger, these low inlet temperatures demand a refrigeration system which was unavailable for the present study.

The outlet subcooling ($\Delta T_{sub,o}$) values refer to the subcooling existing at the outlet of the heated section at the time CHF was reached. The outlet pressure was held constant at P_o = 138 kPa (20 psia) in all tests; the corresponding saturation temperature of FC-72 is $T_{sat,o}$ = 66.3 °C. Therefore, at the time CHF was reached, the outlet bulk fluid temperature was $T_{b,o}$ = 63.3 °C for the saturated tests, or 36.3 °C for the subcooled.

2.4 Photographic Techniques

A Redlake MotionScope PCI 8000s high-speed digital video system was used to capture vapor-liquid interfacial features just prior to CHF. The video camera in this system is capable of recording speeds from 60 to 8000 frames per second (fps) with 256 gray scale levels, and its electronic shutter can be modulated from 1/60th s down to 10 μs. Selecting an appropriate speed for the present study was based on several requirements, most important of which were lighting, resolution, and minimal interfacial shift. Optimum video imaging was realized with a recording rate of 1000 fps and a shutter speed of 50 μs. The system recorded over 2 s of video, which consisted of 2048 individual frames, each consisting of 240 × 210 pixels. This recording time was far too short to capture the detailed CHF transient. Therefore, the system was modified for the transient CHF experiments by connecting a Canon GL1 digital video camera to the Redlake MotionScope video system. This camera provided the shutter speeds needed to "freeze" interfacial features, but could not provide high-frequency sequential tracking at the rate of the Redlake camera.

Figure 2.5 shows the flow visualization setup. The digital video camera was positioned perpendicular to the flow channel. The camera was attached to a tripod so that it could traverse the entire vertical length of the heated wall. This was necessary because the video segments were taken at the inlet, middle, and outlet of the heated wall separately in order to capture the streamwise development of interfacial features with high resolution. The flow was backlit with a light source with adjustable intensity and focus. A semi-opaque sheet of paper was used to soften and diffuse the incoming light. Like the camera, the light source was mounted on a tripod to traverse the entire length of the heated wall.

Figure 2.6 shows a composite of flow characteristics at U = 1.5 m/s captured just prior to CHF at the inlet, middle and outlet sections of the heated wall. For $\Delta T_{sub,o}$ = 3 °C, Fig. 2.6(a), the vapor flow takes the form of relatively long, periodic wavy vapor patches separated by liquid wetting fronts. At the channel exit, the vapor layer occupies a large fraction the channel cross-section. For $\Delta T_{sub,o}$ = 30 °C, vapor patches are shown in Fig. 2.6(b) sliding along the heated surface, separated by liquid wetting fronts, but the overall thickness of the vapor layer is significantly smaller because of the strong condensation effects.

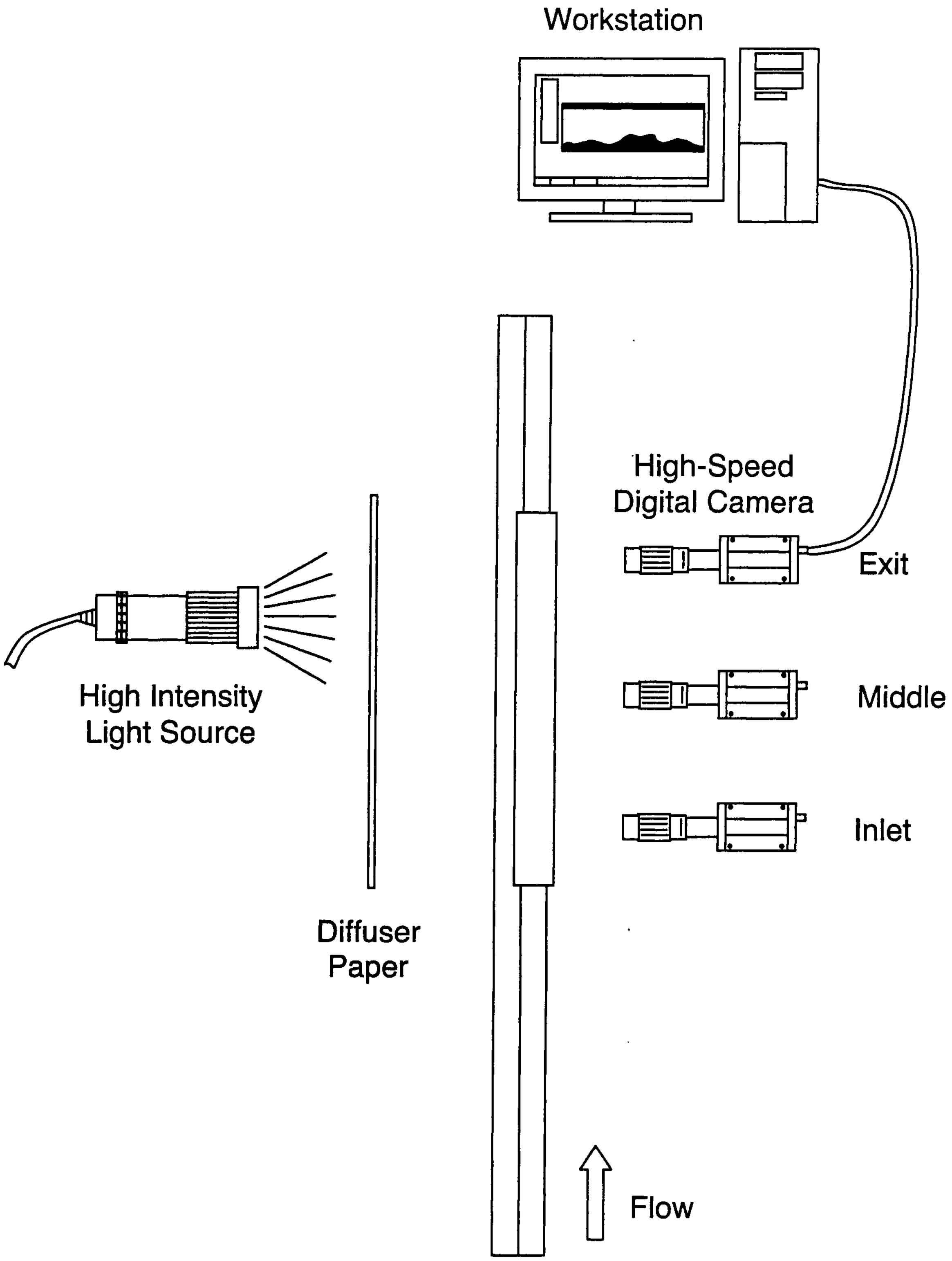

Fig. 2.5 Flow visualization setup.

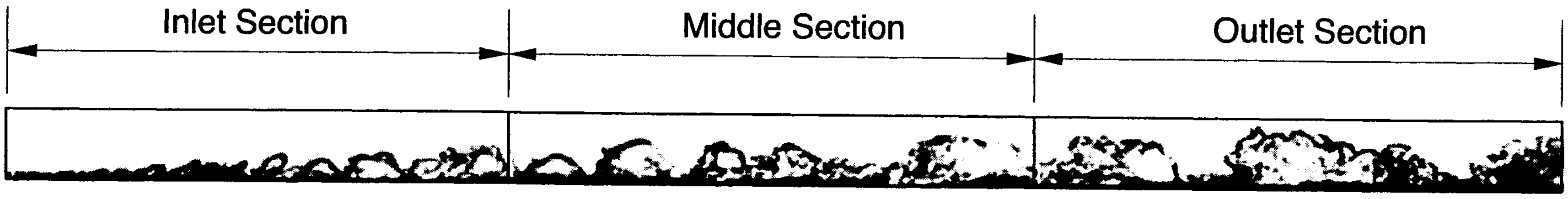

(a) $\Delta T_{sub,o} = 3$ °C

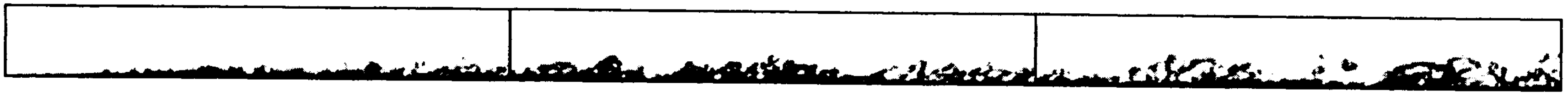

(b) $\Delta T_{sub,o} = 30$ °C

Fig. 2.6 Composite images of wavy vapor layer in vertical upflow at U = 1.5 m/s just prior to CHF for (a) $\Delta T_{sub,o} = 3$ °C and (b) $\Delta T_{sub,o} = 30$°C.

CHAPTER 3

EXPERIMENTAL RESUSLTS

3.1 CHF Regimes

Figure 3.1(a) shows all CHF data collected from this study in a flow velocity – flow orientation plane. The CHF data are grouped into six different regimes for which representative photographs are depicted in Fig. 3.1(b). The most obvious feature of this CHF map is the existence of a dominant *Wavy Vapor Layer Regime* corresponding to all high velocities and at all orientations. At and below 0.5 m/s, there exist a number of complex CHF regimes. Notice that the Wavy Vapor Layer Regime is prevalent even for very low velocities for the vertical and near-vertical orientations, $\theta = 90$ and 135°, respectively. This regime is consistent with CHF depictions of flow boiling by Galloway and Mudawar [20,21].

A *Pool Boiling Regime* exists for low velocities, and $\theta = 0$, 45 and 315°. Bubble behavior within these horizontal and near-horizontal orientations with an upward-facing heated wall resembles pool boiling CHF from large horizontal surfaces. All four remaining CHF regimes are associated with downflow and downward-facing heated wall orientations at low velocities.

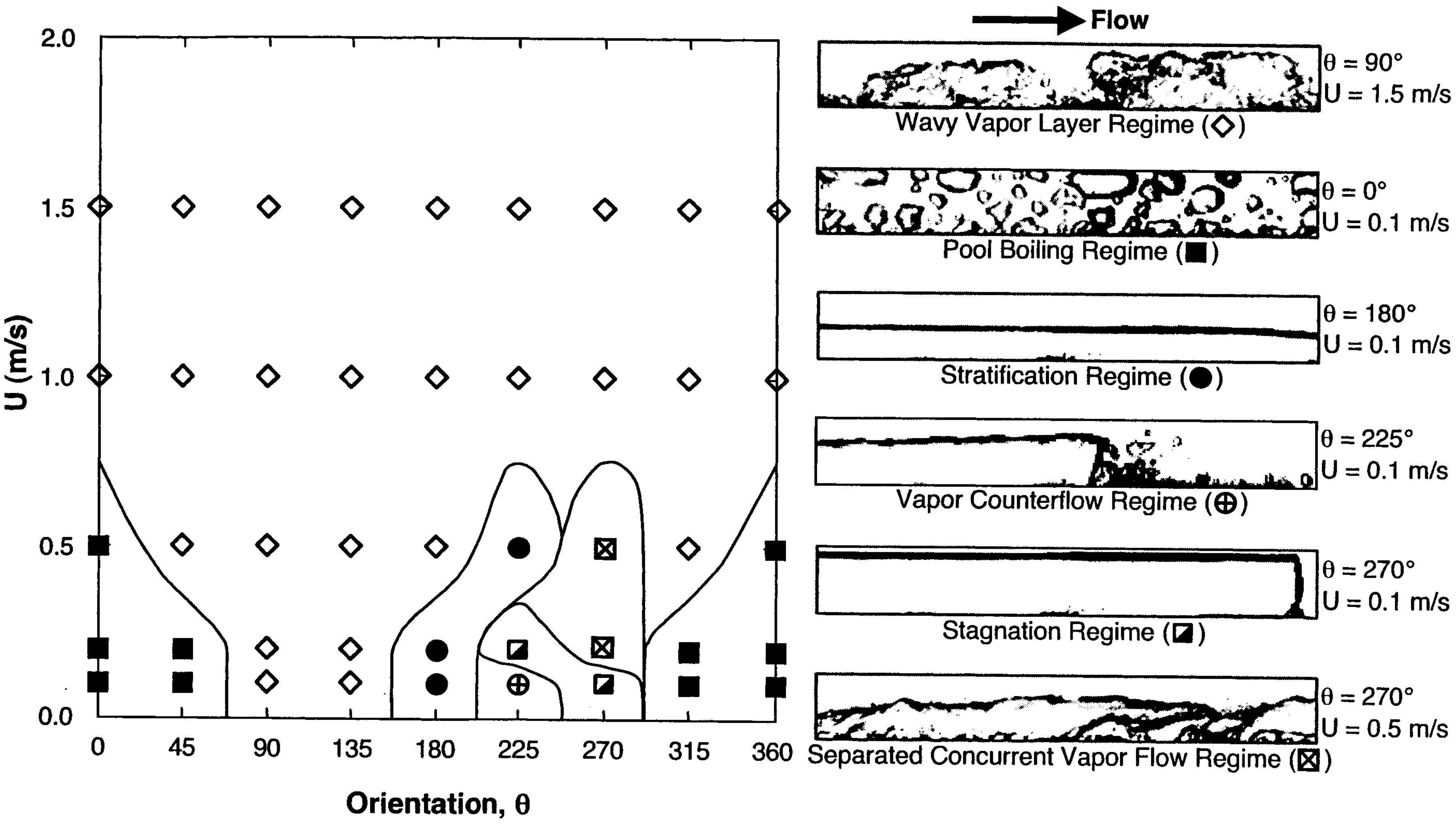

(a)

(b)

Fig. 3.1 (a) CHF regime map. (b) Typical flow characteristics for each regime.

The six CHF regimes are described below in terms of both the shape and temporal behavior of liquid-vapor interface. All the photographs discussed below correspond to the downstream one-third of the heated wall.

3.1.1 Wavy Vapor Layer Regime

As depicted in Fig. 3.1(b), this regime is characterized by large vapor patches which form along the heated wall, resembling a fairly continuous wavy vapor layer. This layer prevents liquid contact with much of the heated wall, producing broad regions of dry wall, except in wetting fronts, located in troughs between vapor patches, where virtually all the heat is dissipated. This regime was encountered at velocities of $U = 1.0$ and 1.5 m/s regardless of orientation and encompasses upflow orientations at lower velocities as well.

Figure 3.2 shows a series of seventeen sequential video images of conditions corresponding to the Wavy Vapor Layer Regime. These images were captured at 1000 fps, which allowed prominent vapor features to be carefully tracked with time. Clearly, the vapor patches and wetting fronts are not stationary, but propagate along the heated wall. The waviness associated with this CHF regime lends credence to the adoption of hydrodynamic instability theory is describing the vapor layer shape, amplitude and propagation speed [20,21].

Figure 3.2 shows the liquid-vapor wavy interface is marred with smaller interfacial disturbances, apparently the result of increased turbulence intensity at high liquid velocities. Galloway and Mudawar [20,21] encountered the same Wavy Vapor

Wavy Vapor Layer Regime

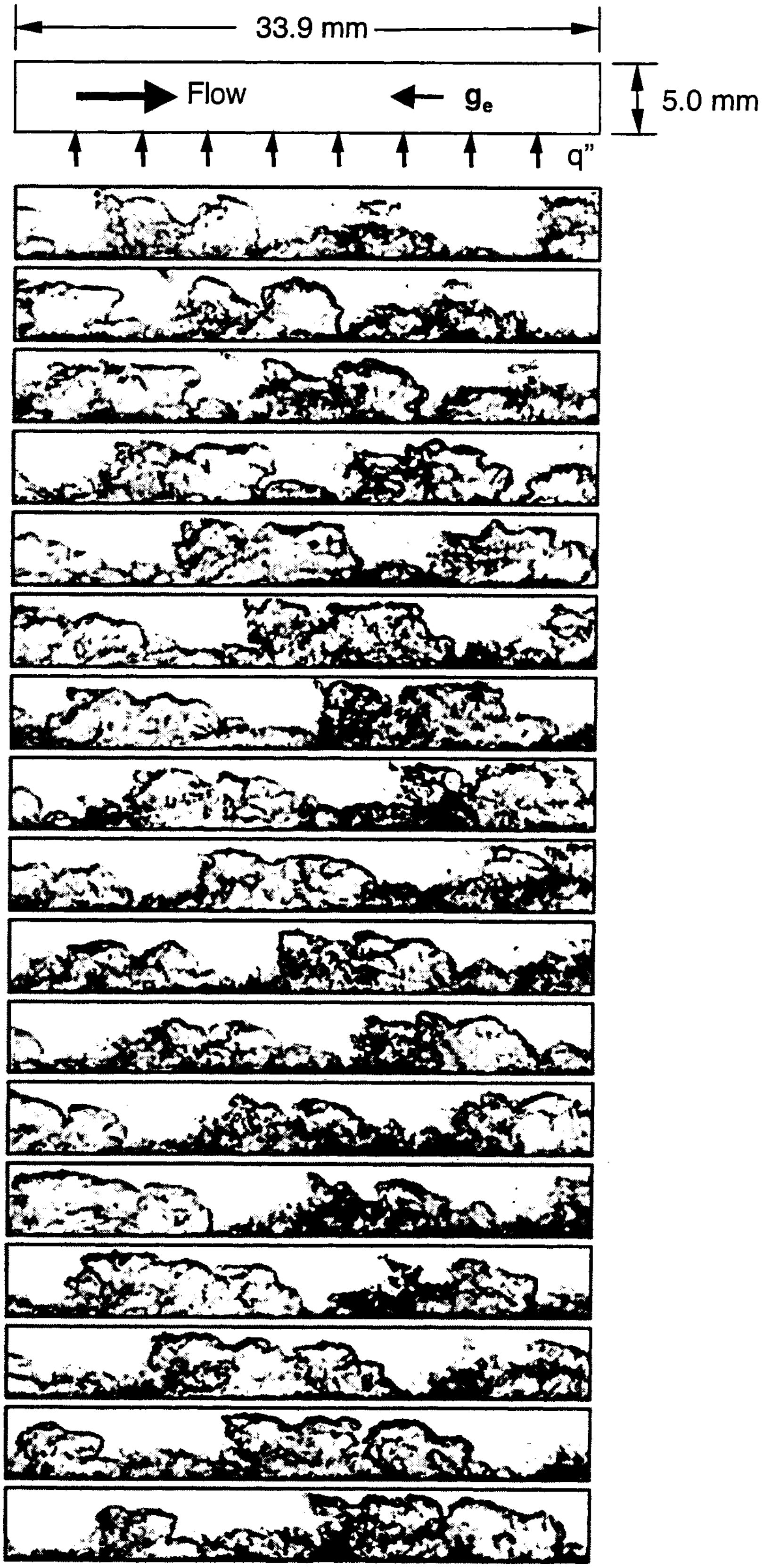

Fig. 3.2 Sequential images of vapor layer at θ = 90°and U = 1.5 m/s.

Layer Regime in vertical upflow along a short heated wall. They too noticed that the wavy vapor layer interface became increasingly marred with small disturbances with increasing velocity.

3.1.2 Pool Boiling Regime

Figures 3.1(a) shows this regime encompasses velocities below 0.5 m/s with the heated wall facing upwards (θ= 315, 0, and 45°). Figure 3.1(b) shows small bubbles coalescing into larger ones, which are detached by buoyancy and driven across the flow channel to the opposite wall, where the vapor accumulates into yet larger vapor masses.

Figure 3.3 shows sequential images of this regime corresponding to $\theta = 0°$ and $U = 0.1$ m/s. While the vapor masses seem to propagate along the heated wall, the speed of propagation is much smaller than in Fig. 3.2, corresponding to $\theta = 90°$ and $U = 1.5$ m/s. The low liquid velocity in Fig. 3.3 produces very mild drag forces on the vapor features, evidenced both by the aforementioned low speed of propagation of vapor masses, as well as the relatively mild deformation in the shape of coalescent bubbles departing normal to the heated wall. This is the primary reason behind the authors' naming of this regime, which is dominated by buoyancy forces. However, even in this Pool Boiling Regime, increasing liquid velocity should help remove vapor along the flow channel and preclude merging of vapor masses between the heated wall and opposite wall.

Fig. 3.3 Sequential images of vapor layer at θ = 0°and U = 0.1 m/s.

3.1.3 Stratification Regime

The same low velocities which caused buoyancy to dominate vapor formation in the previous Pool Boiling Regime are responsible for the formation of a well separated vapor layer which stratified against the heated wall for horizontal and near-horizontal downward-facing wall orientations, $\theta = 180$ and 225°, respectively. As shown in Fig. 3.1(b), this thick continuous vapor layer greatly impeded liquid access to the heated wall, resulting in very low CHF values.

The sequential video images of the stratified vapor layer in Fig. 3.4 show the vapor layer interface is somewhat wavy, but the wavelength is fairly long, exceeding the entire heated length, and has a very small amplitude. This behavior points to hydrodynamic conditions which promote a stable liquid-vapor interface. Such a stable interface is very detrimental to the heat transfer process. An unstable interface, on the other hand, causes both spatial and temporal growth of interfacial amplitude, permitting liquid access to the heated wall.

3.1.4 Vapor Counterflow Regime

This regime as well as the two remaining CHF regimes discussed below are closely related to the relative magnitude of liquid inertia and buoyancy force for downflow orientations at low velocities. As shown in Fig. 3.1(a), the Vapor Counterflow Regime was encountered at $\theta = 225°$ for $U = 0.1$ m/s. At this low velocity, the liquid drag force exerted downwards upon the vapor is far too weak to overcome the opposing buoyancy force. The later pushes vapor backwards (upwards) against the incoming

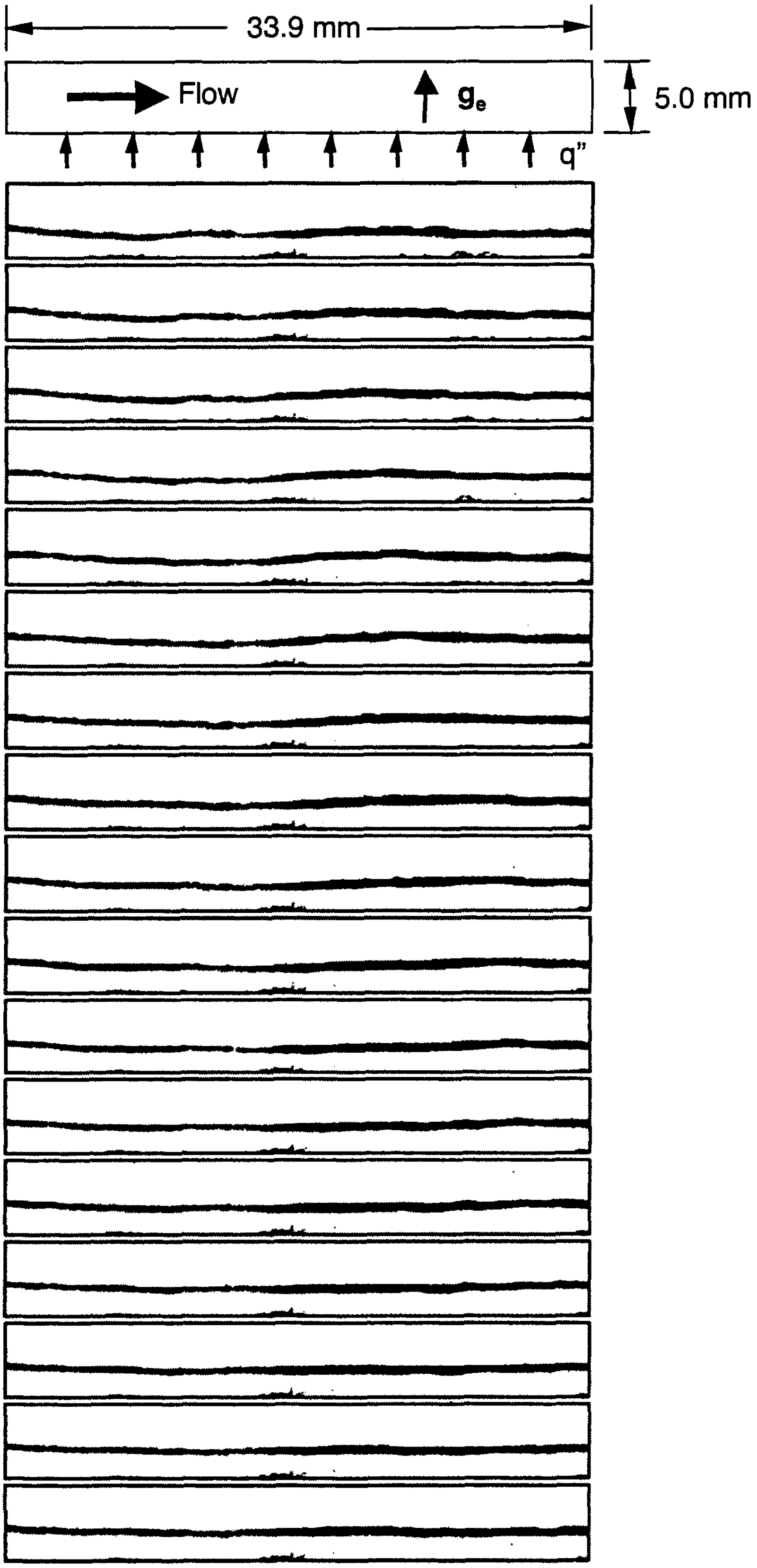

Stratification Regime

Fig. 3.4 Sequential images of vapor layer at θ = 180° and U = 0.1 m/s.

liquid. The sequential images in Fig. 3.5 show the thick coalescent vapor layer moving backwards, albeit very slowly, as liquid continues to make contact over the downstream portion of the heated wall.

3.1.5 Stagnation Regime

This regime was encountered when the liquid drag force and inertia came into balance, effectively freezing a thick coalescent vapor mass in place. As shown in Fig. 3.1(a), this condition occurred at $\theta = 225°$ for $U = 0.2$ m/s and $\theta = 270°$ for $U = 0.1$ m/s. Figure 3.1(b) and the sequential images in Fig. 3.6 show liquid contact with the downstream section of the heated wall is available over of a very small region. The sequential images show the thick, continuous vapor layer is virtually stationary. This behavior produced the lowest CHF values of the present study. In fact, at $\theta = 225°$, CHF at 0.1 m/s (corresponding to the Vapor Counterflow Regime) was actually greater than CHF at the higher velocity of 0.2 m/s corresponding to the Stagnation Regime.

3.1.6 Separated Concurrent Vapor Flow Regime

The stagnant vapor layer described in the previous section was purged from the channel with an increase in inlet liquid velocity which allowed the liquid drag force to overcome buoyancy. Figure 3.1(a) shows this regime was encountered at $\theta = 270°$ for $U = 0.2$ and 0.5 m/s. This regime was complicated by significant disturbances along the vapor-liquid interface and bubble formation in a thin liquid layer at the heated wall which was, for the most, separated from the bulk liquid flow. The sequential images in Fig. 3.7

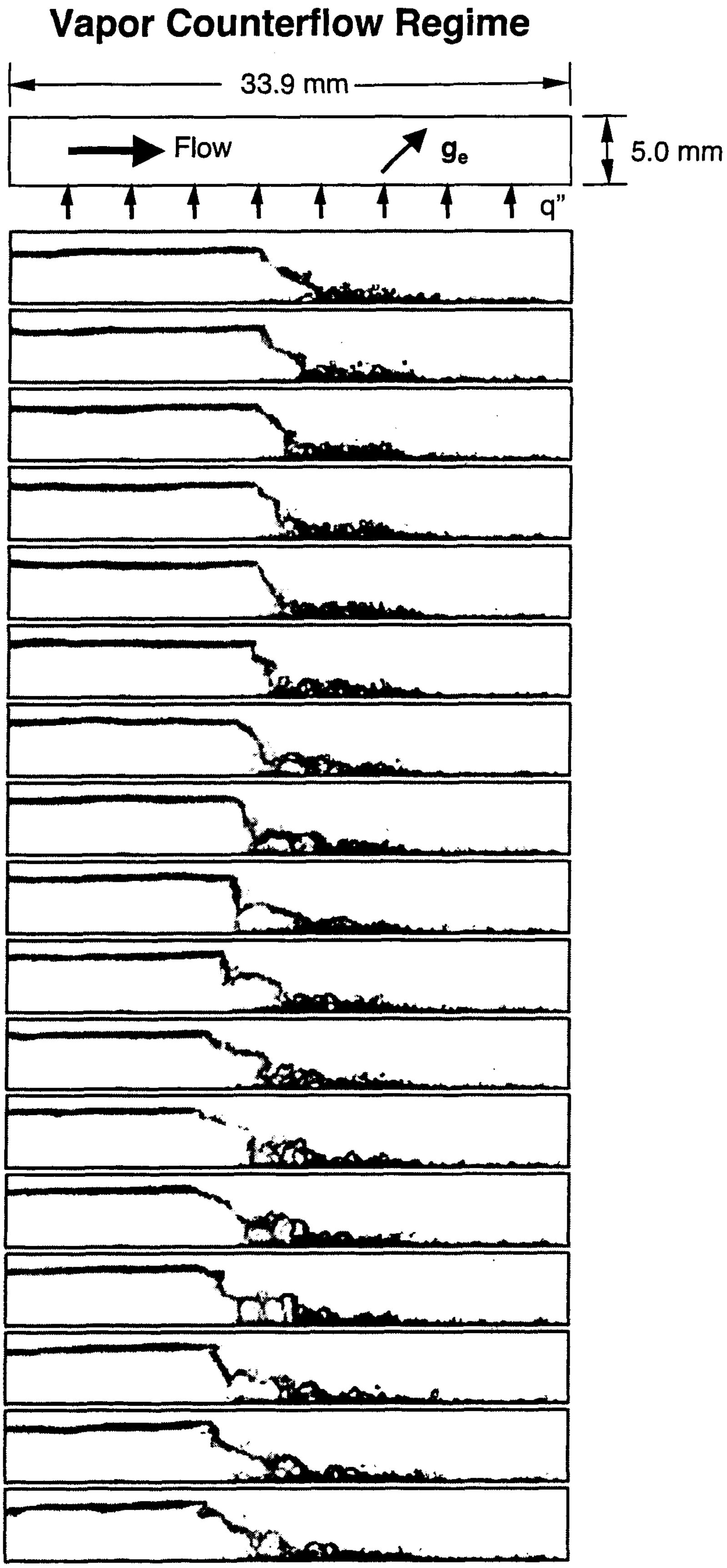

Fig. 3.5 Sequential images of vapor layer at θ = 225°and U = 0.1 m/s.

Stagnation Regime

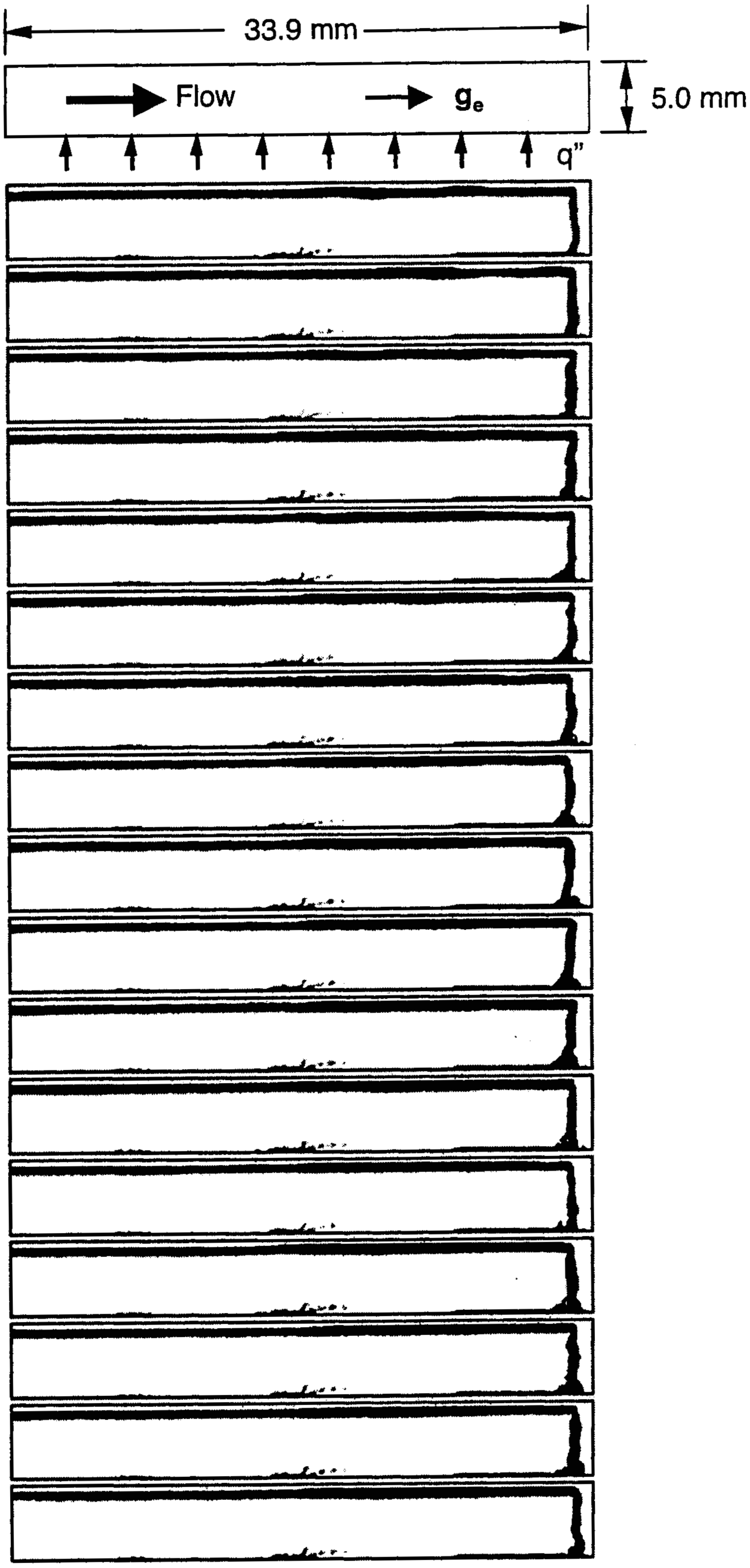

Fig. 3.6 Sequential images of vapor layer at θ = 270°and U = 0.1 m/s.

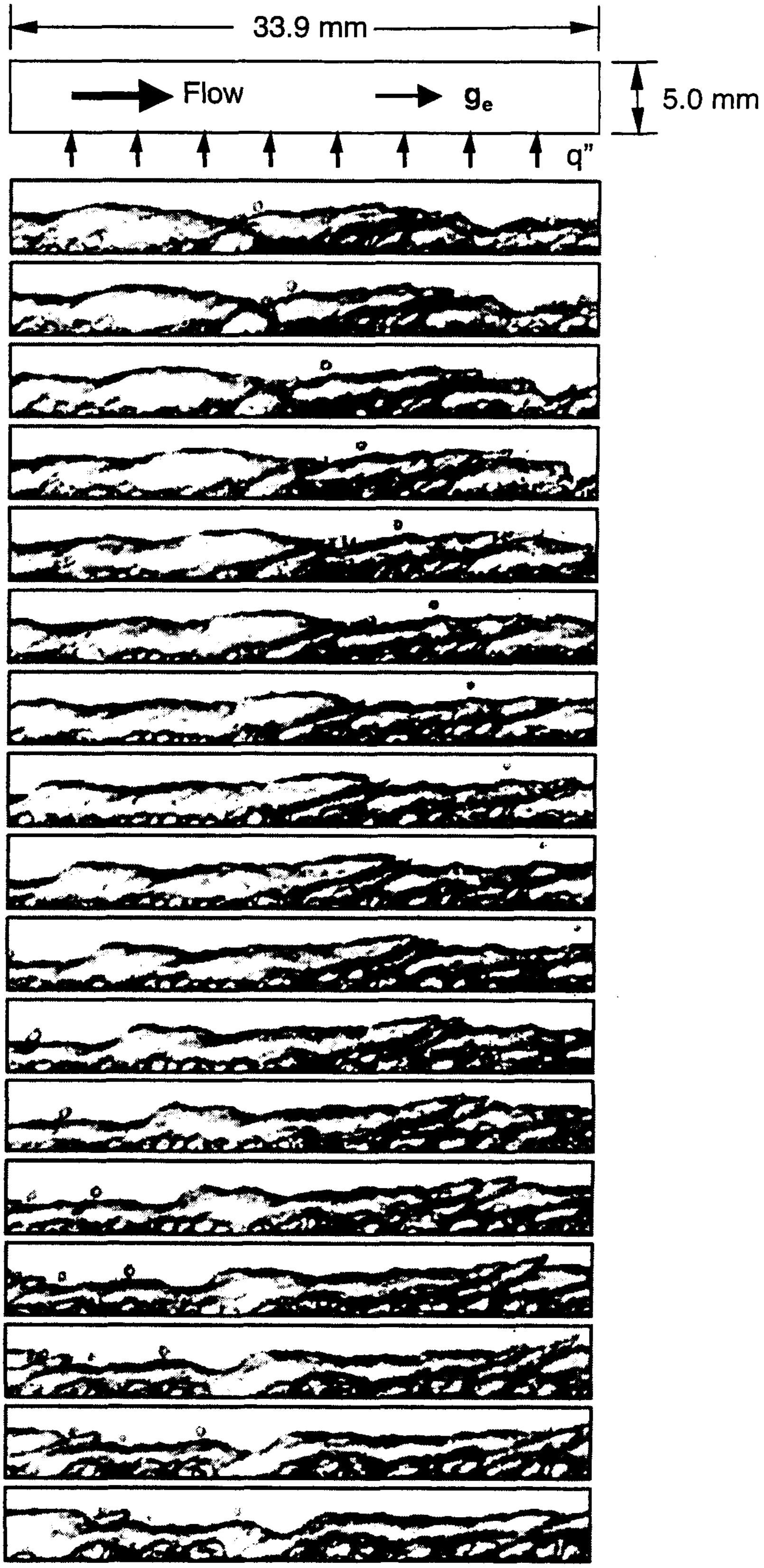

Fig. 3.7 Sequential images of vapor layer at θ = 270°and U = 0.5 m/s.

show the vapor layer interface propagating with a large wavelength and small amplitude along the channel. Figure 3.1(a) shows increasing liquid velocity at this orientation from 0.5 m/s to 1.0 m/s causes the vapor layer interface to become unstable, marking a transition to the Wavy Vapor Layer Regime described above.

3.2 Heat Transfer Results

3.2.1 Boiling Curves

Figures 3.8(a)–(c) show boiling curves measured by the heater's downstream thermocouples at $\theta = 0, 90, 180$ and 270° and $U = 0.1, 0.5$ and 1.0 m/s, respectively. For $U = 0.1$ m/s, the boiling curves are somewhat irregular and show significant differences for different orientations. These differences can be explained by the substantial differences in flow regime encountered at this low velocity. These differences are most obvious at CHF, where the horizontal flow with an upward-facing heated wall ($\theta = 0°$) and vertical upflow ($\theta = 90°$) are shown yielding much greater CHF values than both horizontal flow with a downward-facing heated wall ($\theta = 180°$) and downflow ($\theta = 270°$).

Figure 3.8(b) shows relatively more consistent boiling curves for $U = 0.5$ m/s, which start with a fairly linear single-phase liquid region and a gradual transition to the nucleate boiling region. Here again there are significant differences in CHF for the four orientations, following essentially the same trend depicted in Fig. 3.8(a) for $U = 0.1$ m/s.

Figure 3.8(c) shows far greater consistency in boiling curves for $U = 1.5$ m/s than for the two lower velocities. The high liquid inertia at 1.5 m/s seems to overcome

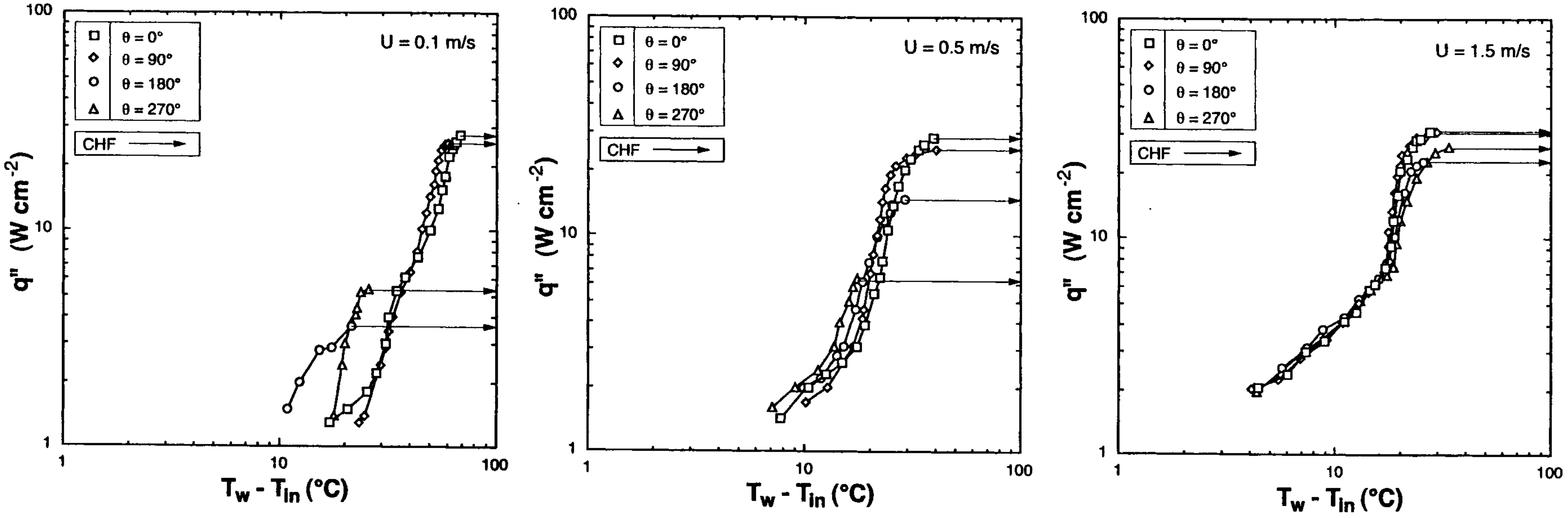

(a) (b) (c)

Fig. 3.8 Effects of flow orientation on boiling curve for (a) U = 0.1 m/s, (b) U = 0.5 m/s, and (c) U = 1.5 m/s.

virtually all buoyancy effects, yielding closer results for the single-phase liquid region, nucleate boiling region, and even CHF itself.

Figure 3.9 compares boiling curves for vertical upflow ($\theta = 90°$) and $U = 0.1$, 0.5 and 1.5 m/s, conditions which fall into the Wavy Vapor Layer Regime. The three boiling curves exhibit all the expected effects of increasing flow velocity: an upward shift in the single-phase liquid region, followed by a merging of data for different velocities in the nucleate boiling region, and culminating in increasing CHF values with increasing velocity.

3.2.2 CHF Results

Figure 3.10 shows the variation of CHF with orientation for the five velocities tested. For all velocities, CHF increases from $\theta = 0°$ to a maximum around 45°, followed by a decrease to a minimum between 180 and 270°, before recovering again to the $\theta = 0°$ value. The three lowest velocities of $U = 0.1$, 0.2 and 0.5 m/s exhibit strong variations of CHF with orientation. These velocities produce very small CHF values in the range of $180 < \theta < 270°$. This further demonstrates the significance of buoyancy force compared to liquid inertia at low flow velocities. As illustrated in Figs. 3.1(b) and 3.4-3.7, the relatively weak liquid inertia enables buoyancy to dominate vapor behavior, causing vapor stratification against the heated wall for $\theta = 180°$, and inducing Vapor Counterflow, Stagnation, or Separated Vapor Concurrent Flow for $\theta = 225$ and 270°. Clearly, downflow and downward-facing heated wall orientations should be avoided at low velocities.

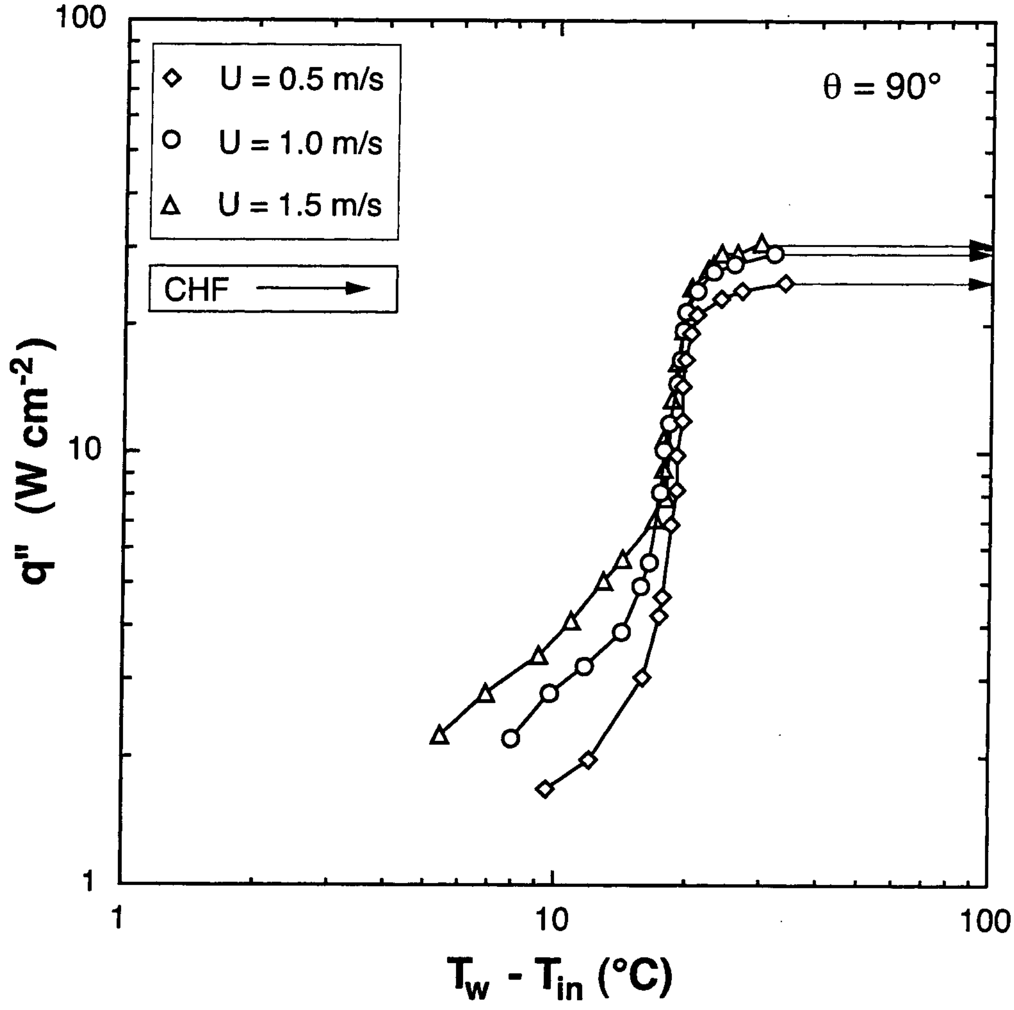

Fig. 3.9 Effects of velocity on boiling curve for θ = 90°.

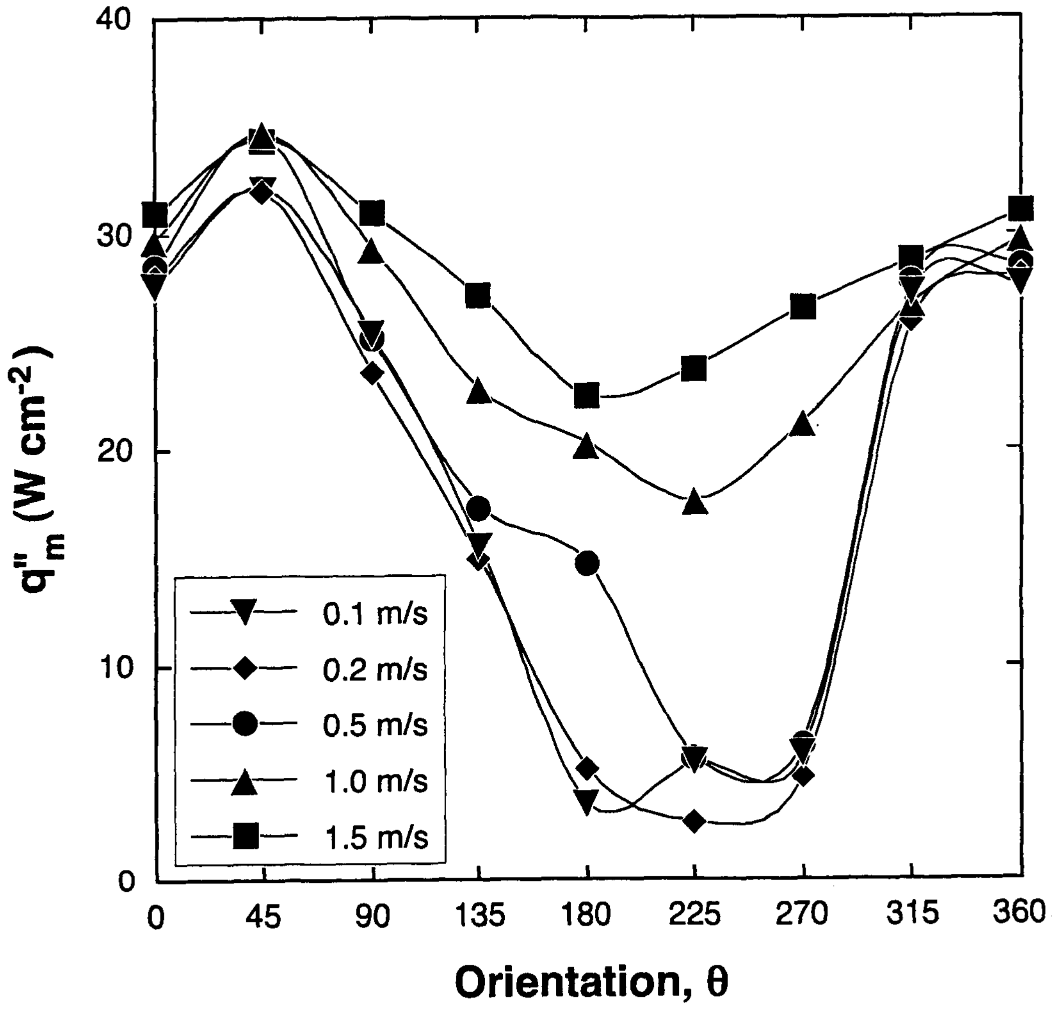

Fig. 3.10 CHF variation with orientation and flow velocity.

Figure 3.10 shows the two highest velocities, 1.0 and 1.5 m/s, cause appreciable diminution in the orientation effects on CHF. Nonetheless, buoyancy still influences CHF at these two velocities. A CHF maximum at $\theta = 45°$ can be explained by the buoyancy force both aiding vapor removal away from the heated wall as well as along the channel. At $\theta = 0°$, buoyancy is perpendicular to the heated wall but does not aid the vapor removal along the channel, while the opposite is true for $\theta = 90°$. CHF for $U = 1.0$ and 1.5 m/s decreases for all downflow and downward-facing heated wall orientations, but to a much lesser degree than for the lower velocities.

CHAPTER 4

VOID FRACTION ESTIMATION

4.1 Void Fraction Estimation Method

As shown in Figs. 2.6(a)-(b), the vapor generally appears very dark and the liquid white in the captured images. Based upon this strong contrast between the phases and thin rectangular cross-section of the channel, it is possible to use image analysis software to estimate the void fraction. Figure 4.1 outlines the basic operations involved. The video images captured by the Canon camera during the transient CHF tests were first downloaded into an image analysis program. The captured video images consist of 256 levels of gray-scale color. Image quality was first enhanced by increasing the contrast. The images were then converted to a 2 color binary image using a threshold operation. The threshold value was adjusted until the liquid-vapor interface in the binary image resembled that in the original image as closely as possible. Next the area below the liquid-vapor interface was filled black. This series of operations resulted in the vapor and liquid phases consisting of totally black and totally white areas, respectively.

To calculate void fraction, a portion of the image was selected which extended from the heated wall to the opposite wall of the channel, as shown in Fig. 4.1. The image analysis software estimates the void fraction as the area occupied by the black pixels

Original Video Image

Modified Video Image

Binary Image

Filled Binary Image

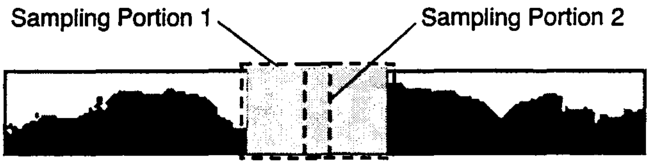

Sampling Area

Fig. 4.1 Procedure for void fraction estimation.

(vapor) in the selected portion divided by the total area of the same portion. This calculation method was applied to many thousands of images in a video file using customized macro subprograms. A wide portion (sampling portion 1 in Fig. 4.1) was used to compute the overall trends of space-averaged void fraction. Void fraction estimation can be refined by using a thinner sampling portion. Figures 4.2(a)-(b) illustrate the use of a thin sampling portion to generate void fraction, α, records. Notice both the small magnitude of α for subcooled flow and therefore far greater difficulty in interpreting void fraction trends compared to near-saturated flow.

Error associated with this void fraction estimation method comes in two forms. First, the method assumes that the flow is two-dimensional, meaning the vapor formations extend uninterrupted perpendicular to the camera viewing direction. These errors were minimized by both the rectangular cross-section and very short width (2.5 mm) of the flow channel. Secondly, there is some error associated with the threshold operation, since it is not possible to exactly duplicate the information contained in a 256 color image with a 2 color image, and some of the small vapor bubbles entrained in the bulk liquid flow may not be accounted for.

4.2 Void Fraction Results

Figure 4.3(a) shows the void fraction record from the last steady-state point before CHF to power cut-off after CHF for vertical upflow at $U = 1.5$ m/s and $\Delta T_{sub,o} = 3$ °C. Each second produces 30 void fraction data points. The void fraction was calculated at a location one-sixth the heated length from the downstream edge of the heater. A wide

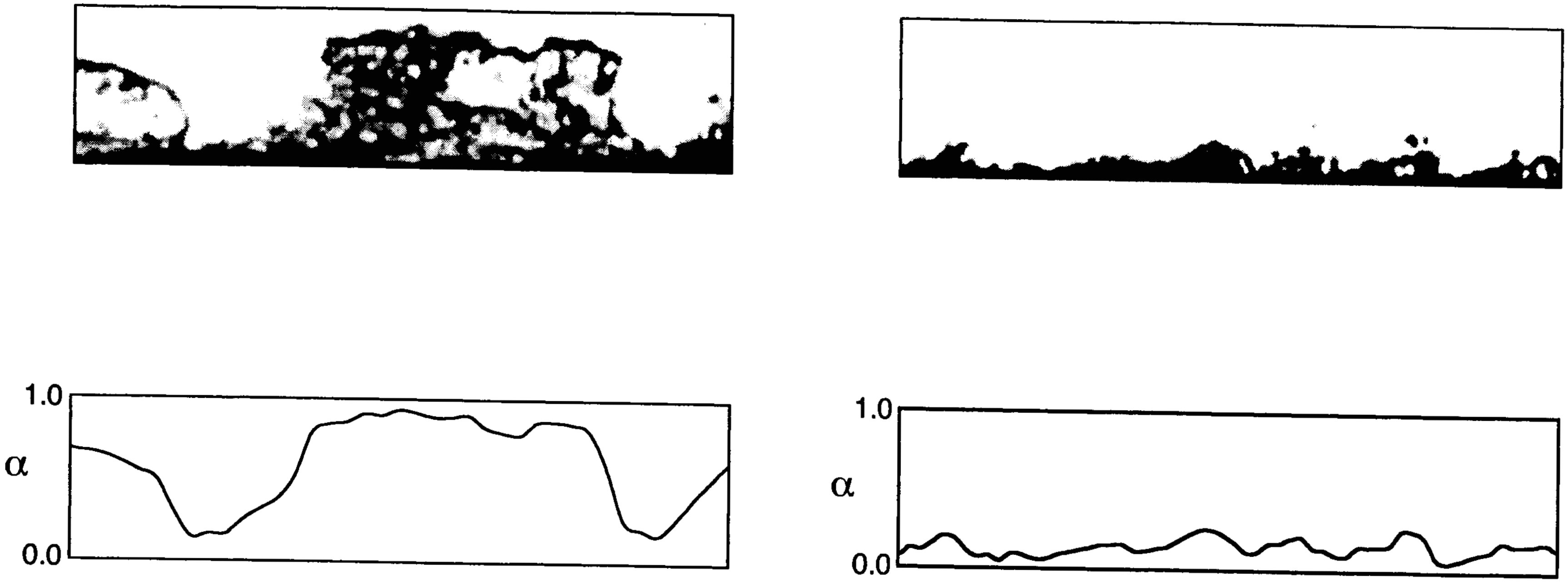

(a) $\Delta T_{su,b,o} = 3$ °C

(b) $\Delta T_{sub,o} = 30$ °C

Fig. 4.2 Video image prior to CHF and calculated void fraction for (a) $\Delta T_{sub,o} = 3$ °C and (b) $\Delta T_{sub,o} = 30$ °C.

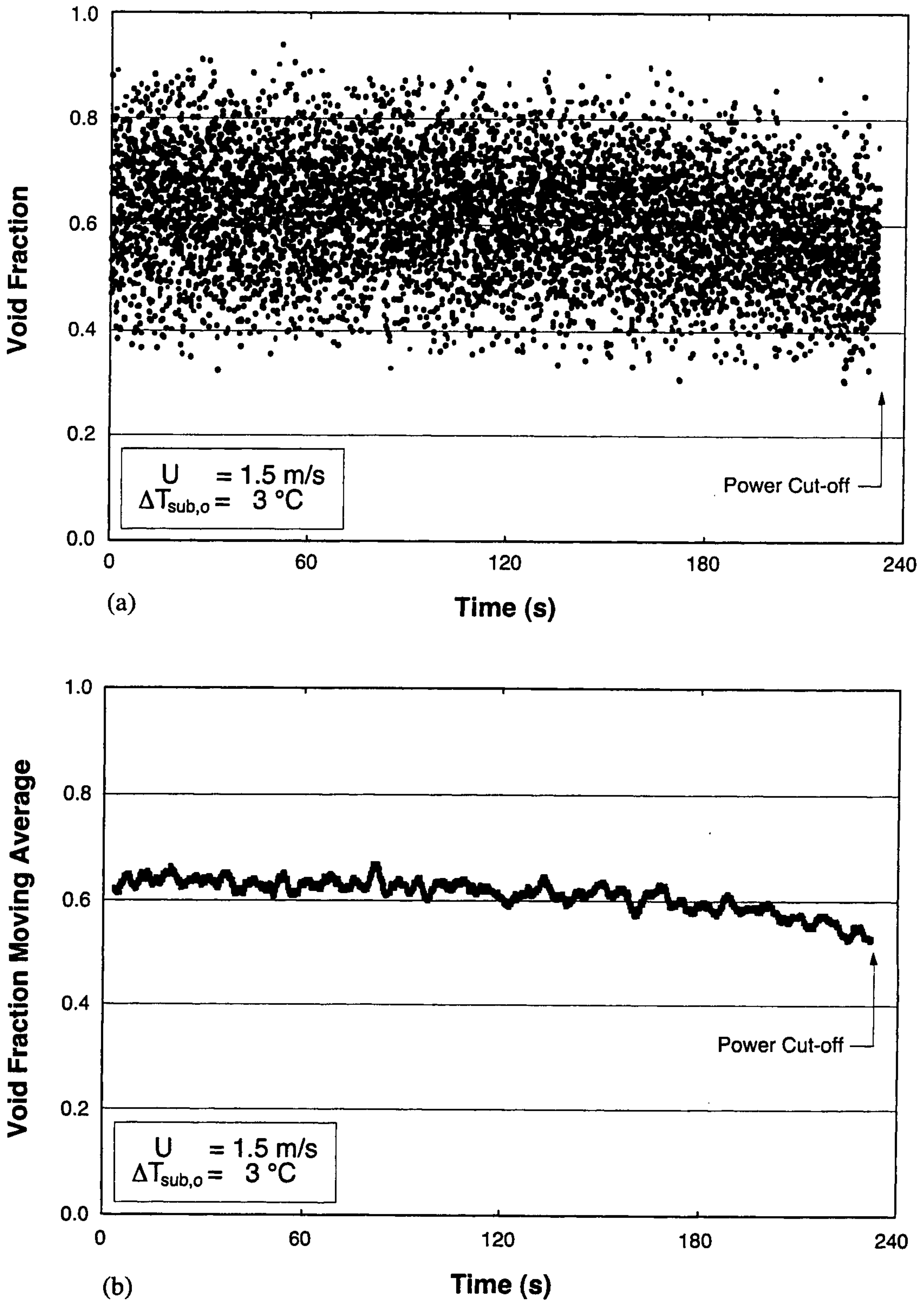

Fig. 4.3 Variations of (a) instantaneous void fraction and (b) void fraction moving average during CHF transient for vertical upflow at U = 1.5 m/s and $\Delta T_{sub,o}$ = 3 °C.

sampling portion was used to generate this plot, which causes some truncation of peak and trough values but effectively captures the overall trend of mean vapor layer thickness. Periodic rises and falls in void fraction, which are more evident in Fig. 4.2(a), are manifest in the form of data scatter about a void fraction mean.

Figure 4.3(b) shows the moving average of the void fraction data shown in Fig. 4.3(a), which, for a particular time *t*, is defined as the average of the void fraction at that time and the 99 prior video images.

$$\overline{\alpha}(t) = \frac{1}{100}\sum_{i=0}^{99}\alpha(t - i\cdot\Delta t) \tag{4.1}$$

A key benefit of the moving average is its effectiveness at eliminating the data scatter and tracking the mean thickness of the wavy vapor layer.

Figure 4.4(a) and 4.4(b) show plots of void fraction and void fraction moving average, respectively, for U = 1.5 m/s and $\Delta T_{sub,o}$ = 30 °C. These two figures show significantly lower void fraction values compared to $\Delta T_{sub,o}$ = 3 °C, Figs. 4.3(a) and 4.3(b), because of the appreciable reduction in net vapor generation in subcooled flow.

Interestingly, Figs. 4.3(a) and 4.3(b) show the vapor layer maintaining a somewhat constant mean vapor layer thickness during the CHF transient until the power cut-off point. A slight decrease in void fraction is detected as the vapor layer begins to develop into a continuous vapor film.

Figures 4.4(a) and 4.4(b) show the void fraction trend is far more drastic for $\Delta T_{sub,o}$ = 30 °C. This is because small changes in the mean vapor layer thickness have an appreciable impact on a predominantly low void fraction (i.e., thin vapor layer) flow. This sensitivity is greatly diminished for $\Delta T_{sub,o}$ = 3 °C where the overall void fraction

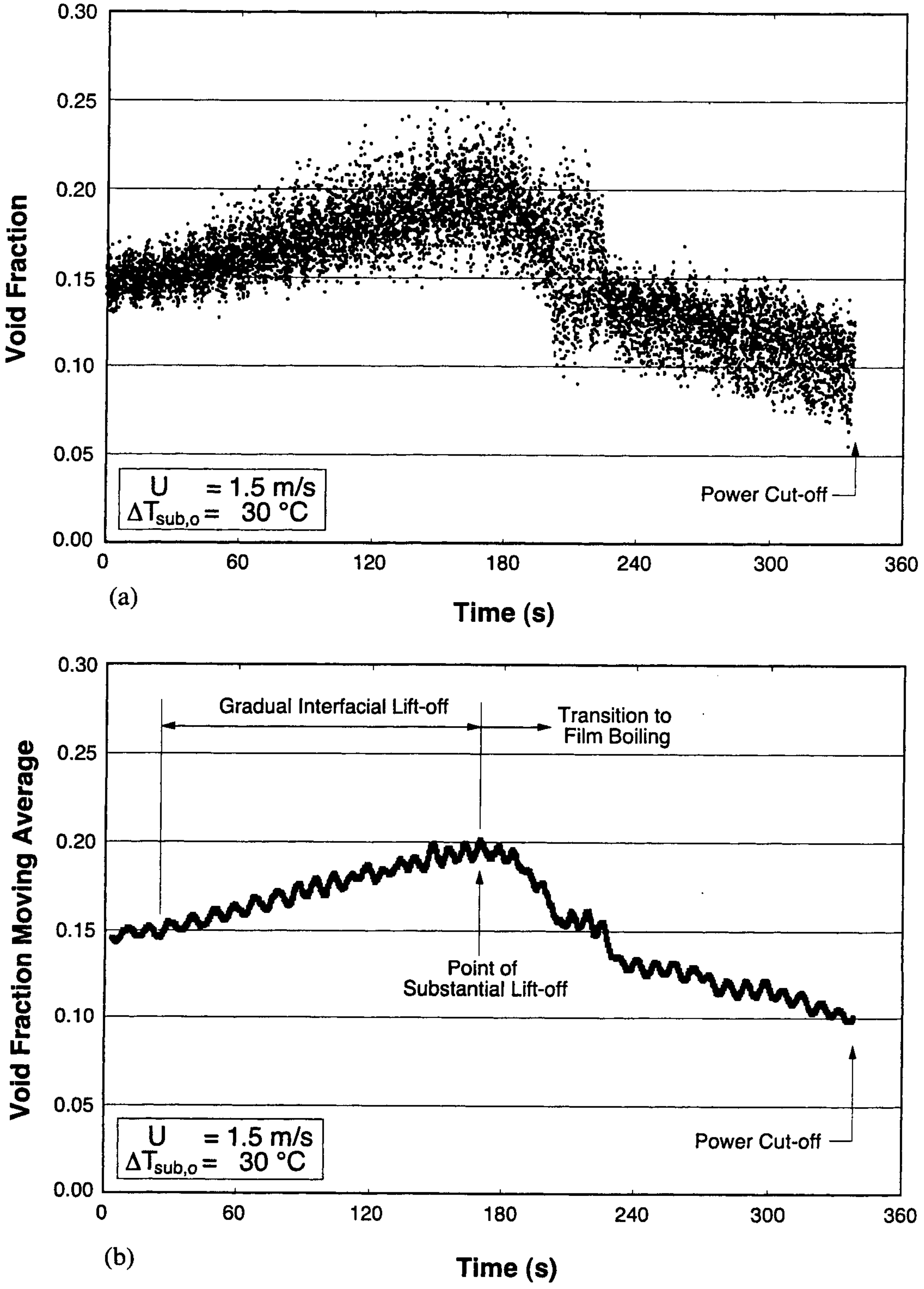

Fig. 4.4 Variations of (a) instantaneous void fraction and (b) void fraction moving average during CHF transient for vertical upflow at $U = 1.5$ m/s and $\Delta T_{sub,o} = 30$ °C.

values are very large to start with. Most notably, the void fraction records for $\Delta T_{sub,o} = 30$ °C can actually detect wetting front lift-off during the CHF transient quite well. The gradual initial increase in void fraction points to an increasing number of wetting fronts incurring lift-off. This process seems to reach some peak value (indicated in Fig. 4.4(b) as "point of substantial lift-off") before the vapor layer begins to thin down to a continuous vapor film.

Figures 4.4(a) and 4.4(b) are the first strong evidence of the validity of the interfacial lift-off mechanism for subcooled flow boiling CHF. In fact, these figures provide a fairly detailed depiction of both the lift-off process and eventual transition to film boiling.

Future work should therefore focus on determining the partitioning of wall energy between sensible and latent heat components to derive accurate energy balance framework in which to incorporate the Interfacial Lift-off Model.

CHAPTER 5

CHF MODEL

5.1 Statistical Characterization of Interfacial Features

As indicated in Fig. 1.4, six CHF regimes have been previously identified by the authors for saturated flow. The present paper concerns modeling of CHF corresponding to the wavy vapor layer regime, which was observed for most velocities and orientations.

In the present study, a 2 s video sequence was recorded at a rate of 1000 frames/s at the middle and outlet sections of the heated wall. Figures 5.1, 5.2, and 5.3 depict the development of the wavy vapor layer just prior to CHF at $\theta = 135°$ for $U = 0.5$, 1.0 and 1.5 m/s, respectively. Seventeen sequential video frames are presented in each figure for each of the middle and outlet sections. The bottom edge of each image represents the heated wall and the upper edge the opposite plastic wall of the flow channel. The time elapsed between consecutive frames is 0.00025 s. Aside from enabling the sizing of interfacial features, the sequential frames facilitate tracking the propagation of the wavy vapor layer along the heated wall. Figures 5.1-5.3 clearly support Galloway and Mudawar's [20,21] depiction of a fairly continuous wavy vapor layer (which develops prior to CHF) travelling along the wall while permitting liquid contact only in wetting fronts, located in the troughs of the interfacial waves.

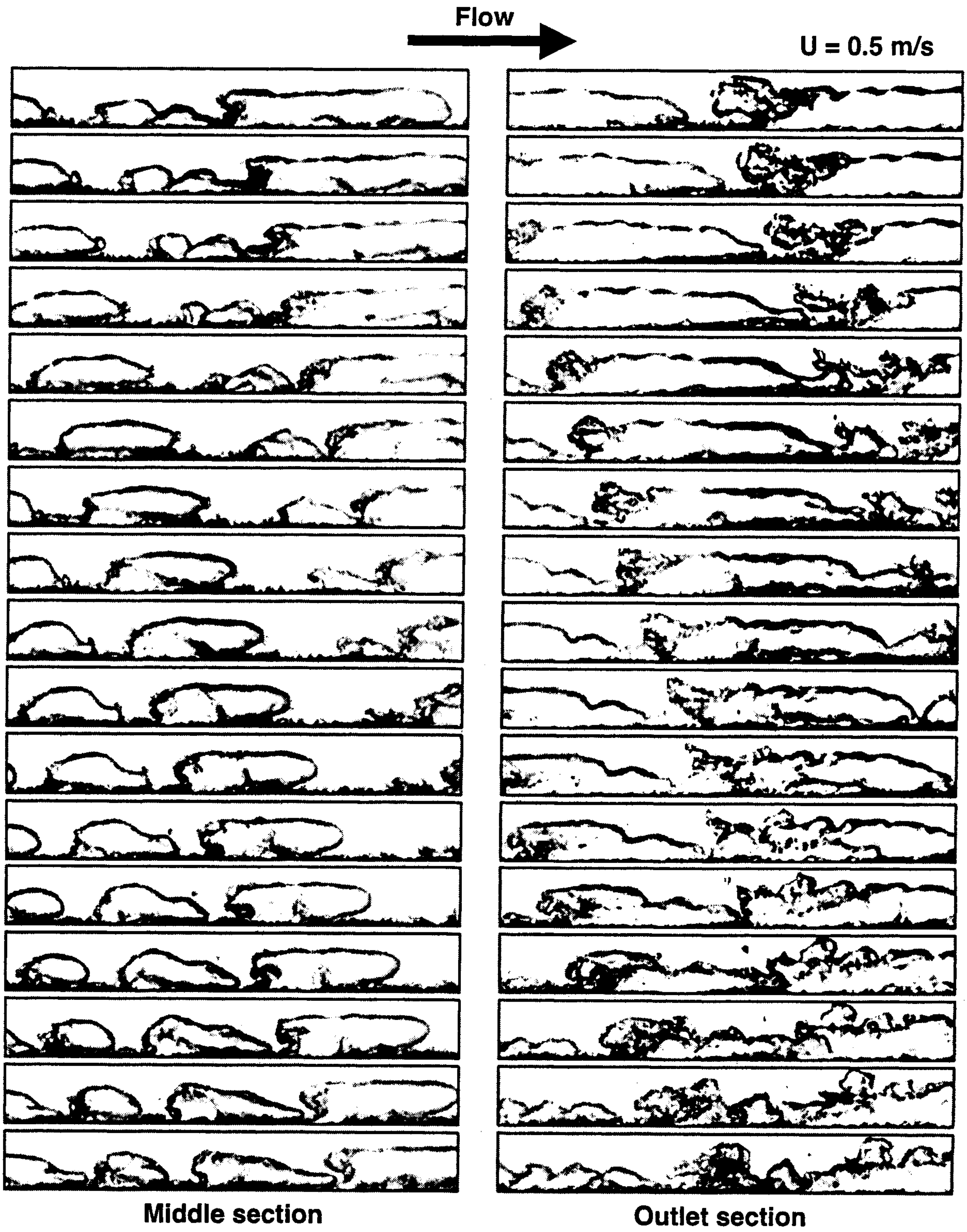

Fig. 5.1 Sequential images of wavy vapor layer at $\theta = 135°$, $\Delta T_{sub,o} = 3$ °C and U = 0.5 m/s.

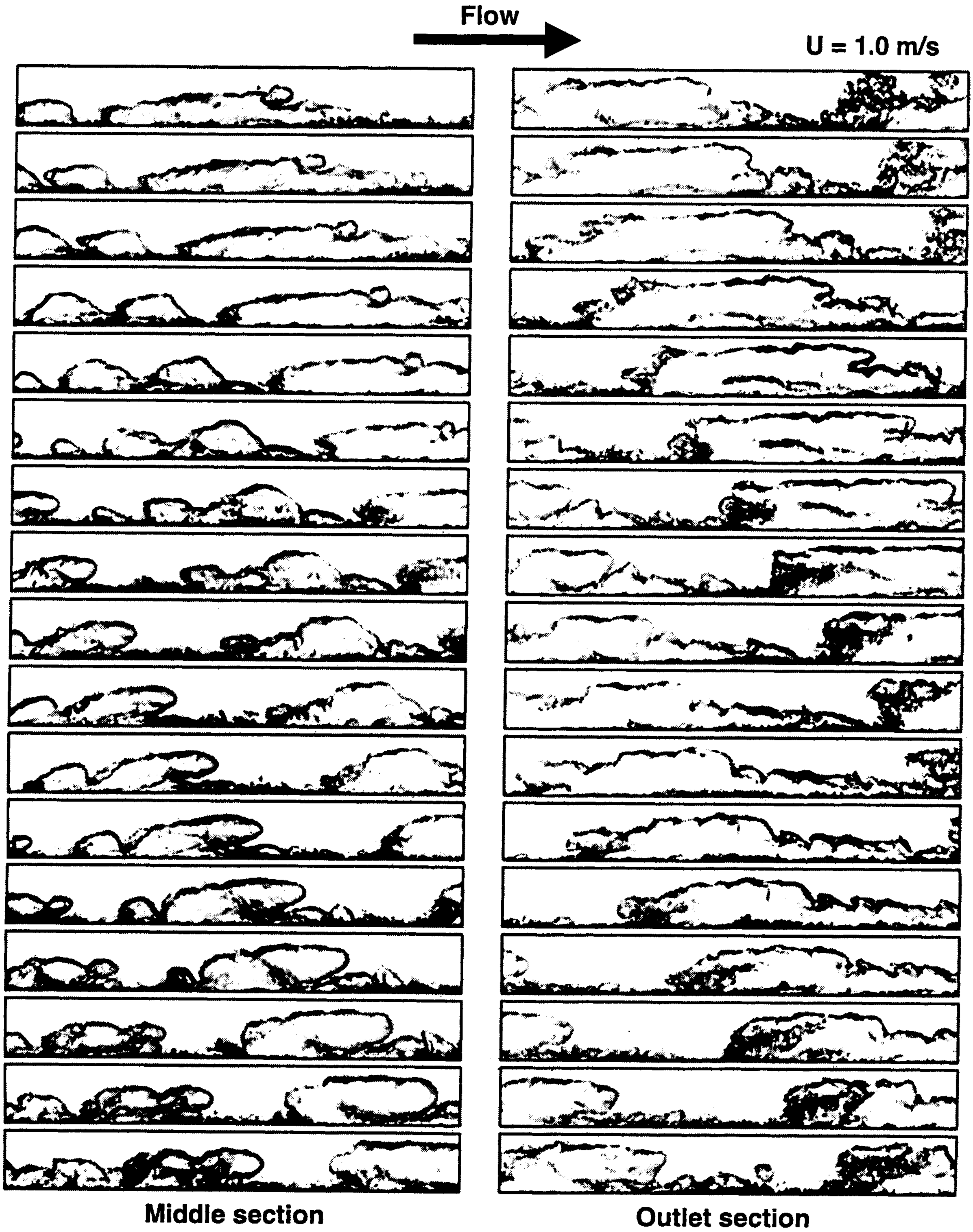

Fig. 5.2 Sequential images of wavy vapor layer at $\theta = 135°$, $\Delta T_{sub,o} = 3$ °C and U = 1.0 m/s.

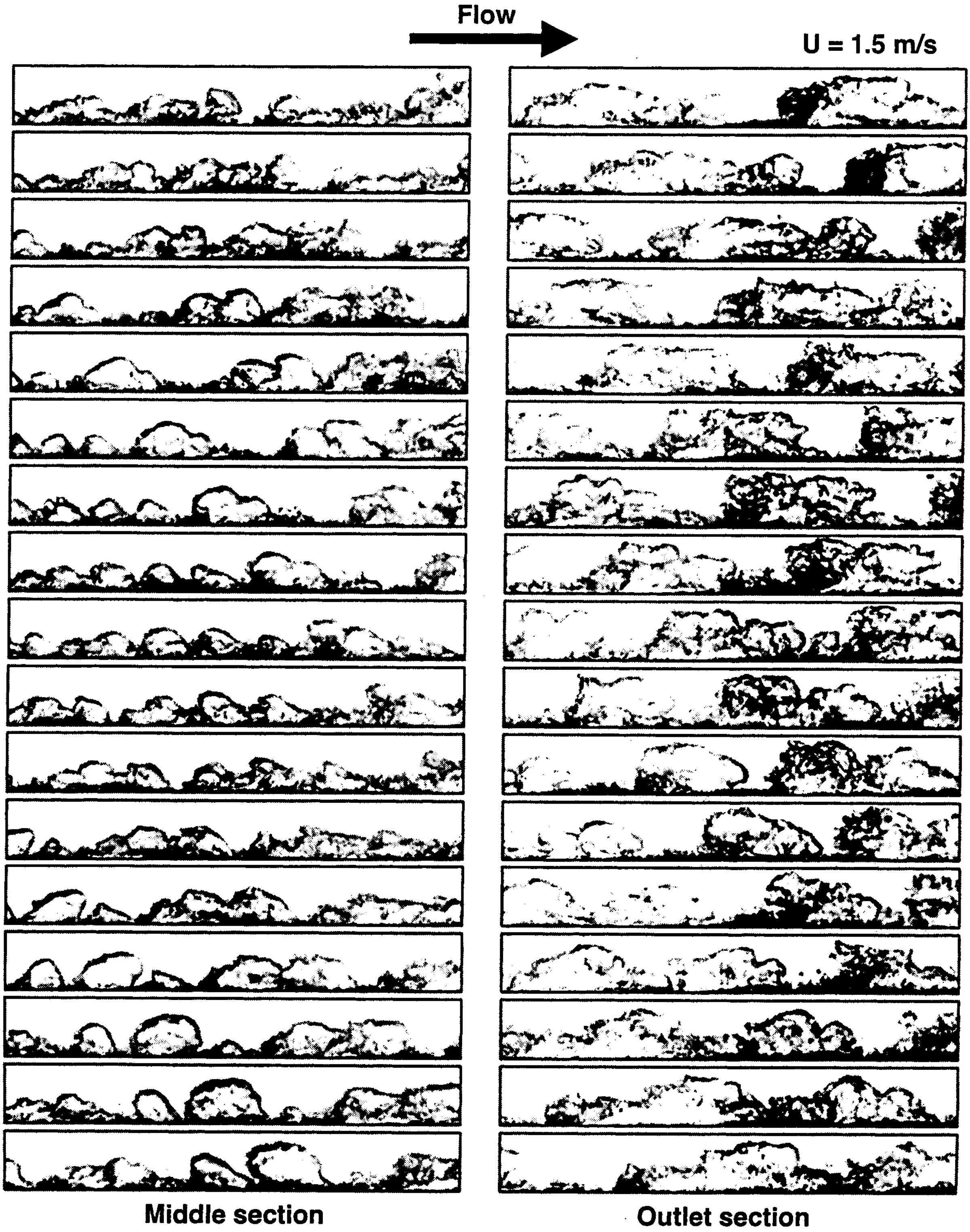

Fig. 5.3 Sequential images of wavy vapor layer at $\theta = 135°$, $\Delta T_{sub,o} = 3$ °C and U = 1.5 m/s.

Interfacial parameters describing both the size and shape of the wavy vapor layer were carefully measured and statistically averaged to explore the vapor layer's development along the heated wall. These parameters, which are illustrated in Fig. 5.4a, consist of vapor "patch" length, λ_{meas}, maximum height, h_{meas}, and length of region of liquid contact with the surface between adjacent patches, w_{meas}. The measured dimensions were averaged for sets of 30 frames, which was deemed a statistically acceptable sample since additional frames had little effect on the calculated average.

The CHF Interfacial Lift-off model is based on an idealized sinusoidal liquid-vapor interface characterized by a wavelength, λ, and amplitude, δ, as illustrated in Fig. 5.4b. The idealized wavelength is defined as the distance between consecutive wetting fronts, hence it is the sum of average vapor length and average wetting front length. When approximating a series of observed vapor patches with a sinusoidal profile, the interfacial amplitude is half the measured height, and the wetting front length of the idealized interface is the same as the measured one. Therefore, the following definitions relate the measured quantities to the idealized ones,

$$\lambda = \overline{\lambda}_{meas} + \overline{w}_{meas} , \tag{5.1}$$

$$\delta = \frac{1}{2}\overline{h}_{meas} , \tag{5.2}$$

and

$$w = \overline{w}_{meas} . \tag{5.3}$$

Poor lighting for certain velocities and orientations prevented the capture of high resolution frames from which interfacial measurements could be made. Therefore, the data for those cases are not available. Furthermore, velocities of 0.5 m/s or smaller

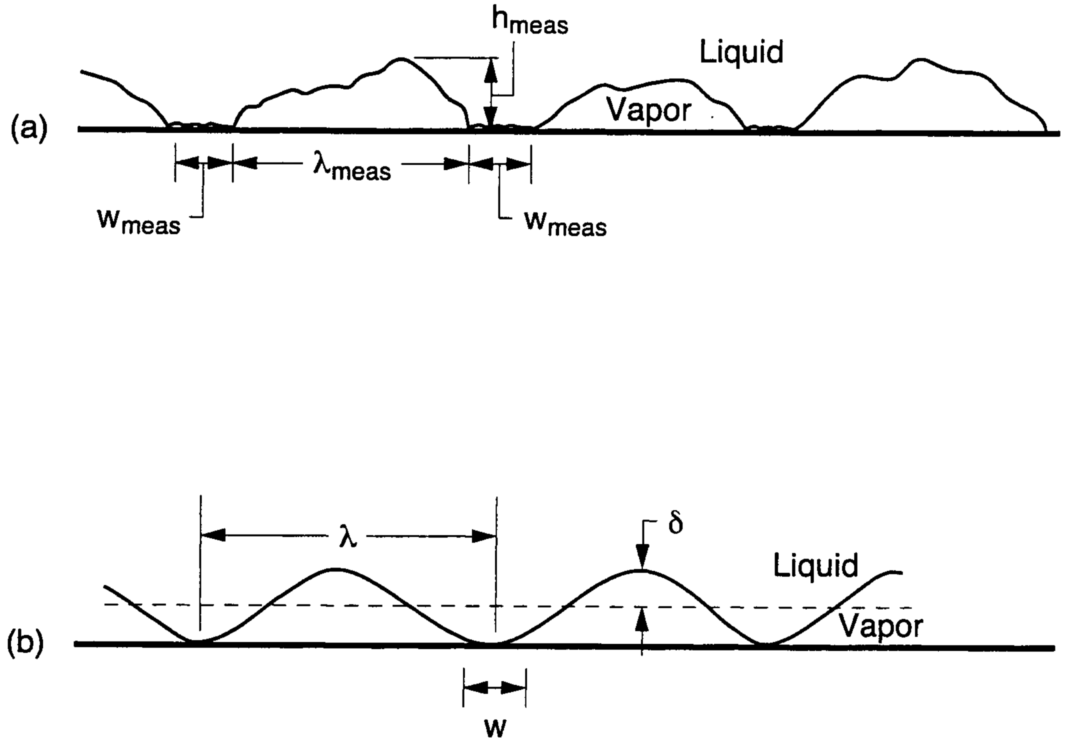

Fig. 5.4 Definitions of vapor layer dimensions for (a) flow visualization study and (b) idealized wavy vapor layer in CHF model.

produced vapor patches which extended beyond the length of the video frame and could not be accurately sized. Table 5.1 shows the interfacial characteristics for conditions which could be carefully measured and statistically characterized. At the outlet section, the wavelength, λ, and amplitude, δ, of the vapor layer both increase compared with those in the middle section, as depicted in Figs. 5.1 to 5.3. The wetting front length, w, between adjacent vapor patches also increases in the flow direction. Statistical averages for each section reveal this wetting front length increases in proportion to the vapor wavelength such that it remains approximately the same fraction of the interfacial wavelength, λ. This is indicated by a ratio, b, defined as

$$b = \frac{w}{\lambda} . \tag{5.4}$$

As shown in Table 5.1, this ratio is fairly insensitive to velocity or flow orientation.

5.2 CHF Modeling

5.2.1 Rationale

The present model is based on the observation that a wavy liquid-vapor develops along the heated wall and permits liquid cooling only in discrete wetting fronts. Therefore, the heat is transferred to the liquid by means of vigorous boiling only in the wetting fronts. The interfacial waviness is a result of instability between the liquid and vapor phases. The phase velocity difference acts as a destabilizing effect while surface tension tends to maintain interfacial stability. Body force may be stabilizing or destabilizing depending on the surface orientation with respect to gravity. In the wetting fronts, the momentum associated with the vapor effusion tends to push the interface away

Table 5.1 Statistically-determined interfacial characteristics of wavy vapor layer.

$U = 1.0$ m/s								
Orientation	Middle Section				Outlet Section			
θ	δ (mm)	λ (mm)	w (mm)	$b = w/\lambda$	δ (mm)	λ (mm)	w (mm)	$b = w/\lambda$
90°	1.95	15.13	3.48	0.23	2.26	18.77	4.10	0.22
135°	1.78	19.09	4.20	0.22	1.95	14.39	3.14	0.22
180°	1.54	10.33	2.39	0.23	1.82	17.25	3.79	0.22
225°	1.31	8.81	2.18	0.24	1.74	21.08	4.48	0.21
270°	1.27	6.03	1.34	0.22	1.93	15.26	3.21	0.21
$U = 1.5$ m/s								
Orientation	Middle Section				Outlet Section			
θ	δ (mm)	λ (mm)	w (mm)	$b = w/\lambda$	δ (mm)	λ (mm)	w (mm)	$b = w/\lambda$
0°	1.57	6.11	1.36	0.22	2.13	11.73	2.86	0.25
90°	1.72	11.28	2.45	0.21	2.01	16.03	3.32	0.21
135°	1.70	8.79	1.80	0.23	1.81	13.61	3.04	0.22
180°	1.53	10.41	2.33	0.22	1.79	20.07	4.50	0.22
225°	1.44	12.91	3.00	0.23	1.89	18.92	3.88	0.21
270°	1.39	6.32	1.39	0.22	1.79	12.76	2.96	0.23

from the heated wall. This momentum is resisted by a pressure force associated with interfacial curvature. When the vapor momentum at a wetting front overcomes the pressure force, the interface will be lifted from the wall and heat transfer at the wetting front is extinguished. Heat that would otherwise be dissipated at this extinguished wetting front will now have to be channeled to neighboring wetting fronts. Increased heat transfer in these neighboring wetting fronts greatly intensifies the vapor momentum perpendicular to the wall, creating conditions which are more favorable for lift-off at those wetting fronts as well. A chain reaction thus ensues, were wetting fronts are extinguished in succession, and the lift-off process actually accelerates with time as more heat has to be dissipated from a decreasing number of wetting fronts. This explains why flow boiling CHF is often described as a catastrophic rather than slow or gradual phenomenon.

In the present study, the Interfacial Lift-off model presented by Sturgis and Mudawar [25] is modified to incorporate the effects of body force as well as a new statistical interfacial curvature parameter. The reader should refer to ref. [25] for details of the Interfacial Lift-off model not included in this paper.

5.2.2 Interfacial Instability of Vapor Layer

Describing interfacial instability of the vapor layer requires knowledge of the mean liquid velocity, U_f, mean vapor velocity, U_g, and mean vapor layer thickness, δ. A two-phase separated flow model is employed to determine these parameters.

In this model, the heat supplied between the leading edge of the heated wall and a location z is assumed to bring a mass of liquid to saturation temperature and then convert the same mass to saturated vapor. Energy conservation leads to the following expression for vapor velocity, U_g,

$$U_g = \frac{q''z}{\rho_g \delta \left(c_{p,f} \Delta T_{sub,i} + h_{fg} \right)}. \tag{5.5}$$

The liquid velocity, U_f, can be determined from mass conservation by subtracting the rate of mass conversion to vapor from the total mass flow rate at the channel inlet.

$$U_f = \frac{UH}{H - \delta} - \frac{q''z}{\rho_f (H - \delta)\left(c_{p,f} \Delta T_{sub,i} + h_{fg} \right)}. \tag{5.6}$$

Conservation of momentum for a section Δz of the separated two-phase flow may be applied to control volumes encompassing the liquid (volume $A_f \Delta z$) and vapor (volume $A_g \Delta z$) separately, resulting, respectively, in the following equations.

$$\frac{d}{dz}\left(\rho_f U_f^2 A_f \right) + W'_{fg} u_i = -A_f \frac{dP}{dz} - \tau_{w,f} p_{w,f} + \tau_i p_i - \rho_f A_f g \sin\theta \tag{5.7}$$

and

$$\frac{d}{dz}\left(\rho_g U_g^2 A_g \right) - W'_{fg} u_i = -A_g \frac{dP}{dz} - \tau_{w,g} p_{w,g} - \tau_i p_i - \rho_g A_g g \sin\theta, \tag{5.8}$$

where W'_{fg} is the rate of evaporation per unit distance, u_i is the streamwise velocity of the vapor formed at the interface, $\tau_{w,f}$, $\tau_{w,g}$, and τ_i are, respectively, the wall shear stress in the liquid, wall shear stress in the vapor, and interfacial shear stress, and $p_{w,f}$, $p_{w,g}$ and p_i are the perimeter of liquid contact with the channel wall, perimeter of vapor contact with the channel wall, and perimeter of liquid-vapor contact (equal to channel width W), respectively.

The present model assumes that vapor generated at the wall has no initial streamwise velocity ($u_i \approx 0$) [21] and, as such, does not contribute streamwise momentum to the control volume. Introducing flow quality, x, and void fraction, α, into Eqs. (5.7) and (5.8) yields, respectively,

$$G^2 \frac{d}{dz}\left[\frac{(1-x)^2}{\rho_f(1-\alpha)}\right] = -(1-\alpha)\frac{dP}{dz} - \frac{\tau_{w,f}\,p_{w,f}}{A} + \frac{\tau_i\,p_i}{A} - \rho_f(1-\alpha)\,g\sin\theta \tag{5.9}$$

and

$$G^2 \frac{d}{dz}\left(\frac{x^2}{\rho_g\,\alpha}\right) = -\alpha\frac{dP}{dz} - \frac{\tau_{w,g}\,p_{w,g}}{A} - \frac{\tau_i\,p_i}{A} - \rho_g\,\alpha\,g\sin\theta, \tag{5.10}$$

where

$$x = \frac{\rho_g U_g \alpha}{G} \tag{5.11}$$

and $\alpha = \delta / H$.

Equation (5.10) can be rearranged to yield a pressure gradient for the vapor layer expressed as the sum of accelerational, frictional, and gravitational components.

$$\begin{aligned} -\frac{dP_g}{dz} &= \left(-\frac{dP_g}{dz}\right)_A + \left(-\frac{dP_g}{dz}\right)_F + \left(-\frac{dP_g}{dz}\right)_G \\ &= \frac{G^2}{\alpha}\frac{d}{dz}\left(\frac{x^2}{\alpha\rho_g}\right) + \frac{\tau_{w,g}}{\alpha}\left[\frac{1}{H} + \frac{2}{W}\alpha\right] + \frac{\tau_i}{\alpha}\frac{1}{H} + \rho_g g \sin\theta . \end{aligned} \tag{5.12}$$

Adding Eqs. (5.9) and (5.10) yields a pressure gradient for the combined flow (liquid and vapor) which can also be expressed as the sum of accelerational, frictional, and gravitational components.

$$-\frac{dP}{dz}=\left(-\frac{dP}{dz}\right)_A+\left(-\frac{dP}{dz}\right)_F+\left(-\frac{dP}{dz}\right)_G$$

$$=G^2\frac{d}{dz}\left(\frac{x^2}{\alpha\rho_g}+\frac{(1-x)^2}{(1-\alpha)\rho_f}\right)+\tau_{w,g}\left[\frac{1}{H}+\frac{2}{W}\alpha\right]+\tau_{w,f}\left[\frac{1}{H}+\frac{2}{W}(1-\alpha)\right]+\left[\alpha\rho_g+(1-\alpha)\rho_f\right]g sin\theta. \tag{5.13}$$

The wall shear stress terms in Eqs. (5.12) and (5.13) can be expressed in terms of a friction factor,

$$\tau_{w,k}=\frac{1}{2}\rho_k U_k^2\left(\frac{f_k}{4}\right), \tag{5.14}$$

where k indicates the phase, and the friction factor is given by [25]

$$f_k=0.184\left(\frac{\rho_k U_k D_{h,k}}{\mu_k}\right)^{-1/5}, \tag{5.15}$$

and $D_{h,k}$ is the hydraulic diameter for each phase. The interfacial shear stress term in Eq. (5.12) is defined as

$$\tau_i=\frac{C_{f,i}}{2}\rho_g\left(U_g-U_f\right)^2. \tag{5.16}$$

Galloway and Mudawar [21] examined several models for the interfacial friction coefficient, $C_{f,i}$, and recommended a constant value of 0.5 for a wavy vapor-liquid interface.

Equating the pressure gradients in Eqs. (5.12) and (5.13) yields an equation which can be solved along with Eqs. (5.5) and (5.6) to determine the variations of U_f, U_g and δ with z.

The observed liquid-vapor interface can be idealized as a sinusoidal wave of the form

$$\eta(z,t) = \eta_0 e^{ik(z-ct)} \, , \tag{5.17}$$

where η_0 represents the wave amplitude ($\eta_0 = \delta$), k the wave number ($k = 2\pi/\lambda$), and c the wave speed. Using classical instability theories [21,25,32], the pressure difference resulting from a small disturbance perpendicular to the interface can be expressed as

$$P_f - P_g = -\left[\rho_f''\left(c - U_f\right)^2 + \rho_g''\left(c - U_g\right)^2 + \left(\rho_f - \rho_g\right)\frac{g_n}{k}\right] k\,\eta_0\, e^{ik(z-ct)} \, , \tag{5.18}$$

where $\rho_f'' = \rho_f \coth\left(kH_f\right)$ and $\rho_g'' = \rho_g \coth\left(kH_g\right)$ ("modified density" terms), and g_n is the component of gravity perpendicular to the heated wall. The pressure difference can be related to the surface tension force by

$$P_f - P_g \approx \sigma \frac{\partial^2 \eta}{\partial z^2} = -\sigma \eta_0 k^2 e^{ik(z-ct)}. \tag{5.19}$$

Equating pressure difference in Eqs. (5.18) and (5.19) yields an expression for the wave speed, c.

$$c = \frac{\rho_f'' U_f + \rho_g'' U_g}{\rho_f'' + \rho_g''} \pm \sqrt{\frac{\sigma k}{\rho_f'' + \rho_g''} - \frac{\rho_f'' \rho_g'' \left(U_g - U_f\right)^2}{\left(\rho_f'' + \rho_g''\right)^2} - \frac{\left(\rho_f - \rho_g\right)}{\left(\rho_f'' + \rho_g''\right)} \frac{g \cos\theta}{k}} \, . \tag{5.20}$$

A negative argument in the radical of Eq. (5.20) results in a wave speed containing both real and imaginary components. The imaginary component

$$c_i = \sqrt{\frac{\rho_f'' \rho_g'' \left(U_g - U_f\right)^2}{\left(\rho_f'' + \rho_g''\right)^2} + \frac{\left(\rho_f - \rho_g\right)}{\left(\rho_f'' + \rho_g''\right)} \frac{g \cos\theta}{k} - \frac{\sigma k}{\rho_f'' + \rho_g''}} \tag{5.21}$$

represents the combined effect of the different forces and determines the stability of the interface. The first term under the radical in Eq. (5.21) is a measure of the destabilizing effect of velocity difference between the liquid and vapor phases. The second term is the body force effect, which may be stabilizing or destabilizing depending on orientation of the wall relative to gravity. The third term accounts for surface tension which is always stabilizing to the interface.

The critical wavelength, defined as the wavelength of a neutrally stable wave, can be determined by setting the radical in Eq. (5.21) equal to zero.

$$k_c = \frac{2\pi}{\lambda_c} = \frac{\rho_f'' \rho_g'' \left(U_g - U_f\right)^2}{2\sigma\left(\rho_f'' + \rho_g''\right)} + \sqrt{\left[\frac{\rho_f'' \rho_g'' \left(U_g - U_f\right)^2}{2\sigma\left(\rho_f'' + \rho_g''\right)}\right]^2 + \frac{\left(\rho_f - \rho_g\right) g \cos\theta}{\sigma}} . \quad (5.22)$$

Figure 5.5 shows the dependence of critical wavelength, λ_c, on the velocity difference and flow orientation. Different values of velocity difference are assumed to explore the λ_c trends. For low velocities, there exists an orientation range over which the interface is always stable. This should produce a fairly smooth vapor layer along the heated wall and preclude any liquid contact, greatly reducing CHF for these orientations and low velocity differences. This was indeed observed by the authors in [26]. Interestingly, even with an unstable wave that provides the necessary liquid contact in wetting fronts, Fig. 5.5 shows low velocity differences both exhibit high sensitivity to orientation and produce unusually large wavelengths. At 0.1 m/s, the critical wavelength engulfs a large fraction of the heated length, meaning very low velocity differences can cause dryout of a considerable fraction of the heated area and induce CHF prematurely. These large wavelengths are also consistent with the observations of the authors in [26]. Finally, Fig. 5.5 shows increasing velocity reduces the sensitivity of λ_c to body force by imparting dominance to the inertia term in Eq. (5.21) compared to the body force term. For high velocities, Eq. (5.22) shows λ_c will approach the limit

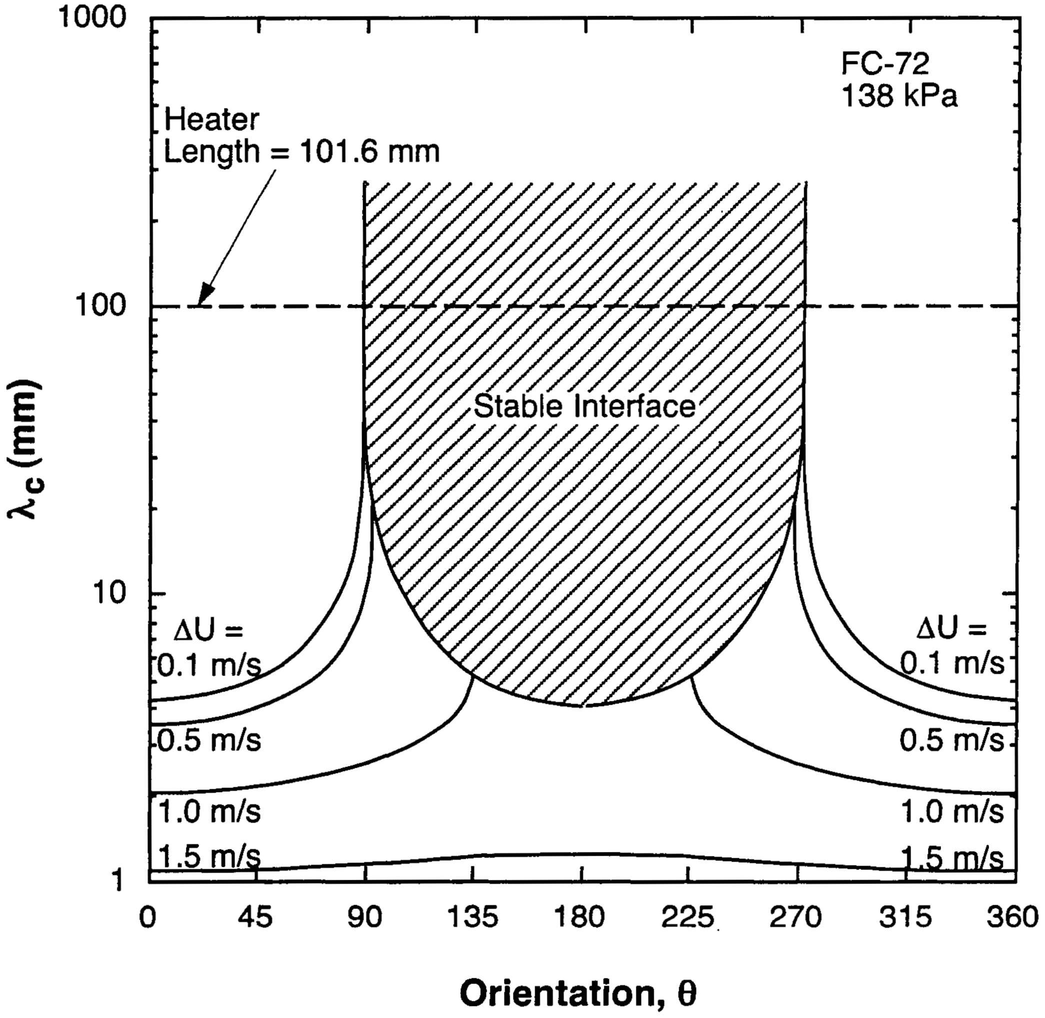

Fig. 5.5 Variation of predicted critical wavelength with flow orientation for different phase velocity differences.

$$\lambda_c = \frac{2\pi\sigma\left(\rho''_f + \rho''_g\right)}{\rho''_f \rho''_g \left(U_g - U_f\right)^2} \; . \tag{5.23}$$

irrespective of body force.

5.2.3 Interfacial Lift-off

As indicated earlier, interfacial lift-off is postulated to occur when the momentum flux of vapor emanating from the wetting front just exceeds the pressure force acting upon the interface. The pressure force is the result of the difference between liquid and vapor pressures across the curved interface. Figure 5.6 illustrates these two opposing effects.

The pressure force over the entire wetting front is obtained by integrating Eq. (5.18) over the length $b\lambda$ centered at the wetting front.

$$\overline{P_f - P_g} = \frac{4\pi\sigma\delta}{b\lambda^2}\sin\left(b\pi\right). \tag{5.24}$$

The heat supplied in the wetting front is consumed by vaporizing liquid into vapor according the relation

$$q''_w A_w = \left(c_{p,f}\Delta T_{sub,i} + h_{fg}\right)\rho_g U_{g,n} A_w \, , \tag{5.25}$$

where $U_{g,n}$ is the vapor velocity in the wetting front normal to the wall. Equation (5.25) yields

$$U_{g,n} = \frac{q''_w}{\rho_g\left(c_{p,f}\Delta T_{sub,i} + h_{fg}\right)} . \tag{5.26}$$

The local lift-off heat flux can be determined by equating the vapor momentum, $\rho_g U^2_{g,n}$, to the pressure force.

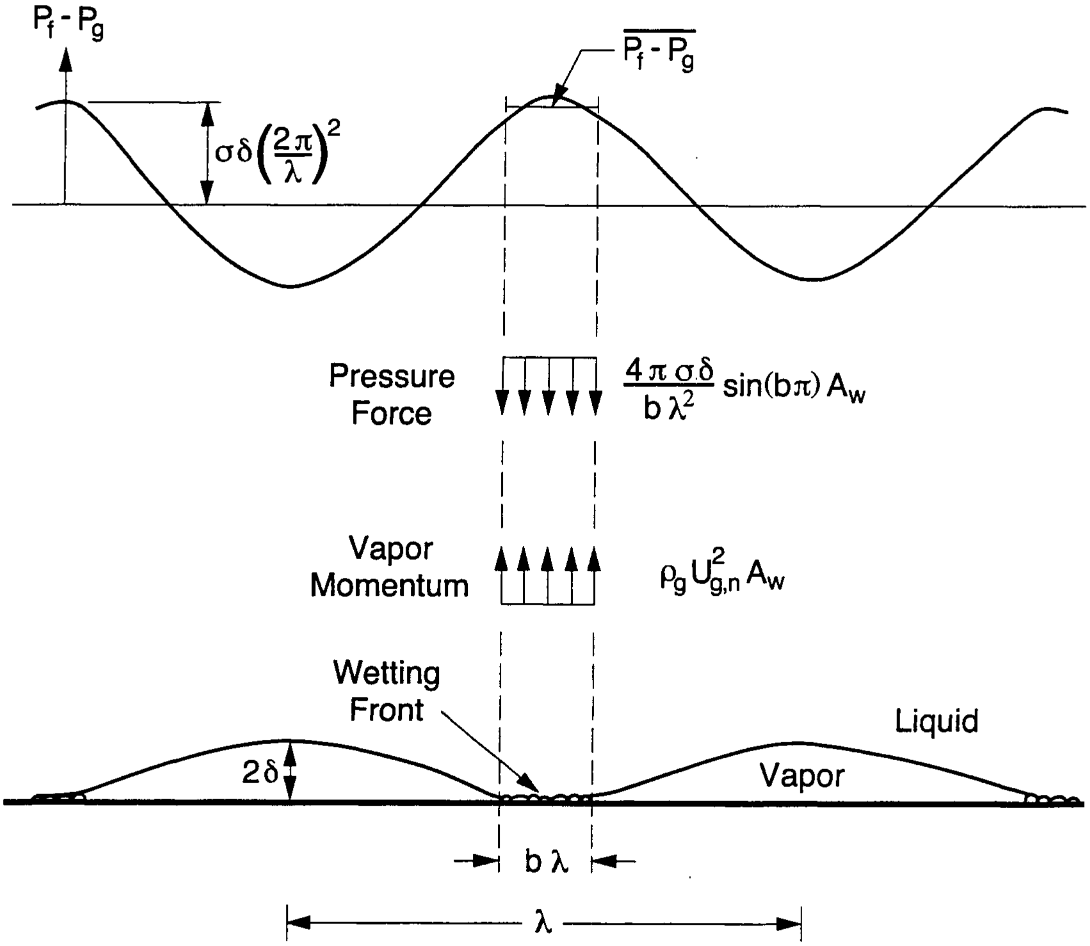

Fig. 5.6 Balance of vapor momentum and interfacial pressure difference used to determine lift-off heat flux.

$$q_w'' = \rho_g\left(c_{p,f}\Delta T_{sub,i} + h_{fg}\right)\sqrt{\frac{P_f - P_g}{\rho_g}} = \rho_g\left(c_{p,f}\Delta T_{sub,i} + h_{fg}\right)\left[\frac{4\pi\sigma}{\rho_g}\frac{\sin(b\pi)}{b}\right]^{1/2}\frac{\delta^{1/2}}{\lambda}. \tag{5.27}$$

Equation (5.27) shows the lift-off heat flux, q_w'', is proportional to $\delta^{1/2}/\lambda$, which can be viewed as a measure of interfacial curvature.

Flow visualization revealed the existence of a continuous wetting region near the leading edge, where the liquid maintains contact with the heated wall. The length of the upstream continuous wetting region, z^*, may be defined as

$$z^* = z_0 + \lambda_c(z^*), \tag{5.28}$$

where z_0 is the location measured from the leading edge where the vapor velocity just surpasses the liquid velocity [25]. Hydrodynamic instability generates the wavy interface at z^*, downstream from which the wavy vapor layer begins to propagate along the heated wall.

The flow visualization measurements revealed the interfacial wavelengths increase is the flow direction, as shown in Figs. 5.7 and 5.8 for U = 1.0 and 1.5 m/s, respectively. Wavelengths in the middle and outlet sections of the heater grow to over four times their critical value at z^*.

The wave curvature parameter $\delta^{1/2}/\lambda$ was also calculated from the flow visualization measurements in the middle and outlet sections of the heated length for U = 1.0 and 1.5 m/s; the results are shown in Figs. 5.9 and 5.10, respectively. Several

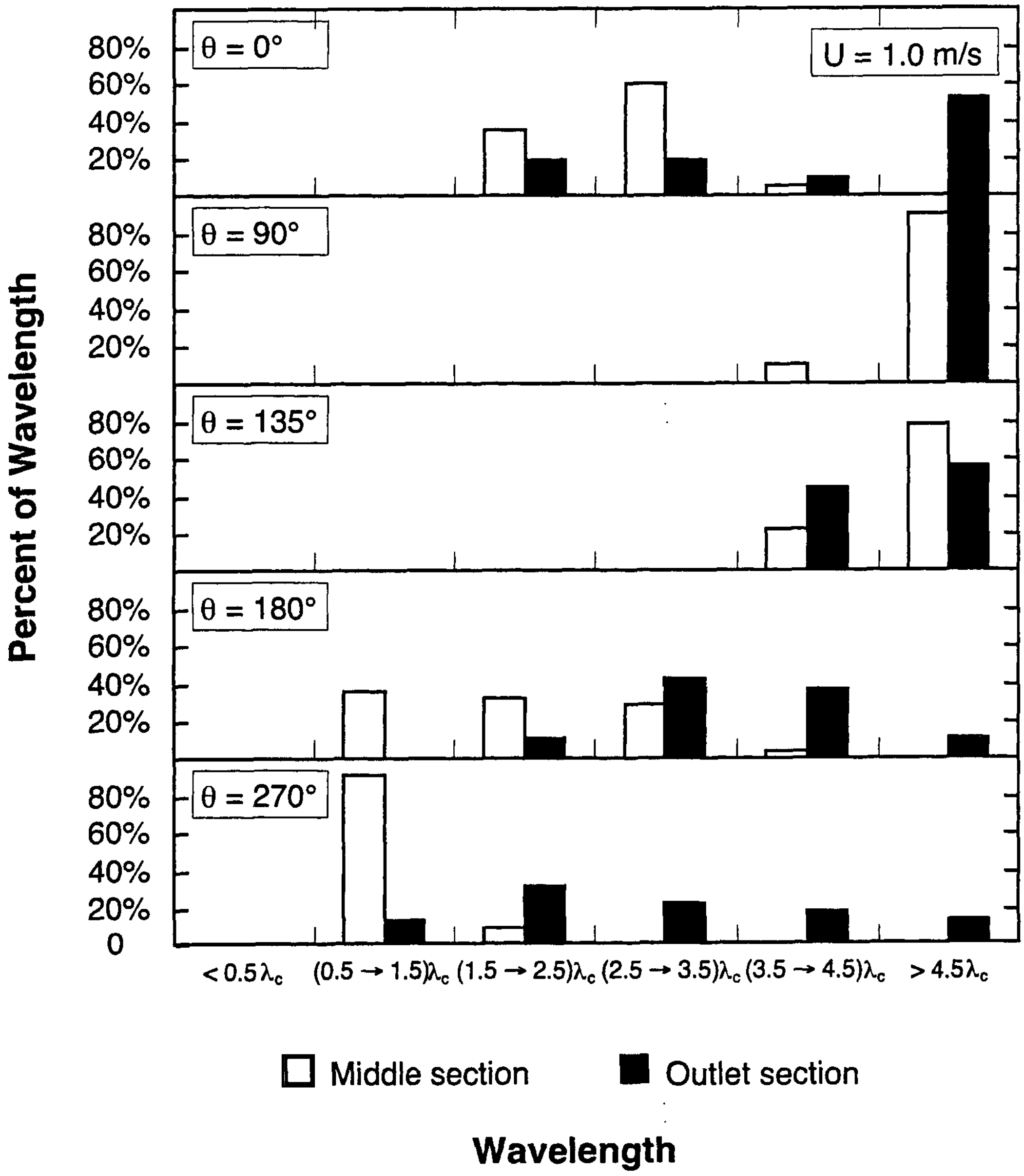

Fig. 5.7 Distribution of wavelengths measured in middle and outlet sections of heated wall relative to critical wavelength predicted at z* for U = 1.0 m/s.

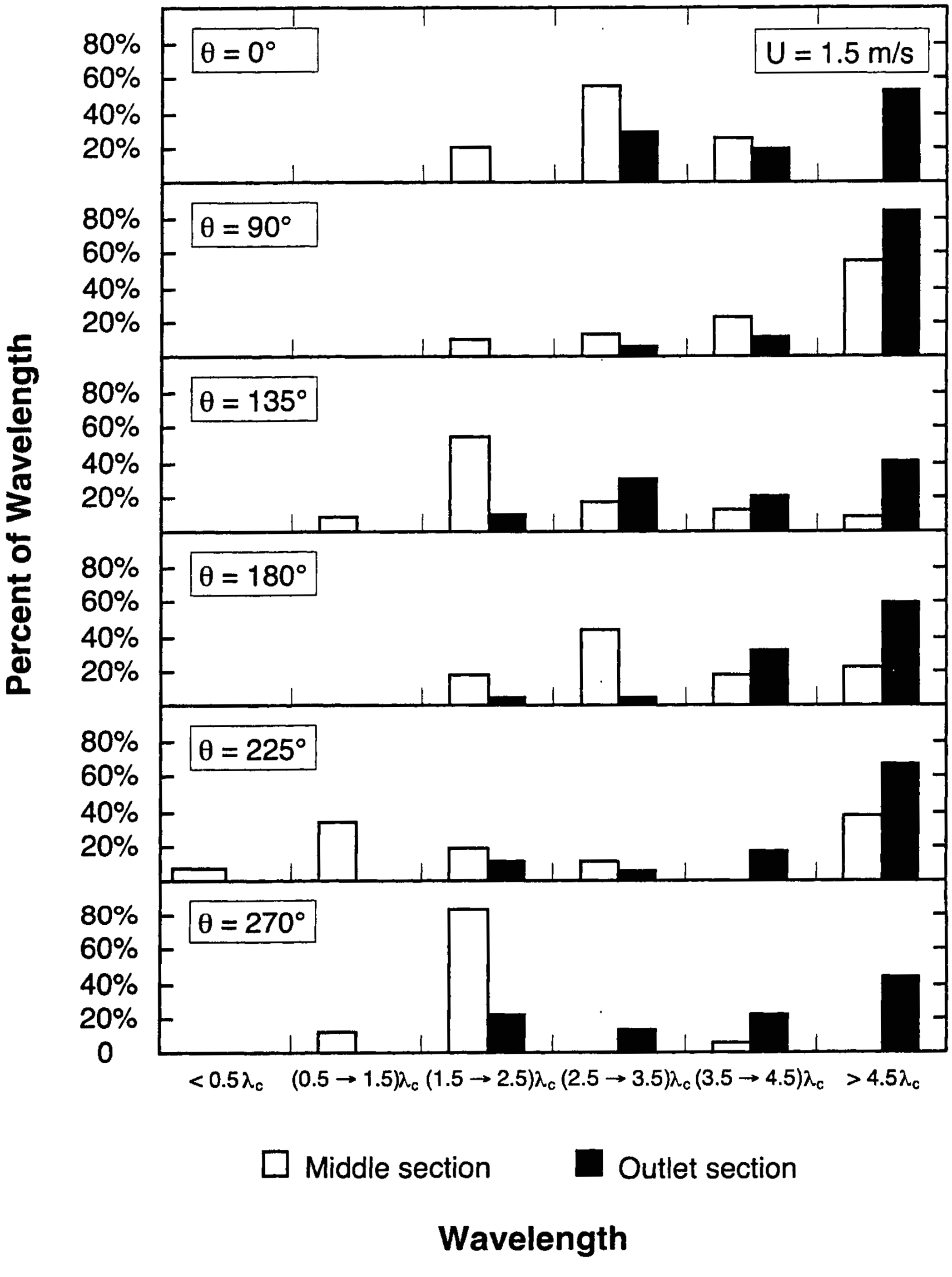

Fig. 5.8 Distribution of wavelengths measured in middle and outlet sections of heated wall relative to critical wavelength predicted at z* for U = 1.5 m/s.

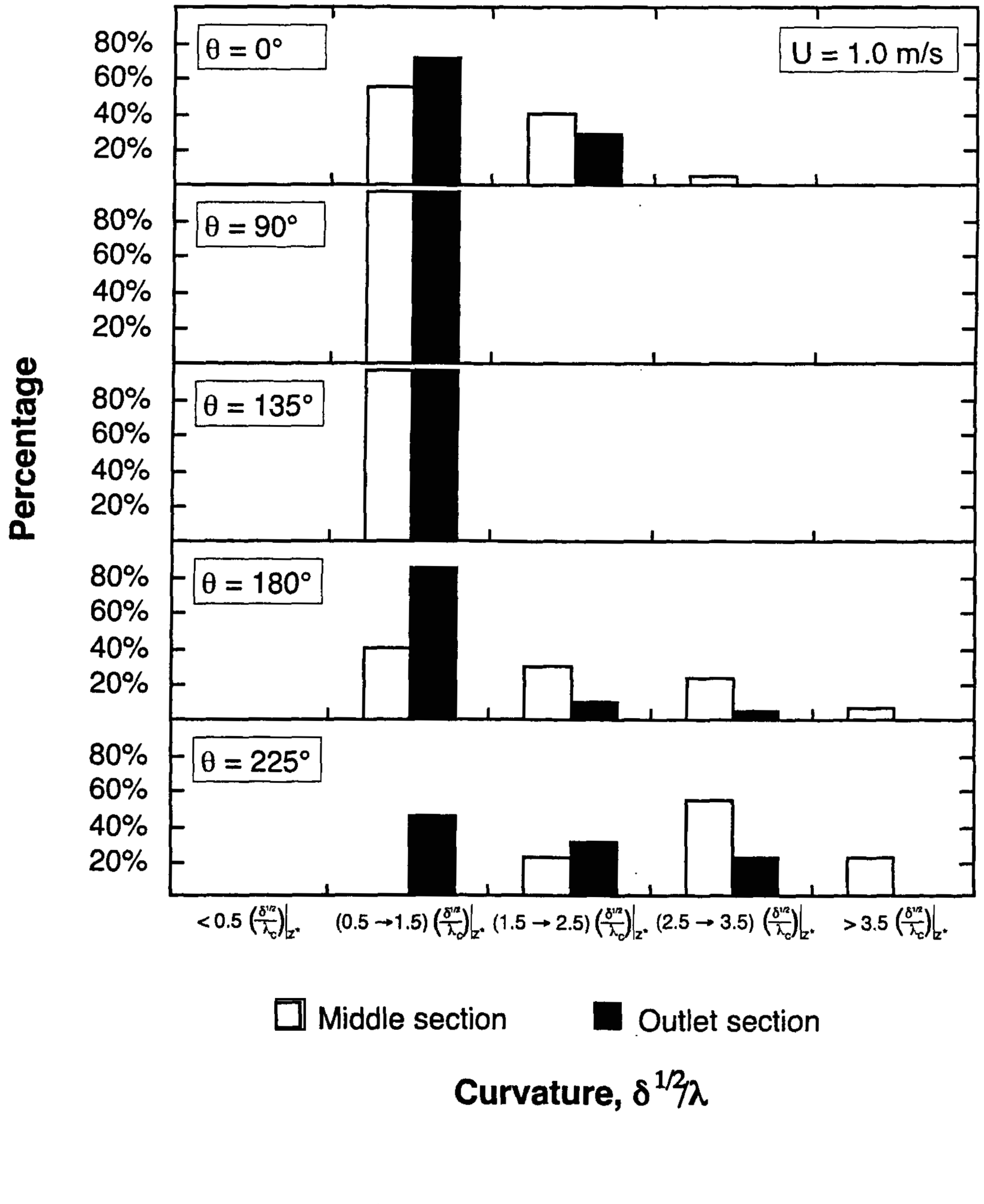

Fig. 5.9 Distribution of wave curvature parameter in middle and outlet sections compared with its value at z* for U = 1.0 m/s.

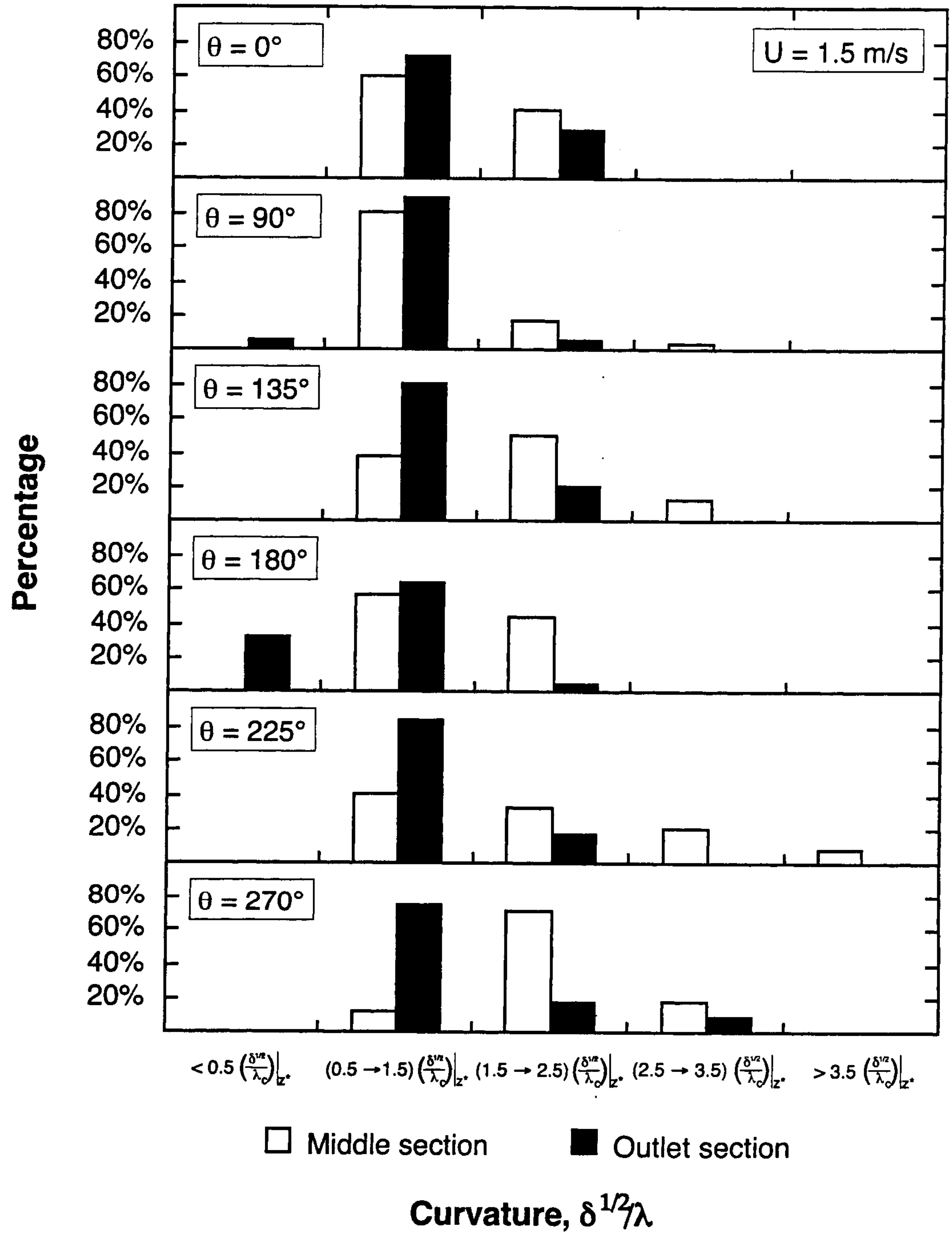

Fig. 5.10 Distribution of wave curvature parameter in middle and outlet sections compared with its value at z* for U = 1.5 m/s.

important conclusions can be drawn from these plots. First, the waves in the outlet section are slightly flatter (i.e., characterized by weaker curvature) that those in the middle section since the outlet section's $\delta^{1/2}/\lambda$ values are somewhat smaller. The outlet waves are therefore easier to lift off from the heated wall. Thus, CHF is more likely to occur in the outlet section. This was confirmed in the present study by consistent CHF detection by the outlet thermocouple array first for CHF conditions belonging to the wavy vapor layer regime. Overall, however, Figs. 5.9 and 5.10 show the majority of $\delta^{1/2}/\lambda$ values for both the middle and outlet sections range from $0.5(\delta^{1/2}/\lambda_c)$ to $1.5(\delta^{1/2}/\lambda_c)$, where both δ and λ_c are calculated at z^*. Therefore, these waves, which are generated upstream at z^*, have a tendency to preserve their curvature value as they propagate along the heated wall.

Measurements also reveal that the wetting front length increases in the flow direction while remaining a constant fraction of the local wavelength,

$$w_j = b\lambda_j . \tag{5.29}$$

For the present model, b = 0.20 is used based on both the present flow visualization measurements and for consistency with Sturgis and Mudawar statistical results [25].

Prior to CHF, liquid makes contact with the heated wall only in the wetting fronts. With the definition of critical heat flux, q_m'', as the average heat flux over the entire heated wall, an energy balance for the outlet section gives

$$q_m'' = b q_w'' . \tag{5.30}$$

Combining Eqs. (5.27) and (5.30) gives

$$q''_m = \rho_g \left(c_{p,f}\,\Delta T_{sub,i} + h_{fg} \right) \left[\frac{4\pi\sigma b\, sin(b\pi)}{\rho_g} \right]^{1/2} \left. \frac{\delta^{1/2}}{\lambda_c} \right|_{z*}, \qquad (5.31)$$

where both δ and λ_c are calculated at $z*$ since $\delta^{1/2}/\lambda$ in the outer section and at $z*$ are equal.

5.3 Model Predictions

An iterative numerical technique is used to calculate CHF. First, an estimated value for CHF is used in the separated flow model to determine the variations of phase velocities, U_f and U_g, and vapor layer thickness, δ, with z. The output of the separated flow model is then utilized in the instability analysis to determine $z*$ and the critical wavelength, λ_c, at $z*$. Equation (5.31) was then used to calculate a new CHF value. This value is input into the separated flow model in the next iteration. The solution is deemed convergent once the CHF values of consecutive iterations are matched.

The model was applied to near-saturated conditions corresponding to the entire wavy vapor layer regime. The predicted and measured CHF values are compared in Figs. 5.11-5.13 for three velocities. The predictions capture the overall shape of CHF variation with orientation angle quite well, with predictions falling mostly within a ± 30% error band. The mean absolute error of the model predictions from the data is 20.0, 9.8 and 5.4% for $U = 0.5$, 1.0 and 1.5 m/s, respectively.

Figure 5.11 shows a specific range of downflow orientations for which the CHF model will not converge for U = 0.5 m/s. Figure 5.5 shows this orientation range may yield a stable interface, and, according to Fig. 1.4, fall into stratification or separated

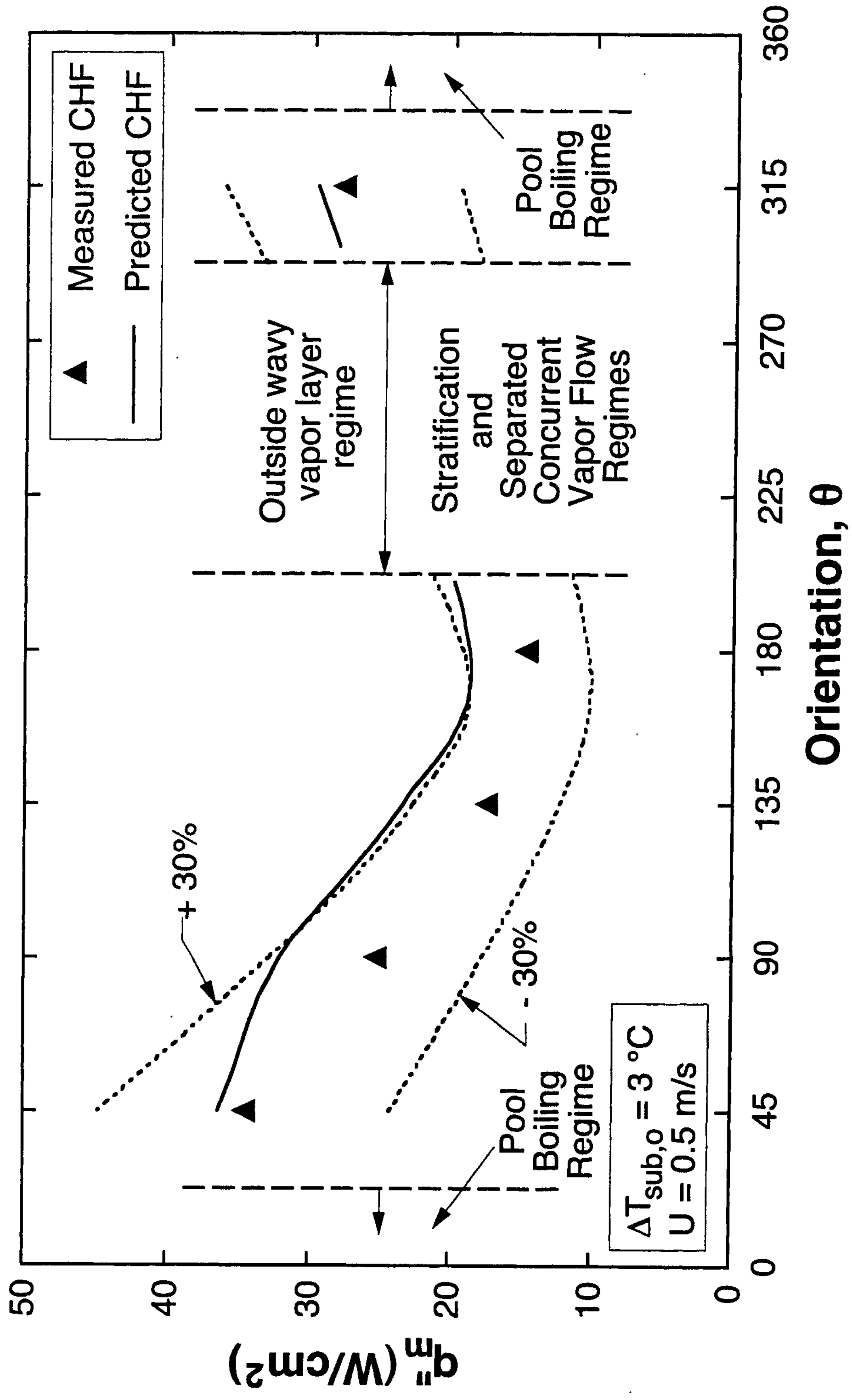

Fig. 5.11 Comparision of measured and predicted CHF for U = 0.5 m/s.

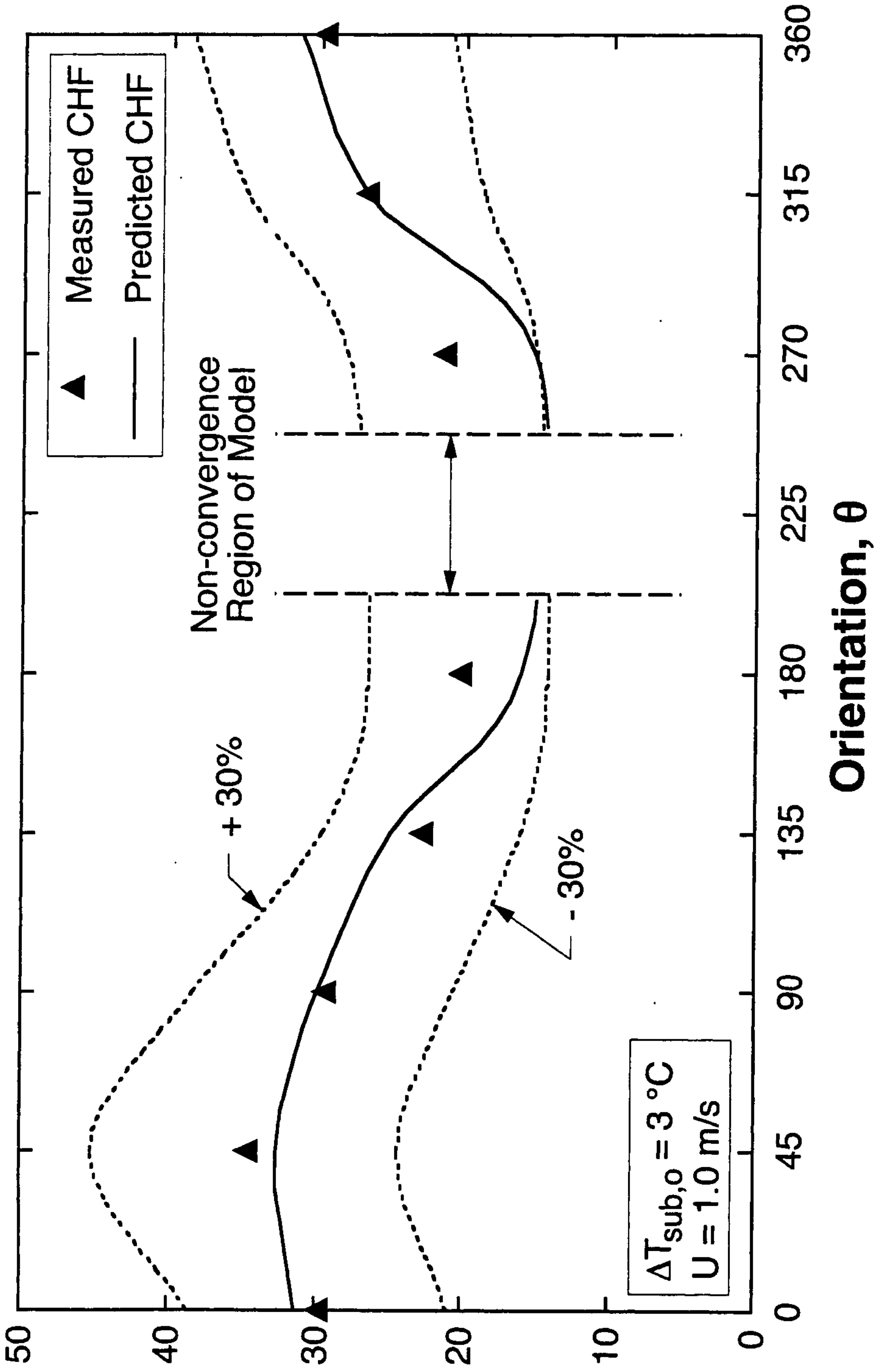

Fig. 5.12 Comparision of measured and predicted CHF for U = 1.0 m/s.

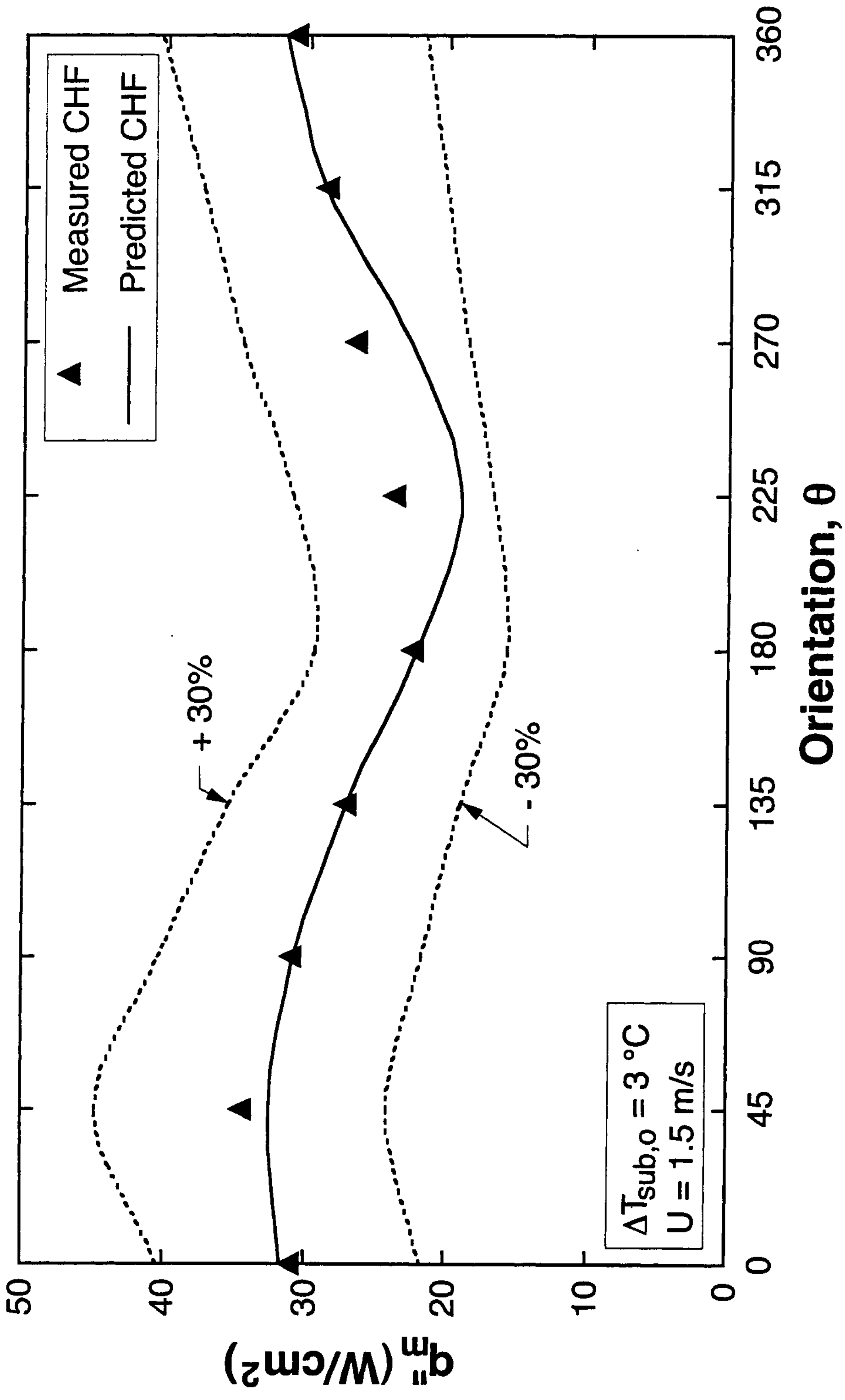

Fig. 5.13 Comparision of measured and predicted CHF for U = 1.5 m/s.

concurrent vapor flow regimes. Figure 5.12 shows similar limitations of the present model near $\theta = 225°$ for $U = 1.0$ m/s.

CHAPTER 6

METHODOLOGY FOR OVERCOMING BODY FORCE ON FLOW BOILING CHF

6.1 Effects of Body Force on CHF

Since the Wavy Vapor Layer Regime was observed for a large fraction of the present operating conditions, it is prudent to explore the dependence of interfacial instability on the forces which influence vapor behavior at different velocities and orientations. The speed of an idealized sinusoidal liquid-vapor interface between a vapor layer moving at velocity U_g and a liquid layer at U_f can be expressed as [21]

$$c=\frac{\rho_f U_f+\rho_g U_g}{\rho_f+\rho_g}\pm\sqrt{\frac{\sigma k}{\rho_f+\rho_g}-\frac{\rho_f\rho_g\left(U_g-U_f\right)^2}{\left(\rho_f+\rho_g\right)^2}-\frac{\left(\rho_f-\rho_g\right)}{\left(\rho_f+\rho_g\right)}\frac{g_e\cos\theta}{k}}\,, \tag{6.1}$$

where k is the wave number. A negative argument in the radical of Eq. (6.1) results in a wave speed containing both real and imaginary components. The imaginary component

$$c_i=\sqrt{\frac{\rho_f\rho_g\left(U_g-U_f\right)^2}{\left(\rho_f+\rho_g\right)^2}+\frac{\left(\rho_f-\rho_g\right)}{\left(\rho_f+\rho_g\right)}\frac{g_e\cos\theta}{k}-\frac{\sigma k}{\rho_f+\rho_g}} \tag{6.2}$$

represents the combined effect of the different forces and dictates the stability (or instability) of the interface. The first term under the radical in Eq. (6.2) is a measure of the destabilizing effect of inertia, or velocity difference between the vapor and liquid phases. The second term is the body force effect, which, for a terrestrial environment, may be stabilizing or destabilizing depending on orientation of the wall relative to gravity. The third term accounts for surface tension which is always stabilizing to the interface.

The critical wavelength, defined as the wavelength of a neutrally stable wave, can be determined by setting the radical in Eq. (6.2) equal to zero.

$$\frac{2\pi}{\lambda_c} = \frac{\rho_f \rho_g (U_g - U_f)^2}{2\sigma(\rho_f + \rho_g)} + \sqrt{\left[\frac{\rho_f \rho_g (U_g - U_f)^2}{2\sigma(\rho_f + \rho_g)}\right]^2 + \frac{(\rho_f - \rho_g) g_e \cos\theta}{\sigma}} . \tag{6.3}$$

Figure 5.5 shows the variation of λ_c with orientation for different assumed values of velocity difference between the two phases. For low velocity differences, the interface is stable over a broad range of orientations, over which the Wavy Vapor Layer Regime cannot be maintained. Such a stable interface would preclude liquid contact with the wall, greatly reducing CHF for these orientations and low velocity differences. Figure 5.5 shows even for upflow orientations, a velocity difference of $\Delta U = 0.1$ m/s will produce a critical wavelength approaching the length of the entire heated wall. The interface becomes increasing unstable and less sensitive to orientation with increasing velocity difference. For high velocity differences, Eq. (6.1) shows λ_c will approach the limit

$$\lambda_c = \frac{2\pi\sigma(\rho_f + \rho_g)}{\rho_f \rho_g (U_g - U_f)^2} \tag{6.4}$$

regardless of orientation. Another interesting feature of Fig. 5.5 is that it shows a strong correlation between the orientation range associated with a stable interface and low CHF values in Fig. 3.10 associated with low velocities.

Figure 6.1 shows CHF data for the limiting velocities of 0.1 and 1.5 m/s versus orientation angle. Also shown are predictions based on previous semi-empirical and theoretical CHF models. The Interfacial Lift-off Model, first proposed by Galloway and Mudawar [20,21] in the early 1990s, is intended for the dominant Wavy Vapor Layer Regime depicted in Figs. 3.1(b) and 3.2. This model is based on the assumption that the wavy layer makes contact with the heated wall over relatively short discrete regions corresponding to the wave troughs. It postulates that CHF will occur when the intense momentum of vapor generated normal to the wall exceeds the pressure force resulting from the interfacial curvature. Recently, the authors of the present study modified this model to explore the effects of orientation and interfacial wave growth [27]. Their model predictions show good agreement with the 1.5 m/s data as shown in Fig. 6.1. Convergence was never achieved with this model for $U = 0.1$ m/s because of the large critical wavelength as discussed earlier in relation to Fig. 5.5. Data for this lower velocity are compared to predictions of the classical CHF model of Zuber et al. [29] for pool boiling from a horizontal upward-facing heated wall. The gravitational acceleration, g_e, in the original model was replaced by $g_e \cos\theta$ since the Taylor instability employed in the model is based on only the component of gravity perpendicular to the heated wall.

$$q''_m = 0.131\,\rho_g\,h_{fg}\left[\frac{\sigma\left(\rho_f-\rho_g\right)g_e\cos\theta}{\rho_g^2}\right]^{1/4} . \tag{6.5}$$

Figure 6.1 shows the pool boiling CHF model underpredicts CHF data corresponding to the present Pool Boiling Regime because it does not incorporate the benefits of liquid motion and its contribution to vapor removal along the channel.

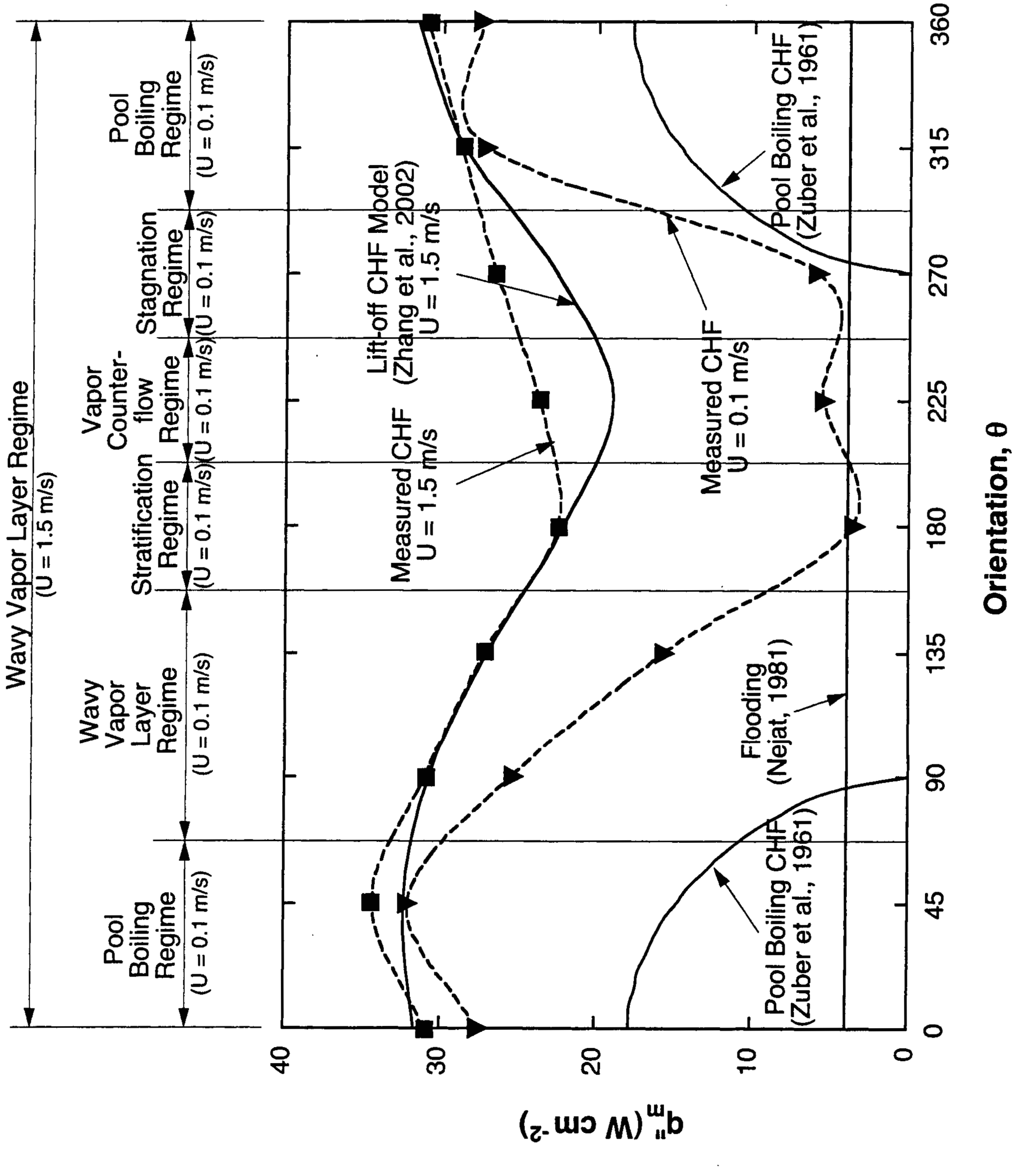

Fig. 6.1 Comparison of CHF data for lowest and highest velocities with predictions based on previous models and correlations.

Also shown in Fig. 6.1 are CHF predictions based on Negat's [33] flooding criterion

$$q''_m = 0.36\left(\frac{L}{D_h}\right)^{0.1}\left(\frac{A}{A_w}\right)\rho_g h_{fg}\left[\frac{(\rho_f-\rho_g)g_e D_h}{\rho_g}\right]^{1/2}\left[1+\left(\frac{\rho_g}{\rho_f}\right)^{1/4}\right]^{-2}, \quad (6.6)$$

which was derived for a closed-end vertical heated tube, where L, D_h, A, and A_w are the heated length, hydraulic diameter, heated area, and channel cross-sectional area, respectively. Figure 6.1 shows all 0.1 m/s CHF data belonging to the Stratification, Vapor Counterflow, and Stagnation Regimes approach the flooding limit. This limit occurs when vapor upflow in a pipe with a closed bottom prevents liquid from flowing downwards to replenish liquid that has been evaporated. This situation resembles the vapor behavior observed in this study in conjunction with the Vapor Counterflow and Stagnation Regimes, but not the Stratification Regime.

Figure 6.1 proves the Interfacial Lift-off Model is an effective tool for predicting high velocity flow boiling CHF for all orientations, while the flooding limit is useful for estimating CHF at low velocities and downflow orientations. However, a more systematic and comprehensive methodology is needed to design thermal management systems that can overcome the effects of body force on flow boiling CHF for different fluids and gravitational fields. Aside for terrestrial applications, such a tool is highly desired for design of thermal management hardware in space applications.

Flow orientation is sometimes dictated by system considerations other than heat dissipation. As indicated before, body force influences flow boiling CHF in three ways:

(1) The body force component that is perpendicular to the heated wall influences hydrodynamic instability of the vapor-liquid interface.

(2) The body force component in the direction of (or opposite to) the liquid flow influences vapor removal from the channel and may trigger flooding at low velocities.

(3) A very long critical wavelength may preclude liquid contact with a large fraction of the heated wall.

Therefore, three separate criteria must be developed to overcome the effects of body force on flow boiling CHF.

6.2 Effects of Component of Body Force Perpendicular to Heated Wall

Equation (6.2) reveals interfacial instability of a vapor-liquid interface in a flow channel is governed by the combined effect of inertia, surface tension, and component of body force that is perpendicular to the heated wall. Equation (6.3) can be rearranged in the following form

$$\frac{2\pi}{\lambda_c}\frac{\sigma\left(\rho_f+\rho_g\right)}{\rho_f\rho_g\left(U_g-U_f\right)^2}=\frac{1}{2}\left\{1+\sqrt{1+4\frac{\left(\rho_f-\rho_g\right)\left(\rho_f+\rho_g\right)^2\sigma g_e\cos\theta}{\rho_f{}^2\rho_g{}^2\left(U_g-U_f\right)^4}}\right\}, \qquad (6.7)$$

The right-hand-side of Eq. (6.7) approaches unity when the component of body force perpendicular to the heated wall is too weak to influence interfacial instability. This constitutes a sufficient condition for negating the influence of this component of body force on CHF and which corresponds to flows that fall into the Wavy Vapor Layer Regime. This condition can be expressed as

$$\left|\frac{\left(\rho_f-\rho_g\right)\left(\rho_f+\rho_g\right)^2\sigma g_e\cos\theta}{\rho_f^2\rho_g^2(U_g-U_f)^4}\right|<<\frac{1}{4}. \qquad (6.8)$$

This criterion was examined by substituting the phase velocity difference by the characteristic velocity of the flow channel, namely U. The left-hand-side of Eq. (6.8) can also be expressed as Bo/We^2, where Bo and We are the Bond and Weber numbers, respectively, which are defined as

$$We = \frac{\rho_f \rho_g U^2 L}{(\rho_f + \rho_g)\sigma} \tag{6.9}$$

and

$$Bo = \frac{(\rho_f - \rho_g) g_e \cos\theta L^2}{\sigma}. \tag{6.10}$$

Figures 6.2(a) and 6.2(b) show the variation of Bo/We^2 with orientation and flow velocity. The peak values of Bo/We^2 for $U = 0.1$, 0.2, 0.5, 1.0 and 1.5 m/s are 4503, 281, 7.2, 0.45, and 0.09, respectively. The large values corresponding to $U = 0.1$ and 0.2 m/s are consistent with the strong influence of orientation on CHF for these velocities. Conversely, the small values of Bo/We^2 for $U = 1.0$ and 1.5 m/s are indicative of a very weak influence of body force on CHF for these velocities, as was clearly demonstrated in the flow boiling experiments. Since the CHF data showed little dependence on orientation for $U \sim 1.5$ m/s, the magnitude of Bo/We^2 for $U = 1.5$ m/s is used as a criterion for overcoming body force effects on CHF.

$$\frac{Bo}{We^2} = \frac{(\rho_f - \rho_g)(\rho_f + \rho_g)^2 \sigma g_e}{\rho_f^2 \rho_g^2 U^4} \le 0.09. \tag{6.11}$$

6.3 Effects of Component of Body Force Parallel to Heated Wall

Several complex CHF regimes were identified in the present study for predominantly downflow orientations at low velocities. The Vapor Counterflow and Vapor Stagnation CHF regimes were both the result of the relative velocity between the

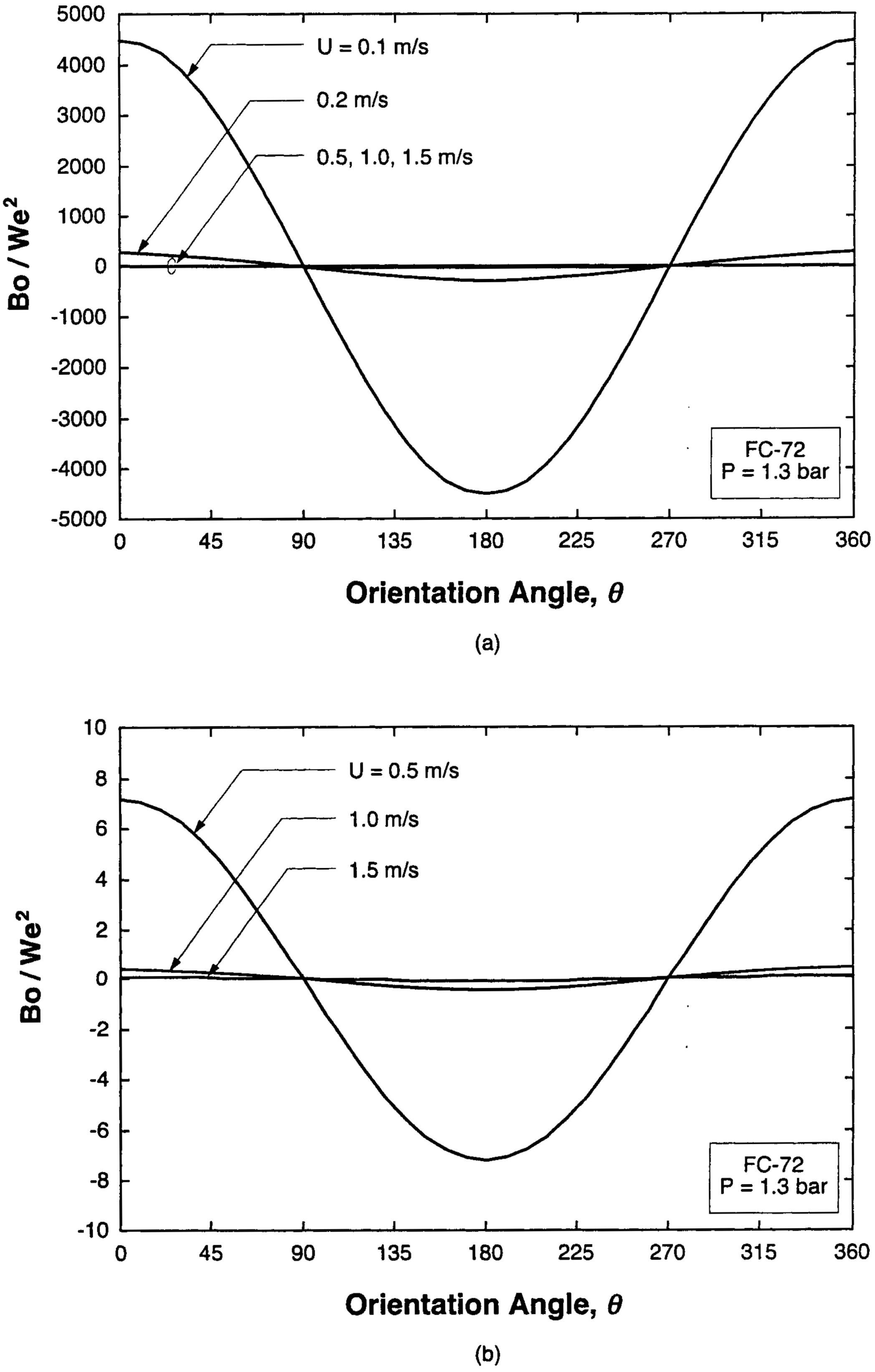

Fig. 6.2 Variation of Bo/We^2 with flow orientation and velocity for (a) all velocities tested and (b) U ≥ 0.5 m/s.

vapor and liquid phases, while the Separated Concurrent Vapor Flow was a transitional regime between the Vapor Stagnation and Wavy Vapor Layer CHF regimes. In the Vapor Stagnation and Vapor Counterflow Regimes, the vapor took the form of a long slug bubble as shown in Fig. 3.6. The rise velocity of a slug bubble relative to liquid can be expressed as [34]

$$U_\infty = 0.35\,\frac{\left[\left(\rho_f - \rho_g\right) g_e \sin\theta\, D_h\right]^{1/2}}{\rho_f^{1/2}}. \tag{6.12}$$

When U_∞ exceeds the liquid velocity, U, the vapor tends to flow backwards relative to the liquid. Vapor Stagnation occurs when the two velocities are equal. A sufficient condition for negating vapor counterflow and vapor stagnation is $U_\infty << U$, which, for $\sin\theta = 1$, can be represented in terms of the Froude number,

$$\frac{1}{Fr} = \left|\frac{\left(\rho_f - \rho_g\right) g_e \sin\theta\, D_h}{\rho_f U^2}\right| << 8.16. \tag{6.13}$$

Figures 6.3(a) and 6.3(b) show the variation of *1/Fr* for different orientations and flow velocities. For $U = 0.1$ and 0.2 m/s and $\theta = 225$ and 270°, where vapor counterflow and vapor stagnation were observed, Fig. 6.3(a) shows the magnitude of *1/Fr* is larger than 0.82. Conversely, Fig. 6.3(b) shows the magnitude of *1/Fr* for the other higher velocities is less than 0.13. Since vapor counterflow and vapor stagnation where not observed for $U = 0.5$ m/s, a sufficient criterion for precluding the occurrence of these flow anomalies can be expressed for $\sin\theta = 1$ by the criterion

$$\frac{1}{Fr} = \frac{\left(\rho_f - \rho_g\right) g_e D_h}{\rho_f U^2} \leq 0.13. \tag{6.14}$$

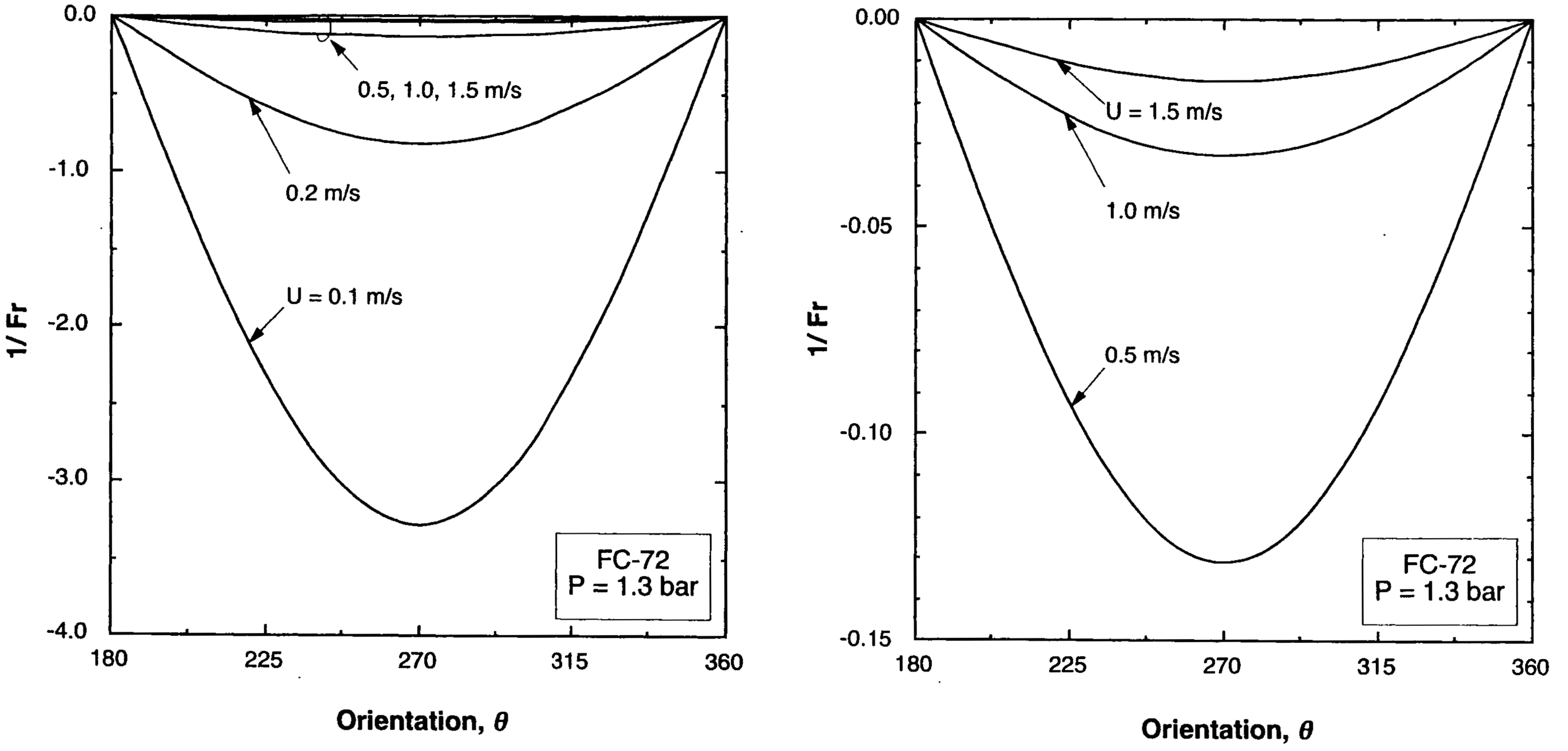

(a)

(b)

Fig. 6.3 Variation of 1/Fr with flow orientation and velocity for (a) all velocities tested and (b) U ≥ 0.5 m/s.

6.4 Critical Wavelength versus Heated Length

As discussed before, low flow velocities can produce very large values of critical wavelength. Replacing the phase velocity difference by the characteristic velocity of the flow channel, Eq. (6.7) reveals the largest value of critical wavelength is given by

$$\lambda_c = \frac{2\pi\sigma(\rho_f + \rho_g)}{\rho_f \rho_g U^2} \ . \tag{6.15}$$

Thus, to maintain a critical wavelength shorter than the heated length, L, the following Weber number criterion must be satisfied:

$$We = \frac{\rho_f \rho_g U^2 L}{(\rho_f + \rho_g)\,\sigma} \geq 2\pi \, . \tag{6.16}$$

6.5 Minimum Flow Velocity Required to Overcome Body Force Effects

It is now possible to combine the above three criteria in pursuit of a comprehensive methodology to overcome body force effects. Equations (6.11), (6.14) and (6.16) reveal that increasing flow velocity is perhaps the most effective means for satisfying these criteria. Velocity is an important parameter for the design of thermal management systems in both terrestrial and space applications. For the latter, coolant velocity has a strong bearing on pumping power and therefore overall power consumption. Using low velocities is therefore vital to reducing power consumption provided the aforementioned flow anomalies can be prevented.

Figure 6.4 shows the minimum velocity required to satisfy the above criteria as a function of a/g_e, the ratio of body force per unit mass to Earth's gravity. This was accomplished by substituting g_e in Eqs. (6.11) and (6.14) by a. Avoiding body force effects requires that flow velocity exceed values predicted by each of the three criteria.

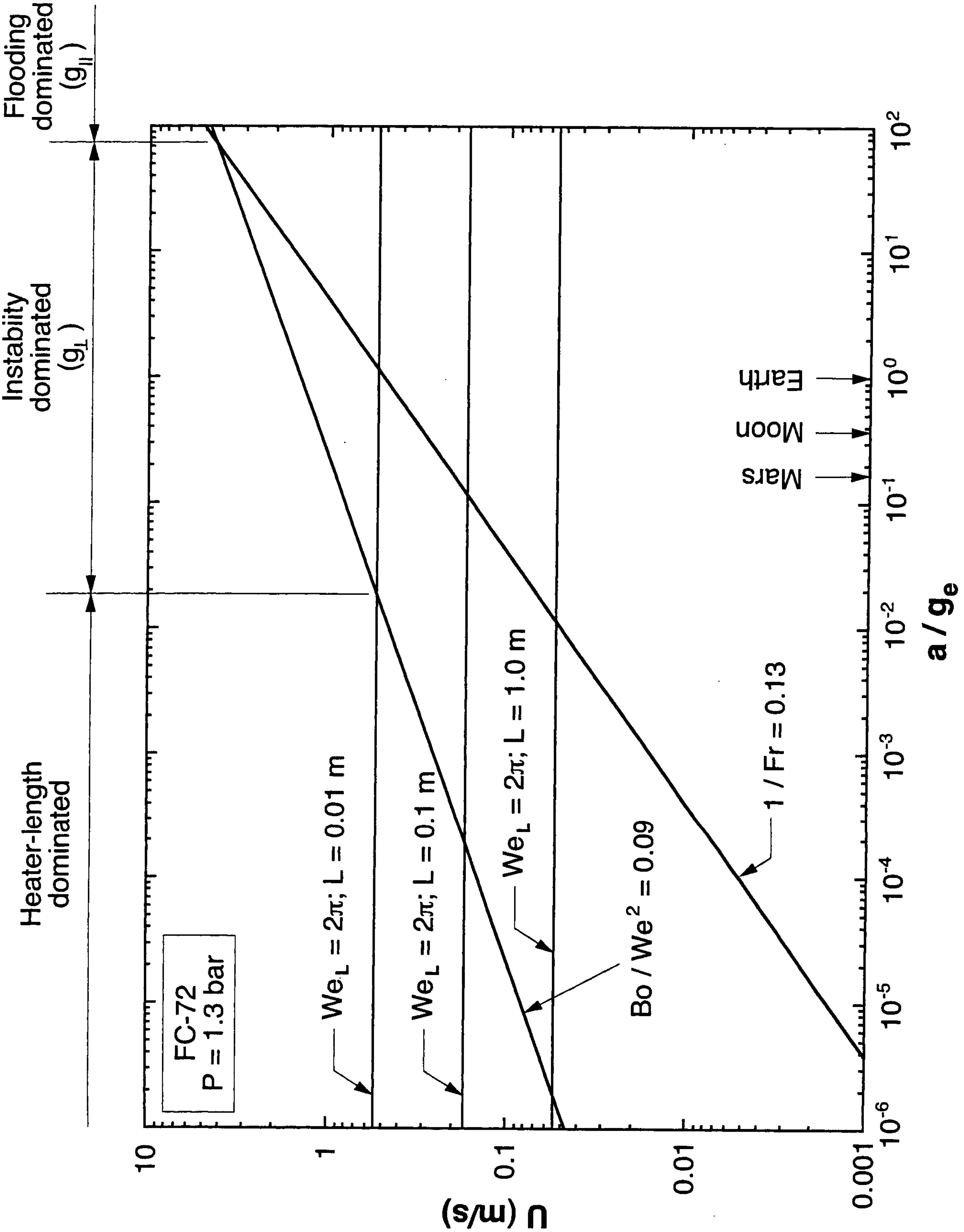

Fig. 6.4 Determination of minimum flow velocity required to overcome all body force effects on flow boiling CHF.

Only one of these criteria is dominant for a given value of a/g_e. Figure 6.4 shows fairly appreciable flow velocities will be required to overcome flooding effects, should a large body force of $a/g_e > 75$ be present in a direction opposite to the liquid flow. Instability effects are dominant when a body force of $a/g_e < 75$ is present in a direction perpendicular to the heated wall, as surface tension effects become increasingly important. These instability effects span Earth, Lunar and Martian environments. The heater length criterion is dominant for relatively low values of a/g_e. However, the transition a/g_e value between the instability-dominated and heater-length-dominated regimes is a function of the heated length; shorter heaters require higher velocities to decrease critical wavelength below the heated length. Overall, the heater-length-dominated regime appears quite significant for microgravity conditions.

Obviously, the validation of this methodology for determining the minimum velocity required to overcome body force effects on flow boiling CHF will require future tests with other coolants, especially in a reduced gravity environment. Such tests represent future goals for a follow-up study.

CHAPTER 7

PREPARATION FOR FLIGHT EXPERIMENT

7.1 Fast-Response Heater

For the future parabolic flight experiments, a new heater with fast time response was designed and fabricated. The heater consists of a 0.80 mm thick oxygen-free copper plate to which a series of six thick-film resistors are soldered. As shown in Fig. 7.1, each resistive heater measures 16.1 mm x 4 mm and has a resistance of about 188 Ω. These resistors are soldered as a linear array along the underside of the copper plate as depicted in Figs. 7.2 and 7.3.

Five thermocouples are inserted into the copper plate between the resistive heaters, aligned along the centerline of the plate. The six restive heaters are connected in a parallel electrical circuit which provides equal voltage drop across each resistor. To preclude variations in power dissipation between the individual resistive heaters, the six heaters were carefully selected from a large batch of resistors based on equal resistance values. This ensures equal current supply through each resistor and, hence, uniform heat flux along the copper surface. Power dissipation from these heaters will be determined from the current and voltage measurements. Figure 7.4 shows the fully assembled heater.

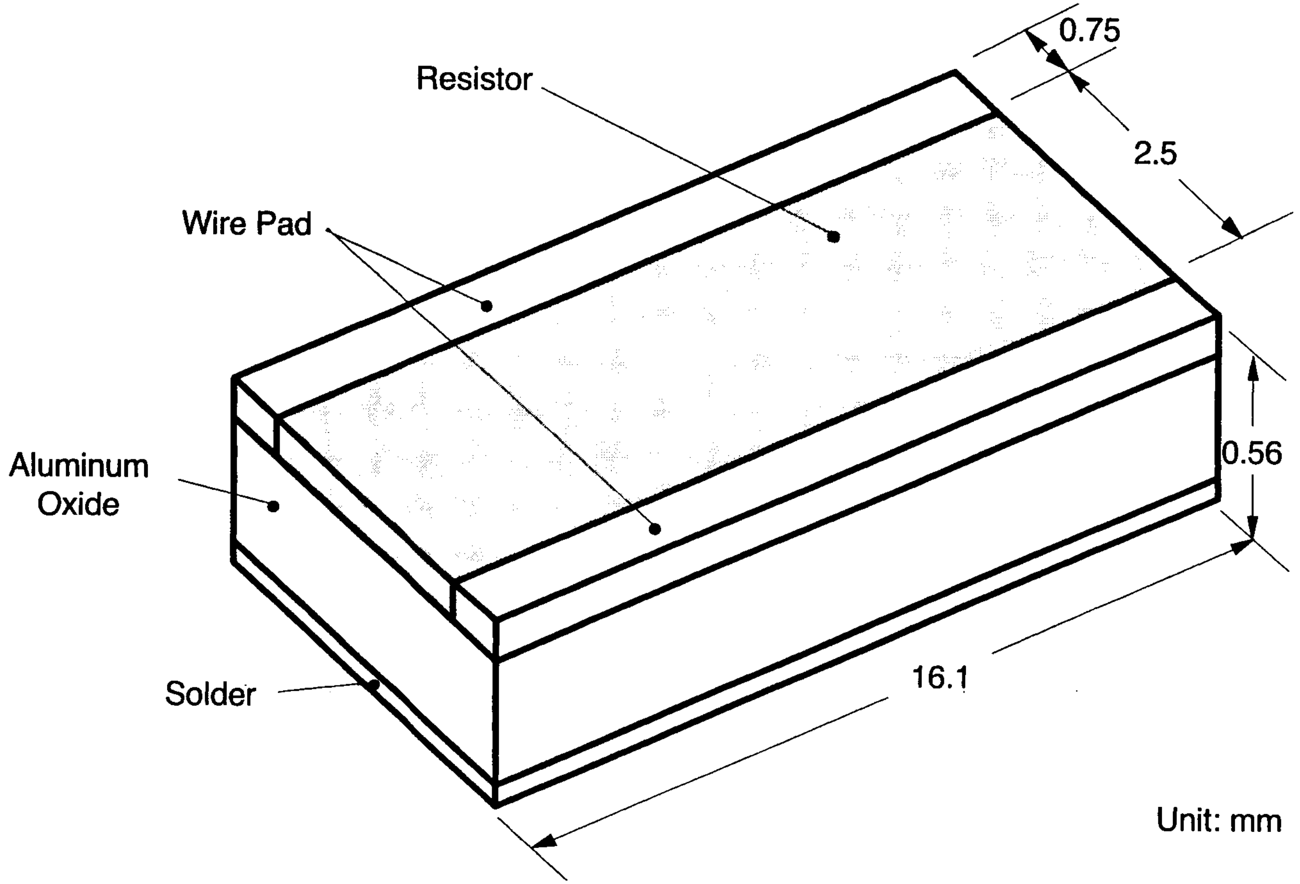

Fig. 7.1 Thick-film resistor.

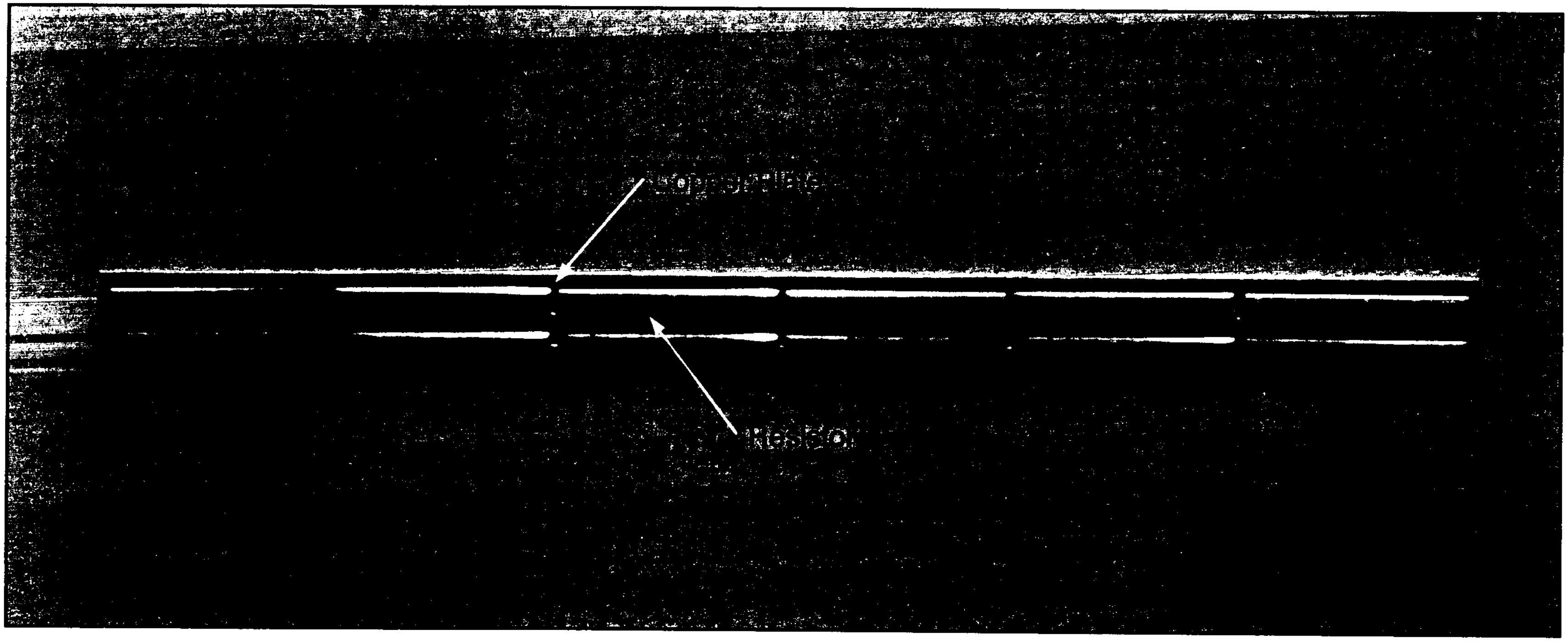

Fig. 7.2 Copper plate with resistors.

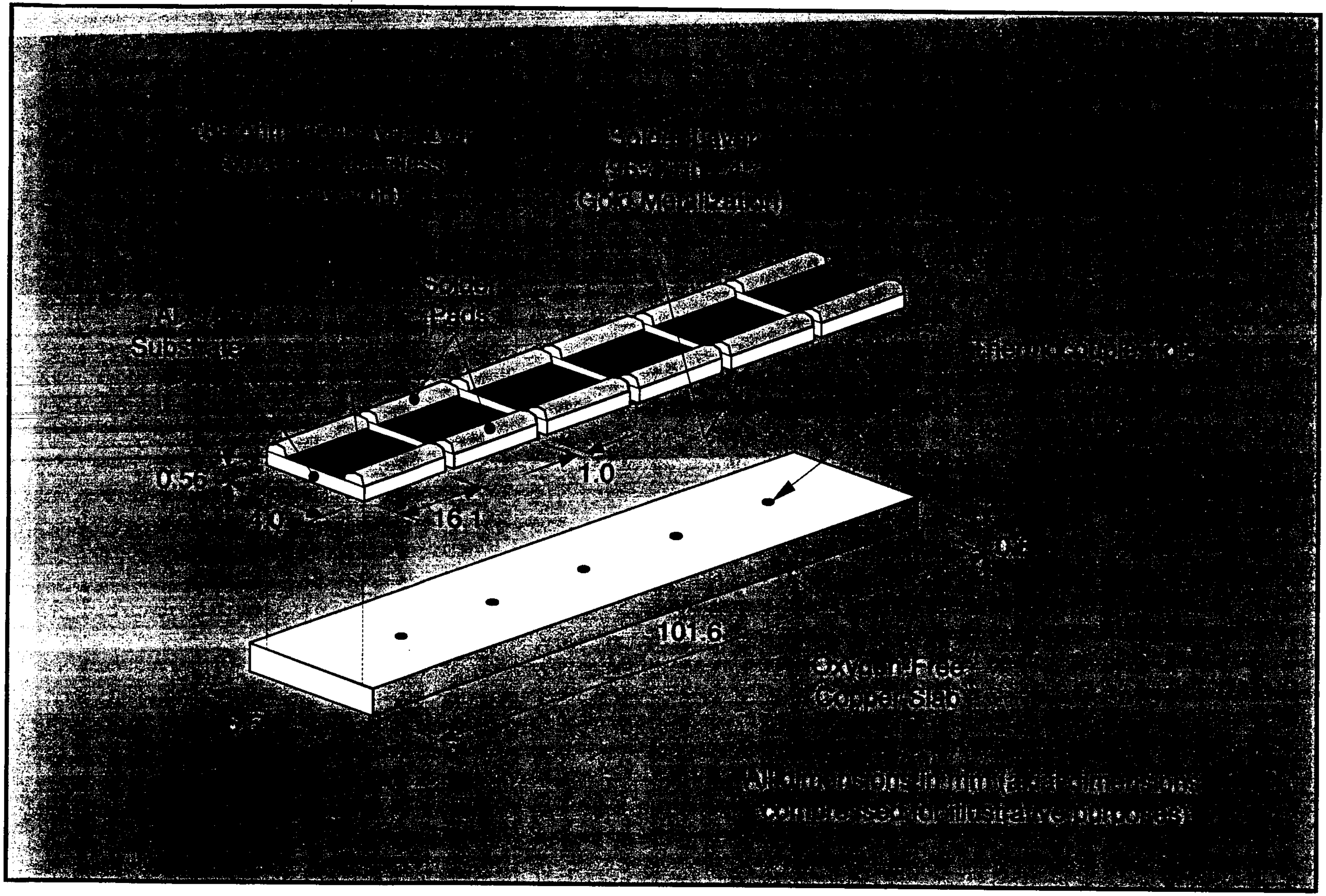

Fig. 7.3 Construction of fast-response heater.

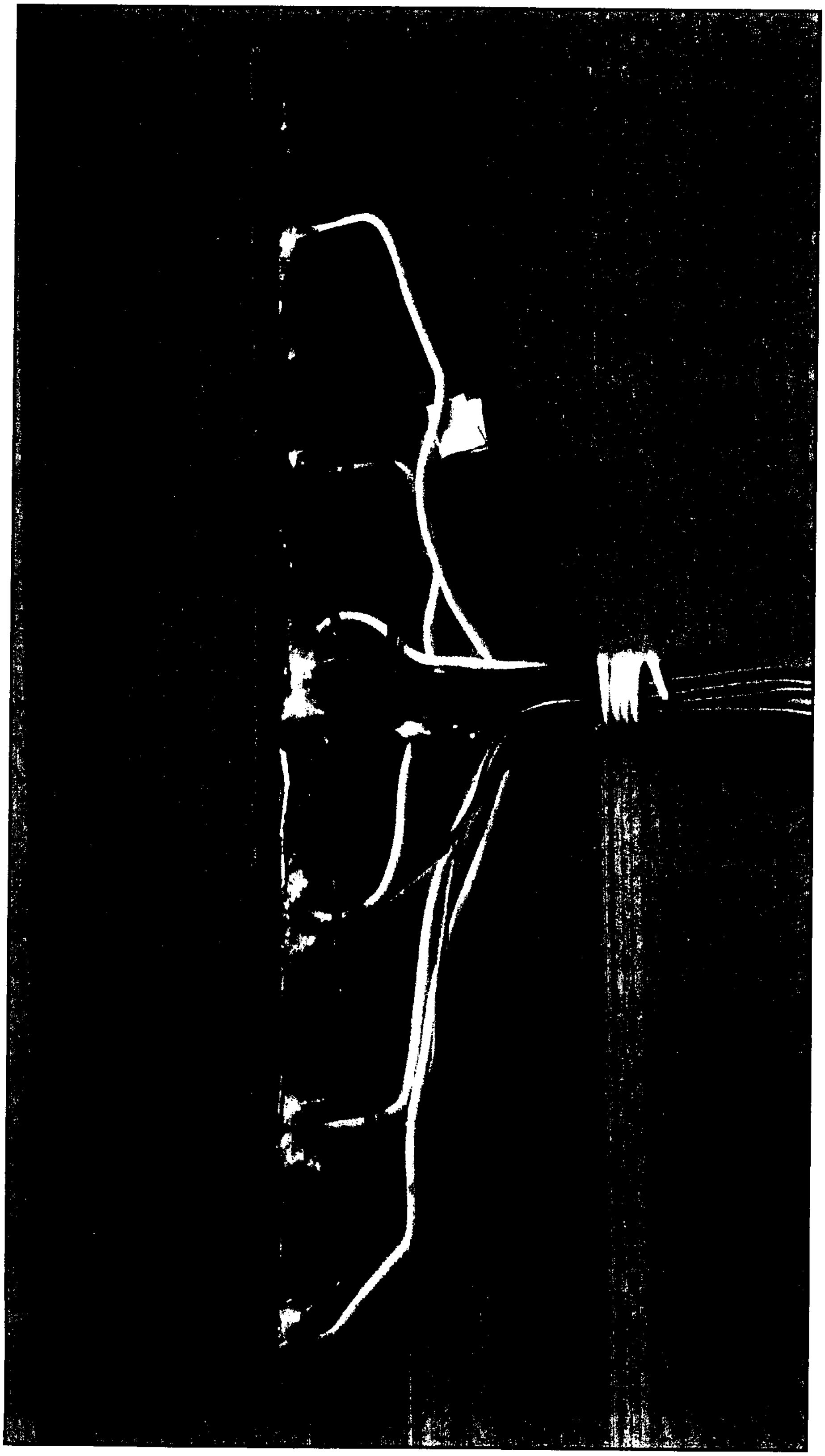

Fig. 7.4 Assembled heater.

7.2 Flow Boiling Module

As shown in Figs. 7.5 and 7.6, the flow boiling module is formed by bolting together two transparent polycarbonate plastic (Lexan) plates between two aluminum support plates. The flow channel is constructed by milling a 5.0 × 2.5 mm rectangular slot into the top Lexan plate. A rectangular groove is milled into the bottom plate to introduce the copper plate and flush mount it with the upper surface of the bottom Lexan plate. The cross section of the channel is illustrated in Fig. 7.7. A leak-proof seal is maintained by a flexible Teflon cord placed in a shallow O-ring slot on the upper surface of the bottom Lexan plate when the two plates are bolted together. A honeycomb insert is placed at the channel inlet to straighten the flow and break up any large eddies. An entry length 106 times the channel hydraulic diameter provides a hydrodynamically fully-developed flow upstream of the heater. Just upstream and downstream of the heater, thermocouples and pressure transducers are connected via compression fittings to the top plate to measure fluid conditions at these two locations. Figure 7.8 shows a photo of the assembled flow boiling module.

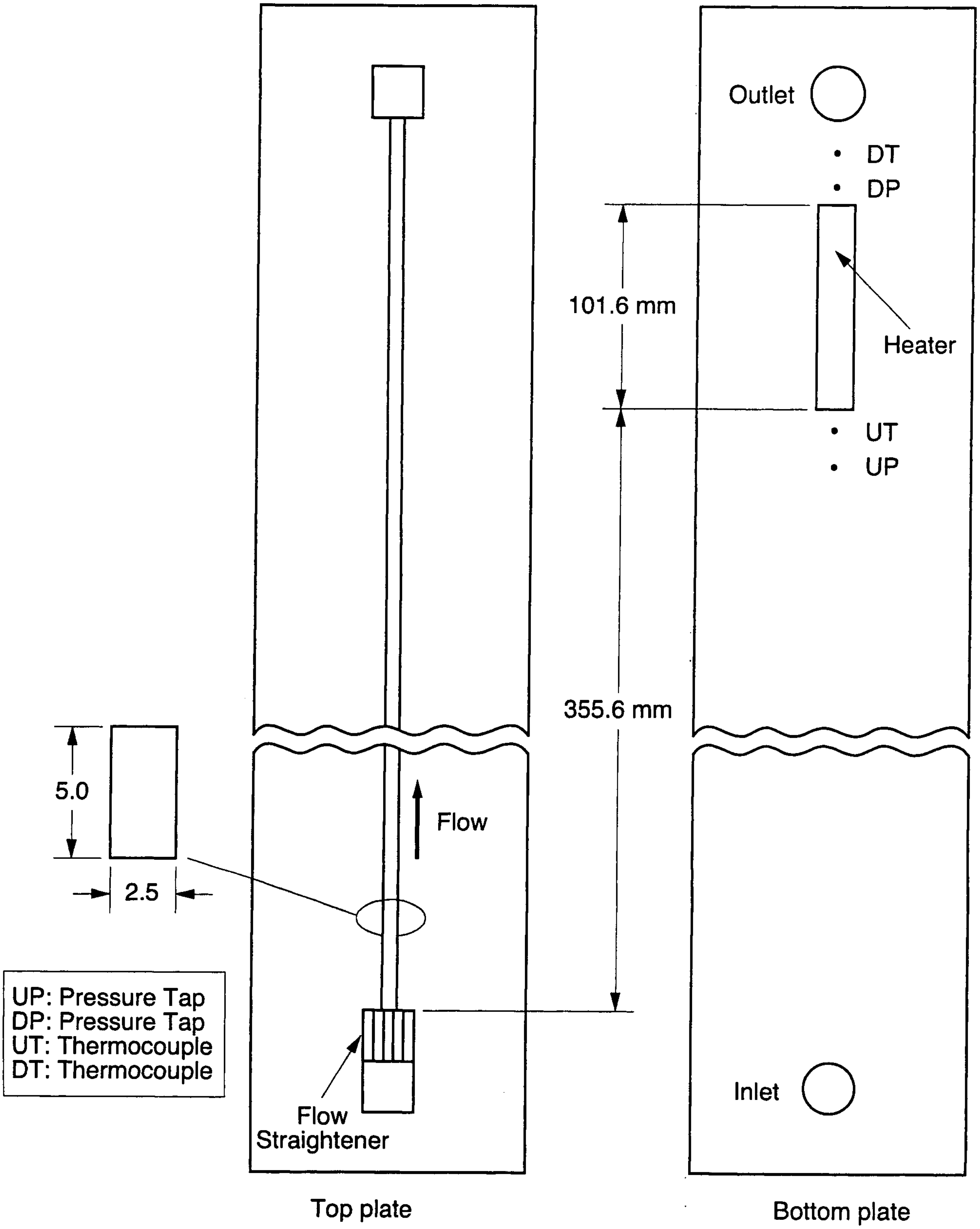

Fig. 7.5 Top and bottom plates of test channel.

Fig. 7.6 Main parts of test channel.

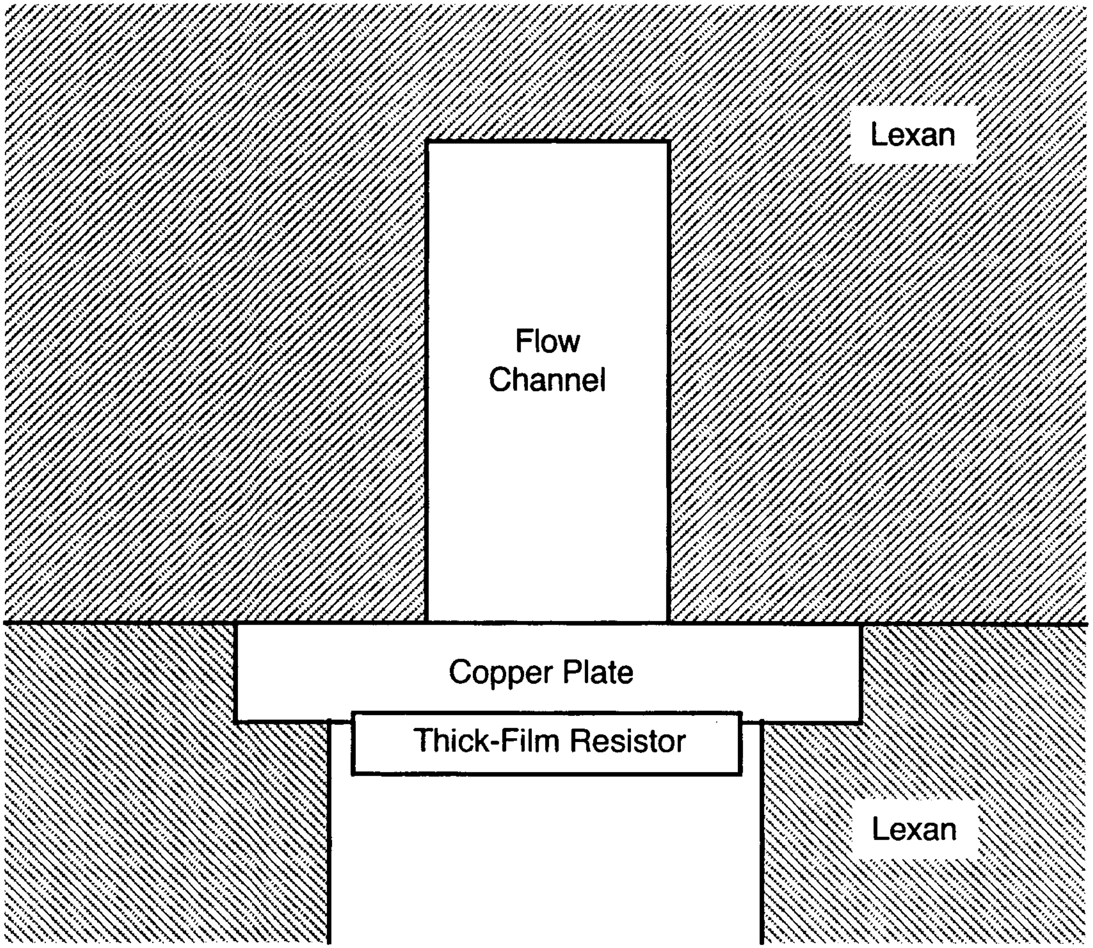

Fig. 7.7 Cross-section of test channel.

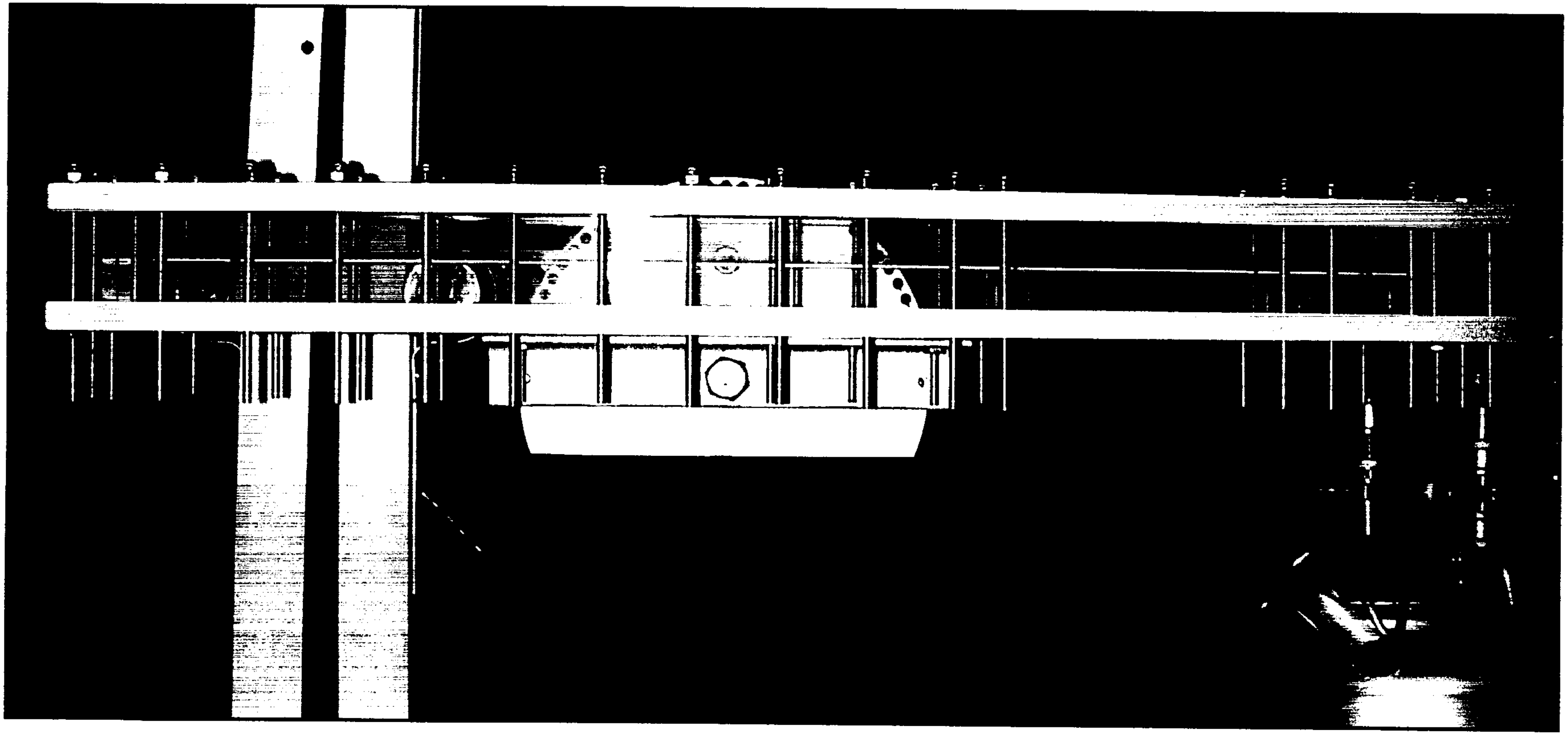

Fig. 7.8 Assembled test channel.

CHAPTER 8

CONCLUSIONS

This study involved both experimental and theoretical investigation of the effects of orientation on flow boiling CHF. High-speed video and microphotographic techniques were used to measure interfacial features just prior to CHF. Key findings from the study are as follows:

(1) Six different CHF regimes were observed. A dominant wavy vapor layer regime was observed for all relatively high velocities and most orientations, while all the other regimes were encountered at low velocities, in downflow and/or downward-facing heated wall orientations. The present CHF model is intended only for the dominant wavy vapor layer regime.

(2) Video analysis of the wavy vapor layer supports Galloway and Mudawar's [20,21] depiction of a fairly continuous wavy vapor layer travelling along the wall while permitting liquid contact only in wetting fronts, located in the troughs of the interfacial waves.

(3) An instability model of the wavy vapor layer interface shows low phase velocity differences produce a stable interface for certain orientations, precluding liquid contact with the heated wall and resulting in very low CHF values. Even with an

unstable wave that provides the necessary liquid contact, low phase velocity differences produce unusually large wavelengths capable of engulfing a large fraction of the heated length. Increasing phase velocity difference reduces the sensitivity of critical wavelength to body force by imparting dominance to liquid inertia over body force.

(4) Interfacial measurements reveal both the wavelength and wetting front length increase in the flow direction but their ratio remains constant.

(5) Lift-off of wetting fronts is closely related to a wave curvature parameter $\delta^{1/2}/\lambda$. Measurements reveal waves in the outlet section of the heated wall are slightly flatter that those in the middle section, and therefore are easier to lift off. This was confirmed by consistent CHF detection in the outlet section. Overall, however, the waves, which are generated at an upstream location, have a tendency to preserve their curvature value as they propagate along the heated wall.

(6) The Interfacial Lift-off model is very effective at capturing the overall dependence of CHF on orientation. The mean absolute error of the model predictions from the data is 20.0, 9.8 and 5.4% for $U = 0.5$, 1.0 and 1.5 m/s, respectively. For the lower velocities, the model is not valid for certain downflow orientations which are associated with a stable interface.

(7) Three dimensionless criteria were developed to determine the minimum flow velocity required to overcome body force effects on flow boiling CHF. Only one of the three criteria is dominant for a given gravitational field. This methodology may

help reduce electric power consumption in space thermal management systems, provided it is ultimately validated for other coolants, especially in microgravity.

(8) The combination of video imaging of flow boiling in a thin rectangular channel and image analysis software is an effective means to estimating void fraction as well as tracking the wavy vapor layer development during the CHF transient.

(9) Video images and void fraction records of both saturated and subcooled flow show the development of a wavy vapor layer which propagates along the heated wall permitting cooling prior to CHF in wetting fronts corresponding to the wave troughs.

(10) The void fraction records for subcooled flow boiling show the CHF transient is accompanied by gradual lift-off of wetting fronts culminating in some maximum vapor layer mean thickness, following which the vapor layer begins to thin down as the transition to film boiling ensues.

(11) This study proves the Interfacial Lift-off Model is equally valid for subcooled flow boiling CHF as it is for saturated. Future work should therefore focus on understanding the partitioning of wall energy between sensible and latent components to derive accurate energy balance framework in which to incorporate the Interfacial Lift-off Model.

REFERENCES

1. J.G. Collier and J.R. Thome, Convective Boiling and Condensation, 3rd ed., Clarendon Press, Oxford, United Kingdom, 1994, pp. 325-424.
2. S.S. Kutateladze and A.I. Leont'ev, Some applications of the asymptotic theory of the turbulent boundary layer, Proceedings of the Third International Heat Transfer Conference, vol. 3, AIChE, New York, 1966, pp. 1-6.
3. L.S. Tong, Boundary-layer analysis of the flow boiling crisis, Int. J. Heat Mass Transfer 11 (1968) 1208-1211.
4. L.S. Tong, A phenomenological study of critical heat flux, ASME Paper 75-HT-68 (1975).
5. J.C. Purcupile and S.W. Gouse, Jr., Reynolds flux model of critical heat flux in subcooled forced convection boiling, ASME Paper 72-HT-4 (1972).
6. J. Weisman and B.S. Pei, Prediction of critical heat flux in flow boiling at low qualities, Int. J. Heat Mass Transfer 26 (1983) 1463-1477.
7. J. Weisman and S. Ileslamlou, A phenomenological model for prediction of critical heat flux under highly subcooled conditions, Fusion Technology 13 (1988) 654-659.
8. M.A. Styrikovich, E.I. Nevstrueva and G.M. Dvorina, The effect of two-phase flow pattern on the nature of heat transfer crisis in boiling, in Heat Transfer 1970: Fourth International Heat Transfer Conference, vol. 6, U. Grigull and E. Hahne, eds., Elsevier Publishing Co., Amsterdam, Netherlands, Paper B 6.10, 1970.
9. M.P. Fiori and A.E. Bergles, Model of critical heat flux in subcooled flow boiling, in Heat Transfer 1970: Fourth International Heat Transfer Conference, vol. 6, U. Grigull and E. Hahne, eds., Elsevier Publishing Co., Amsterdam, Netherlands, Paper B 6.3, 1970.
10. R. Mesler, A mechanism supported by extensive experimental evidence to explain high heat fluxes observed during nucleate boiling, AIChE J. 22 (1976) 246-252.

11. S.B. van der Molen and F.W.B.M. Galjee, The boiling mechanism during burnout phenomena in subcooled two-phase water flows, in Heat Transfer 1978: Sixth International Heat Transfer Conference, vol. 1, Hemisphere Pub. Corp., Washington, DC, 1978, pp. 381-385.
12. G.P. Celata, M. Cumo, A. Mariani and G. Zummo, Preliminary remarks on visualization of high heat flux burnout in subcooled water flow boiling, in Two-Phase Flow Modelling and Experimentation 1995, vol. 2, G.P. Celata and R.K. Shah, eds., Edizioni ETS, Pisa, Italy, 1995, pp. 859-866.
13. C.H. Lee and I. Mudawar, A mechanistic critical heat flux model for subcooled flow boiling based on local bulk flow conditions, Int. J. Multiphase Flow 14 (1989) 711-728.
14. W.-S. Lin, C.-H. Lee, and B.-S. Pei, An improved theoretical critical heat flux model for low-quality flow, Nuclear Technology 88 (1989) 294-306.
15. Y. Katto, A physical approach to critical heat flux of subcooled flow boiling in round tubes, Int. J. Heat Mass Transfer 33 (1990) 611-620.
16. Y. Katto, Prediction of critical heat flux of subcooled flow boiling in round tubes, Int. J. Heat Mass Transfer 33 (1990) 1921-1928.
17. Y. Katto, A prediction model of subcooled water flow boiling CHF for pressure in the range 0.1-20 MPa, Int. J. Heat Mass Transfer 35 (1992) 1115-1123.
18. G.P. Celata, M. Cumo, A. Mariani, M. Simoncini and G. Zummo, Rationalization of existing mechanistic models for the prediction of water subcooled flow boiling critical heat flux, Int. J. Heat Mass Transfer 37 (1994) 347-360.
19. G.P. Celata, M. Cumo, Y. Katto and A. Mariani, Prediction of the critical heat flux in water subcooled flow boiling using a new mechanistic approach, Int. J. Heat Mass Transfer 42 (1999) 1457-1466.
20. J.E. Galloway and I. Mudawar, CHF mechanism in flow boiling from a short heated wall - I. Examination of near-wall conditions with the aid of photomicrography and high-speed video imaging, Int. J. Heat Mass Transfer 36 (1993) 2511-2526.
21. J.E. Galloway and I. Mudawar, CHF mechanism in flow boiling from a short heated wall - II. Theoretical CHF model, Int. J. Heat Mass Transfer 36 (1993) 2527-2540.
22. C.O. Gersey and I. Mudawar, Effects of heater length and orientation on the trigger mechanism for near-saturated flow boiling critical heat flux - I. Photographic study and statistical characterization of the near-wall interfacial features, Int. J. Heat Mass Transfer 38 (1995) 629-641.

23. C.O. Gersey and I. Mudawar, Effects of heater length and orientation on the trigger mechanism for near-saturated flow boiling critical heat flux - II. Critical heat flux model, Int. J. Heat Mass Transfer 38 (1995) 643-654.
24. J.C. Sturgis and I. Mudawar, Critical heat flux in a long, rectangular channel subjected to one-sided heating - I. Flow visualization, Int. J. Heat Mass Transfer 42 (1999) 1835-1847.
25. J.C. Sturgis and I. Mudawar, Critical heat flux in a long, rectangular channel subjected to one-sided heating - II. Analysis of critical heat flux data, Int. J. Heat Mass Transfer 42 (1999) 1849-1862.
26. H. Zhang, I. Mudawar and M.M. Hasan, Experimental assessment of the effects of body force, surface tension force, and inertia on flow boiling CHF, Int. J. Heat Mass Transfer 45 (2002) 4079-4095.
27. H. Zhang, I. Mudawar and M.M. Hasan, Experimental and theoretical study of orientation effects on flow boiling CHF, Int. J. Heat Mass Transfer 45 (2002) 4463-4477.
28. A.H. Howard and I. Mudawar, Orientation effects on pool boiling critical heat flux (CHF) and modeling of CHF for near-vertical surfaces, International Journal of Heat and Mass Transfer 42 (1999) 1665-1688.
29. N. Zuber, M. Tribus, and J.W. Westwater, The hydrodynamic crisis in pool boiling of saturated and subcooled liquids, International Developments in Heat Transfer: Proceedings of 1961-62 International Heat Transfer Conference, Boulder, CO, 1961, pp. 230-236.
30. R.J. Simoneau and F.F. Simon, A visual study of velocity and buoyancy effects on boiling Nitrogen, NASA Tech Note TN D-3354, 1966.
31. K. Mishima and H. Nishihara, The effect of flow direction and magnitude on CHF for low pressure water in thin rectangular channels, Nuclear Engineering and Design 86 (1985) 165-181.
32. L.M. Milne-Thomson, Theoretical Hydrodynamics, 4th ed., MacMillan, New York, 1960.
33. Z. Nejat, Effect of Density Ratio on Critical Heat Flux in Closed End Vertical Tubes, Int. J. Multiphase Flow 7 (1981) 321-327.
34. G.B. Wallis, One-Dimensional Two-Phase Flow, New York, McGraw-Hill Book Company, 1969.